

The
**PHILOSOPHICAL
MAGAZINE**

FIRST PUBLISHED IN 1798

. 46 SEVENTH SERIES No. 374

UNIVERSITY OF HAWAII
LIBRARY
APR 29 '55
March 1955

*A Journal of
Theoretical Experimental
and Applied Physics*

EDITOR

PROFESSOR N. F. MOTT, M.A., D.Sc., F.R.S.

EDITORIAL BOARD

SIR LAWRENCE BRAGG, O.B.E., M.C., M.A., D.Sc., F.R.S.

SIR GEORGE THOMSON, M.A., D.Sc., F.R.S.

PROFESSOR A. M. TYNDALL, C.B.E., D.Sc., F.R.S.

PRICE 15s. 0d.

Annual Subscription £8 0s. 0d. payable in advance

AND PUBLISHED BY TAYLOR & FRANCIS LTD., RED LION COURT, FLEET ST., LONDON, E.C.4.

New Interscience Books

LECTURES ON PARTIAL DIFFERENTIAL EQUATIONS

By I. G. PETROVSKY

Translated from the Russian by A. SHENITZER

CONTENTS: Introduction. Classification of Equations. Hyperbolic Equations: The Cauchy Problem for Non-analytic Functions. Vibrations of Bounded Bodies. Elliptic Equations. Parabolic Equations.

1954

255 pages, 17 illus.

41/-

HIGH-ENERGY ACCELERATORS

By M. STANLEY LIVINGSTON (*Massachusetts Institute of Technology*)
(Interscience Tracts on Physics and Astronomy, Volume II)

CONTENTS: High-Energy Accelerators as Tools for Nuclear Research. Principles of Acceleration to High Energies. The Electron Synchrotron. The Synchrocyclotron. Linear Accelerators. The Proton Synchrotron. Alternating Gradient Focusing. References. Index.

1954

5 × 8

165 pages, with many diagrams

26/-

THE METHOD OF TRIGONOMETRIC SUMS IN THE THEORY OF NUMBERS

By I. M. VINOGRADOV

*Translated from the Russian, revised and annotated by K. F. ROTH, B.A., Ph.D.,
and ANNE DAVENPORT, M.A. (University College, London)*

"Since 1934 the analytic theory of numbers has been largely transformed by the work of Vinogradov. This work, which has led to remarkable new results, is characterized by its supreme ingenuity and great power. . . ."

from the preface.

CONTENTS: Preface. Notation. Introduction. Note on Vinogradov's Method by the Translators. I. General Lemmas. II. The Investigation on the Singular Series in Waring's Problem. III. The Contribution of the Basic Intervals in Waring's Problem. IV. An Estimate for $G(n)$ in Waring's Problem. V. Approximation by the Fractional Parts of the Values of a Polynomial. VI. Estimates for Weyl Sums. VII. The Asymptotic Formula in Waring's Problem. VIII. The Distribution of the Fractional Parts of the Values of a Polynomial. IX. Estimates for the Simplest Trigonometrical Sums with Primes. X. Goldbach's Problem. XI. The Distribution of the Fractional Parts of the Values of the Function.
Each Chapter with Notes by the Translators.

1954

6 × 9

190 pages

33/-

INTERSCIENCE PUBLISHERS LTD
88-90 CHANCERY LANE, LONDON, W.C.2

XXIX. *The Growth of Ice Crystals from the Vapour*

By D. SHAW and B. J. MASON
Imperial College, London *

[Received November 18, 1954]

SUMMARY

The growth and evaporation of single ice crystals have been studied in relation to the temperature and supersaturation of the environment. The sequence of crystal forms which occurs in clouds as the temperature falls from 0°C to -40°C has been reproduced in these experiments. Measurements of the growth rates of individual faces of crystals growing under fixed environmental conditions reveal that $dR^2/dt = \text{const.}$ where R is a linear crystal dimension, but the growth rates of basal and prism faces are different to a degree depending mainly on the temperature. At constant temperature, dR^2/dt varied as the square of the supersaturation σ over the range of σ studied. A critical supersaturation for growth was found which varied in an apparently random manner from face to face, there being no systematic difference between the values for the prism and basal faces. The crystal habit, defined by limiting values of the axis/diameter ratio, was found to be controlled very largely by the temperature, the supersaturation having a much smaller, non-systematic effect.

§ 1. INTRODUCTION

THE growth of ice crystals, besides being an interesting and difficult study in crystal physics, is of particular importance to the cloud physicist concerned with the development of the ice phase in natural clouds. Snow crystals occur in a wide variety of shapes and forms and many workers have tried to relate the occurrence of particular crystal forms with the meteorological conditions. That they have not found a clearly marked correlation between the predominant crystal habit and the temperature at the ground is, perhaps, not surprising, since only the conditions prevailing during the growth of the crystals are likely to be of major importance. It is only in recent years that crystals have been collected from different types of clouds having widely different conditions of temperature and water-vapour concentration, and that a correlation between the crystal habit and the environmental conditions has been established. The most comprehensive study of this kind has been made by Weickmann (1947) who took samples at different heights up to cirrus levels where the temperature was below -40°C. His observations are summarized in table 1.

* Communicated by the Authors.

The familiar needle-like crystals, which are not represented in Weickmann's observations, are observed at the ground when the temperature is only slightly below freezing, and according to Wall (1947) and to Gold and Power (1952), originate from clouds with temperatures between -3°C and -8°C .

Table 1. Weickmann's Observations of Predominant Crystal Forms in Different Cloud Types

Level of observation	Temp. range	Cloud types	Crystal forms
Lower troposphere	0°C to -15°C	Nimbostratus Stratocumulus	Thin hexagonal plates Star-shaped crystals showing dendritic structure
Middle troposphere	-15°C to -30°C	Stratus Altostratus Alto cumulus	
Upper troposphere	$< -30^{\circ}\text{C}$	Isolated cirrus Cirrostratus	Thick hexagonal plates Prismatic columns—single prisms and twins Clusters of prismatic columns containing funnel-shaped cavities. Some single hollow prisms Individual, complete prisms

The existence of a number of basic forms of snow crystals, e.g. hexagonal plates, hexagonal prismatic columns, dendritic forms, and of an almost infinite number of variations on each of these main themes, suggests that their growth and development are complicated matters. As some of these variations may arise from changes in environmental conditions as the crystal falls through the atmosphere, it seems judicious to study the growth of crystals in the laboratory where the temperature and supersaturation of the environment can be controlled.

The growth of crystals in artificially-produced supercooled water clouds has been studied by aufm Kampe, Weickmann and Kelly (1951) and by Mason (1953). The clouds are formed by introducing steam into thermostatically-controlled, room-size, cold chambers and crystal formation is initiated by seeding the cloud with a minute quantity of solid carbon-dioxide. In the presence of a water cloud it can be assumed that the crystals are growing in an atmosphere saturated with respect to liquid water, and therefore supersaturated with respect to ice by an amount determined solely by the temperature.

The observed changes of crystal habit with temperature were very similar in both sets of experiments and are summarized in table 2, which shows a marked similarity to table 1 giving the temperature classification of natural snow crystals.

Table 2. Changes of Crystal Habit with Temperature in Artificially-produced Water Clouds (aufm Kampe *et al.*, and Mason)

Temperature range	Crystal habit
0°C to -5°C	Single, clear, hexagonal plates with no surface markings. Some trigonal plates
-4°C to -9°C	Prisms, some showing marked cavities and similarity to needles
-10°C to -25°C	Hexagonal plates showing ribs, surface markings and tendency to sprout at corners. Sector stars
-25°C to -40°C	Dendritic stars, most prominent below -14°C Single prisms, twins, and hollow prisms. Aggregates of prisms and irregular crystals

The most striking feature of table 2 is the remarkable sequence of habit, plates-prisms-plates-prisms which occurs as the temperature is lowered from 0°C to about -25°C. Such marked changes in habit within this small temperature range, involving changes from preferred growth along the principal *c* axis for prisms, to preferred growth along the secondary *a* axes for plates, are apparently peculiar to ice.

To investigate in more detail the factors which control the relative growth rates of different crystal faces, it was decided to make continuous observations on single crystals growing in an atmosphere where the temperature and supersaturation could be controlled and varied independently. The crystals were grown on a metal surface, their growth being recorded by time-lapse photography so that the rates of advance of the different crystal faces could be measured.

§ 2. THE EXPERIMENTAL ARRANGEMENT

A diagram of the apparatus is shown in fig. 1. The clean, smooth, metal surface on which the crystals are grown is situated in the centre of a cylindrical metal chamber, internal diameter 3 inches and depth 2 inches, the hollow walls of which may be cooled down to a temperature of -55°C by circulating petrol chilled with solid CO₂ through the annular space. The temperature of the chamber walls is controlled by the temperature of a cold bath in which is immersed a long copper spiral forming part of the circuit for the cooling fluid. The base of the chamber is coated with ice, so that the air in the experimental space, which is stirred by a small electric fan, is uniformly saturated with respect to ice at a temperature T_1 , indicated by a sensitive thermocouple embedded in the surface of the ice layer on the floor of the chamber. The temperature over the floor does not vary by more than 0.2°C, and the thermocouple is located in the coldest spot near the inlet for the cooling fluid.

The experimental surface, a metal plate, is supported on a long copper rod which is insulated from the chamber and dips into a Dewar flask containing liquid air. The plate is thus cooled to a temperature T_2 lower than that of the surrounding air, and which can be controlled by

varying the current through a heating coil wound around the copper rod. The temperature T_2 of the growing crystals is recorded by a thermocouple soldered immediately below the experimental surface, and the saturation ratio of the air in the immediate vicinity of the crystals is altered by adjusting the temperature difference $T_1 - T_2$, and is measured by the ratio of the equilibrium vapour pressure of ice at the temperatures T_1 and T_2 respectively.

Fig. 1

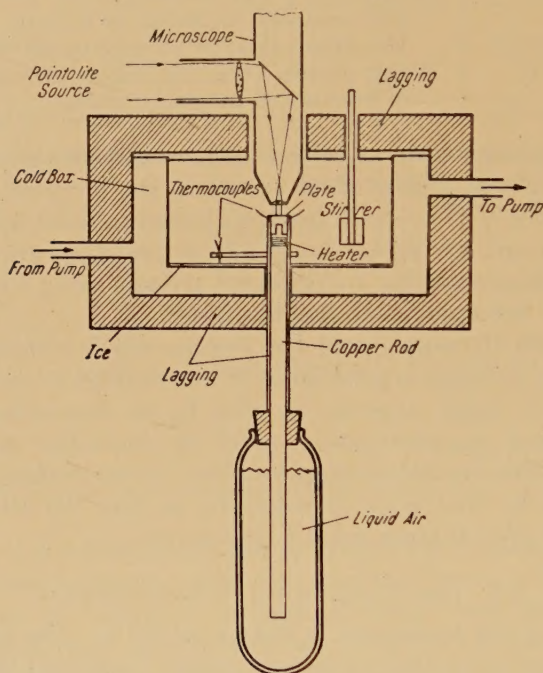


Diagram of the apparatus.

The crystals were viewed through a metallurgical microscope fitted with a vertical illuminator and a 4 mm objective, and were photographed at one-minute intervals with a 16 mm camera using a fine-grain film. The growth rates of the crystal faces were determined from measurements made on the negatives with a micrometer eyepiece.

§ 3. FORMATION OF CRYSTALS ON THE METAL SURFACE

In order to produce ice crystals on the test surface it was generally found necessary to cool it to the dew point of the surrounding air, so that *condensation* occurred on the plate. This confirmed the earlier observations of Weickmann (1947) that the great majority of crystals form only when the air is saturated with respect to liquid water, and therefore probably arise by the freezing of the supercooled liquid. Only an occasional crystal formed slightly before the dew point was reached ;

in these cases the air was highly supersaturated relative to ice and condensation of very small quantities of water may have occurred in surface cavities of solid nuclei or in fine scratches on the metal surface. To obtain a regular crop of well-formed crystals the metal plate was exposed to a small dose of silver-iodide smoke which provides active nuclei at temperatures below -5°C .

Typical examples of crystals forming at different temperatures are shown in fig. 2 (Plate 3). Crystals which grew with their c axes normal to the surface permitted measurement of the rates of advance of three pairs of opposite prism faces. In the case of hexagonal prisms growing with their c axes parallel to the surface, measurements could be made of the growth rates of both the basal faces and the prism faces. Since it was possible to measure only the diameters and length of a crystal, the sum of the growth rates of opposite faces, rather than the growth rate of each face separately, was determined.

It was necessary to work with a sparse deposit of crystals, their spacing being large compared with their linear dimensions, so that the growth of one crystal did not seriously interfere with that of its neighbours.

§ 4. CORRESPONDENCE BETWEEN CRYSTAL FORMS APPEARING ON METAL PLATE AND IN CLOUDS

The first experiments were designed to show whether the various crystal forms appearing in natural and laboratory-produced clouds as described in the Introduction, could be produced in the same temperature ranges on the metal plate.

The plate temperature was held at various temperatures between -5°C and -40°C and crystals were grown at constant temperature, the supersaturation being adjusted to correspond to water-saturation. The crystal habit was found to alternate between prismatic columns and thin hexagonal plates as the temperature was lowered according to the following scheme :

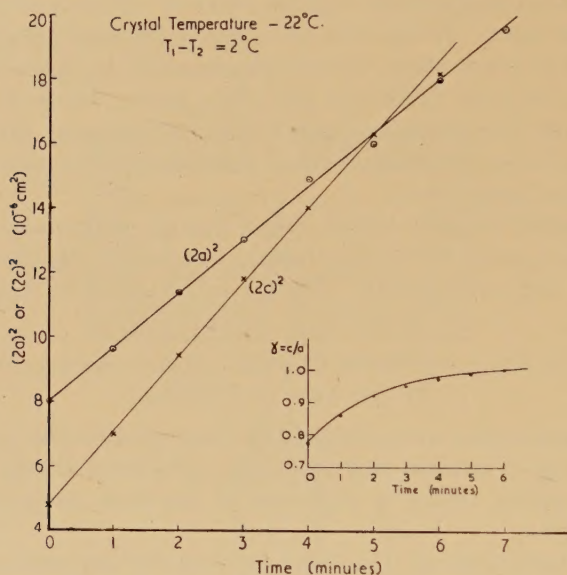
-5°C to -9°C Prisms,
 -9°C to -25°C Plates,
 below -25°C Prisms.

As a very few crystals appeared at temperatures above -5°C , crystals were initially formed at a lower temperature but grown subsequently at temperatures above -5°C . Although they may have originated at a temperature normally associated with prismatic columns, when the temperature was raised, they assumed subsequently the plate-like habit which was typical of the temperature range 0°C to -5°C in the cloud experiments.

Thus, the variation of crystal habit with temperature followed a very similar pattern to that found in both natural clouds and the model clouds of the laboratory. But, in addition, a new and interesting crystal form quite often appeared on the plate at temperatures between -4°C and

-8°C and also below -22°C . This took the form of a prismatic column terminated at *one end only* by a pyramid (see fig. 2). The appearance of such hemimorphic forms, which have been found only very occasionally in natural clouds (usually cirrostratus) but not at all in the small-scale laboratory clouds, is of considerable interest in connection with the possibility of ice possessing a polar lattice (see Owston (1951), Mason and Owston (1952)).

Fig. 3



Plot of the square of the linear dimensions of the crystal against time.

§ 5. GROWTH RATES OF CRYSTAL FACES

The photography at regular time intervals of crystals growing with their c axes either normal or parallel to the metal surface allowed the rates of advance of both the prism and basal faces to be determined. When the square of the linear dimensions ($(2c)^2$ or $(2a)^2$) of a crystal were plotted against time, straight lines resulted as shown in fig. 3.

The growth rate of a crystal under steady-state conditions is determined by the balance between the rate at which material diffuses towards the crystal and the rate at which it can be built into the crystal. If the diffusion rate is much greater than the rate of incorporation at the crystal face, the growth is said to be surface limited. If, however, the reverse is the case, the growth rate is determined almost entirely by the rate of diffusion, i.e. we have diffusion-limited growth. Under the latter circumstances, the rate of advance of a particular face should be inversely proportional to *some* linear dimension of the crystal. The fact that in our experiments the quantities da/dt and dc/dt were inversely proportional to a and c respectively and *not* to c and a respectively (the ratio $\gamma = c/a$

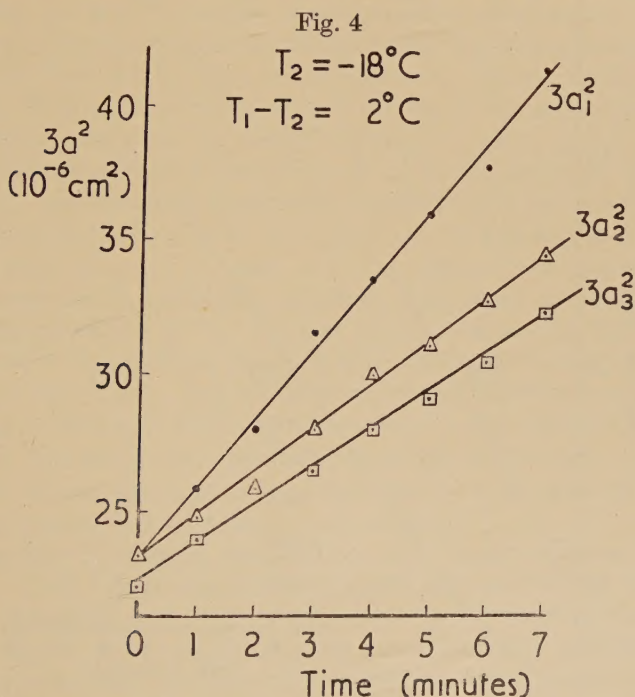
varied considerably during growth), enables us to describe the growth of the faces by the equations

$$(2c)^2 = U_c t + \alpha; \quad (2a)^2 = U_a t + \beta$$

where c and a are respectively the semi-principal and semi-secondary crystal axes, U_c , U_a , α and β are constants. It follows that the crystal grows towards a limiting habit which may be defined by

$$\Gamma = |c/a|_{\text{lim}} = \sqrt{(U_c/U_a)} = \sqrt{\left[\frac{\partial}{\partial t} (2c)^2 \right] / \left[\frac{\partial}{\partial t} (2a)^2 \right]}.$$

The limiting habit, which can be determined experimentally from the plots of $(2c)^2$ and $(2a)^2$ against time, is the most suitable parameter to use in discussing the crystal habit because, unlike the actual c/a ratio of the crystal, it is independent of the period of growth.

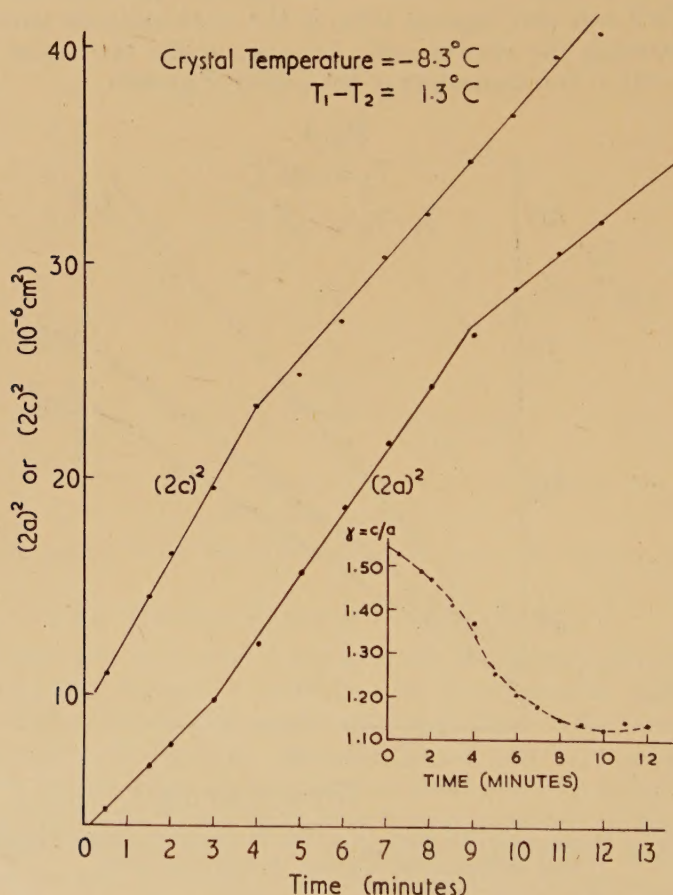


The growth of three opposite pairs of prism faces of the same crystal, showing that different faces grow at different rates.

Although the square law of growth held for all crystal faces indicating that the growth was largely controlled by diffusion, the actual values of da^2/dt and dc^2/dt were somewhat different for different crystals growing under the same environmental conditions, while crystallographically similar faces of the same crystal sometimes grew at different rates (differences of 50% were not uncommon) as shown in fig. 4. Furthermore, the growth rate of a particular crystal face sometimes changed abruptly, even though the temperature, supersaturation and rate of stirring remained

constant. A typical case is illustrated in fig. 5. Very similar behaviour has been observed by Bunn (1949) and by Humphreys-Owen (1949) in the case of crystals growing from solution. These results indicate that the growth of crystal faces is not determined solely by external conditions, but is partly influenced by certain properties of the faces themselves. Thus the variations in habit may be partly attributed to different faces having their own individual characteristics which control the rate at which the available molecules can be built into the crystal structure.

Fig. 5



Discontinuities in the growth rate of particular crystal faces.

Detailed examination of all the available data on crystals growing at constant temperature revealed no correlation between the limiting habit of a crystal and its rate of mass increase which is a measure of the contemporary total flux of vapour towards the crystal. This point is of importance in that Weickmann (1950) and also Marshall and Langleben (1954) have suggested that the crystal habit is essentially controlled by the flux of vapour towards the growing surfaces.

§ 6. VARIATION OF GROWTH AND EVAPORATION RATES WITH SATURATION RATIO

To study how the rate of propagation of a crystal face varied with the supersaturation of the environment, observations were made on individual crystals growing at constant temperature, as the supersaturation, governed by $(T_1 - T_2)$, was changed. The first step was to establish the absolute value of the supersaturation for each experiment. To do this, graphs of $\sqrt{U_c}$ and $\sqrt{U_a}$ were plotted against $(T_1 - T_2)$. The resulting straight lines cut the $(T_1 - T_2)$ axis at a distance $\pm \Delta T$ from the origin which was the same for the plots of $\sqrt{U_c}$ and $\sqrt{U_a}$. The intercept ΔT was always small in magnitude ($< 1^\circ\text{C}$), varied in sign from experiment to experiment and showed no systematic correlation with the plate temperature T_2 . These small fluctuations of the straight-line plots about the origin were probably due to slight changes of temperature distribution within the experimental chamber and also small changes in the air temperature within the cold box from experiment to experiment. These results indicated that ideally the supersaturation of σ of the air in the immediate vicinity of the crystals was given by $\sigma = p(T_1)/p(T_2) - 1$ where $p(T_1)$ and $p(T_2)$ are the equilibrium vapour pressures of ice at temperatures T_1 and T_2 respectively; the actual supersaturation prevailing in any one experiment was assumed to be $[p(T_1 \pm \Delta T) - p(T_2)]/p(T_2)$. In this way it was possible to obtain plots of $\sqrt{|U_c|}$ and $\sqrt{|U_a|}$ against the supersaturation σ , the temperature T_2 remaining constant, for a large number of crystals and for different values of T_2 . Typical plots are shown in figs. 6 (a), (b), which represent observations made during both growth and evaporation of basal and prism faces. In general, it was found that the quantity U was proportional to the square of the supersaturation σ (the values of σ employed ranged from 0 to 40%), but with the higher supersaturations there were occasions on which the growth rate was smaller than that which would be obtained by extrapolation of the $U - \sigma^2$ relation.

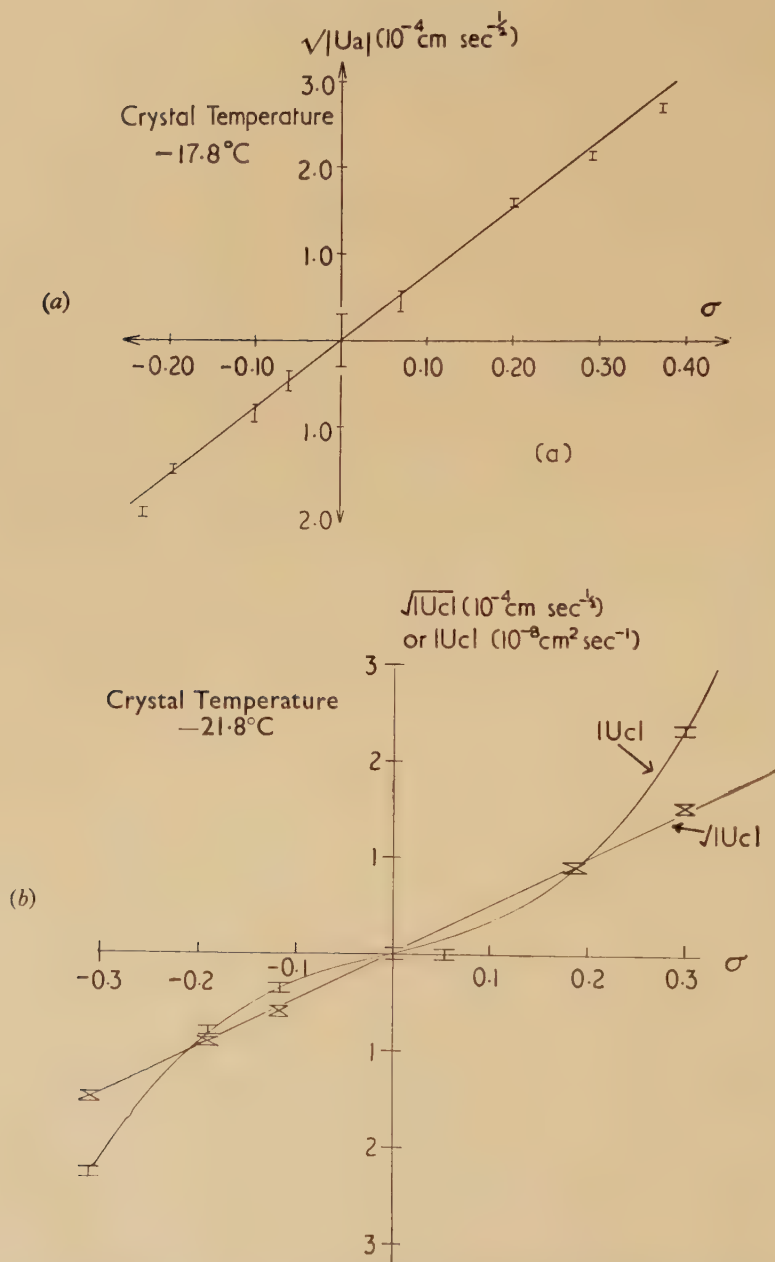
The behaviour of crystals evaporating under large subsaturations was interesting; under these conditions of rapid evaporation the reciprocity between evaporation and growth suggested by fig. 6 broke down. The crystal developed well rounded corners and eventually lost its external crystalline appearance, the rate of evaporation being much faster than the growth rate under a supersaturation of the same magnitude. It was suggested by Frank (1949) that at moderate subsaturations, dissolution of a crystal face should proceed in a manner closely equivalent to growth, i.e. by unbuilding at molecular steps ending on screw dislocations, but that under large subsaturations, evaporation may arise from attack at the edges and corners to produce curved faces; evaporation then proceeds rapidly and the crystal loses its geometrical shape.

§ 7. CRITICAL SATURATION RATIOS FOR GROWTH AND EVAPORATION

For some of the crystals studied, the saturation ratio $\alpha = \sigma + 1$ had to exceed or be less than a certain value before growth or evaporation of the

faces could be detected (see fig. 7). The value of the critical saturation ratio was often appreciably different for different faces of the same crystal, but there was no *systematic* difference between the initial resistance

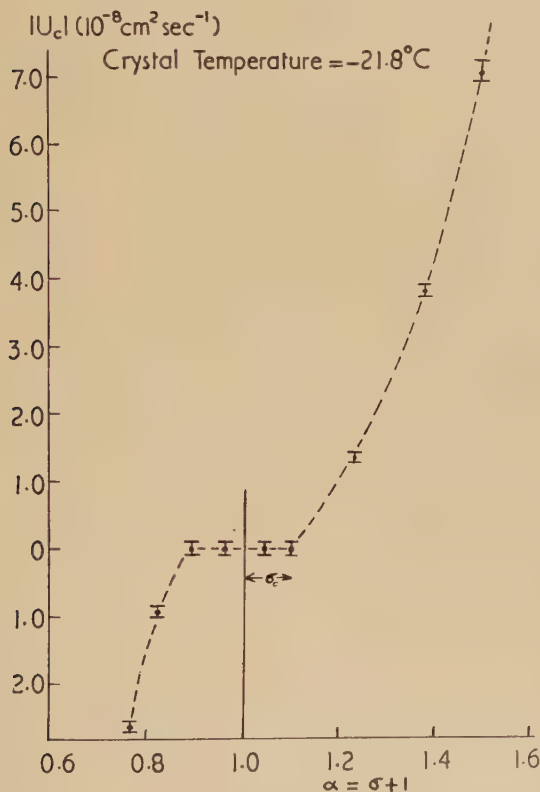
Fig. 6



Plots of $\sqrt{|U_a|}$, $\sqrt{|U_c|}$ and $|U_c|$ against the supersaturation σ .

of prisms and basal faces. This is obvious from fig. 8 in which are plotted the critical values of α for crystals growing at different temperatures. Again, there was evidence that growth and evaporation occurred more readily on some faces than on others which were crystallographically similar.

Fig. 7



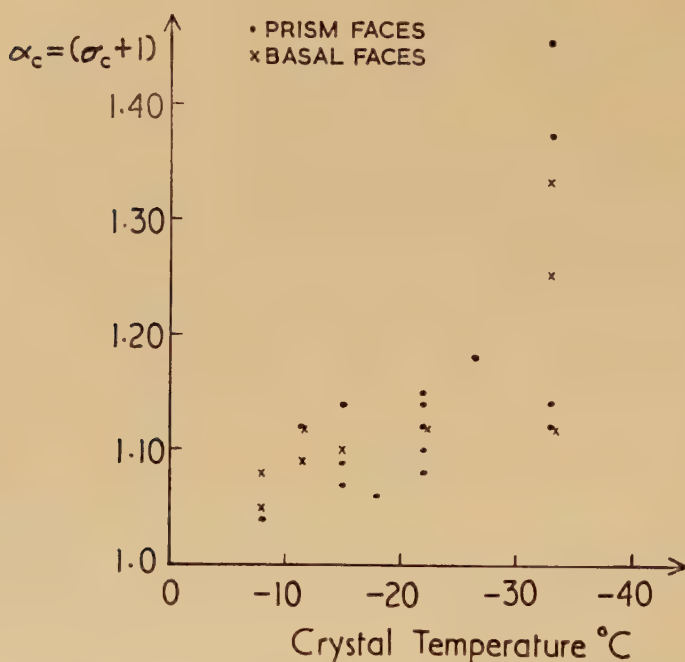
Values of $|U_c|$ plotted against supersaturation showing the critical saturation ratios required for growth and evaporation of crystal faces.

§ 8. VARIATION OF CRYSTAL HABIT WITH TEMPERATURE AND SUPERSATURATION

That the curves of growth rate plotted against supersaturation (figs. 6 (a), (b)) for the basal and prism faces were, in general, of constant slope indicates that the crystal habit defined by $\Gamma = \sqrt{(l'_c l'_a)}$ was generally independent of the supersaturation. This was confirmed by plotting Γ against the supersaturation for each of a large number of

crystals grown at the same temperature; for any given value of the supersaturation, there was a considerable spread in the values of Γ for different crystals but there was no obvious dependence of Γ on the supersaturation. The maximum and minimum values of Γ obtained at various fixed temperatures when the supersaturation was varied are shown in fig. 9. Remembering that values of $\Gamma < 1$ indicate a tendency towards plate-like growth and values of $\Gamma > 1$, a tendency towards columnar

Fig. 8

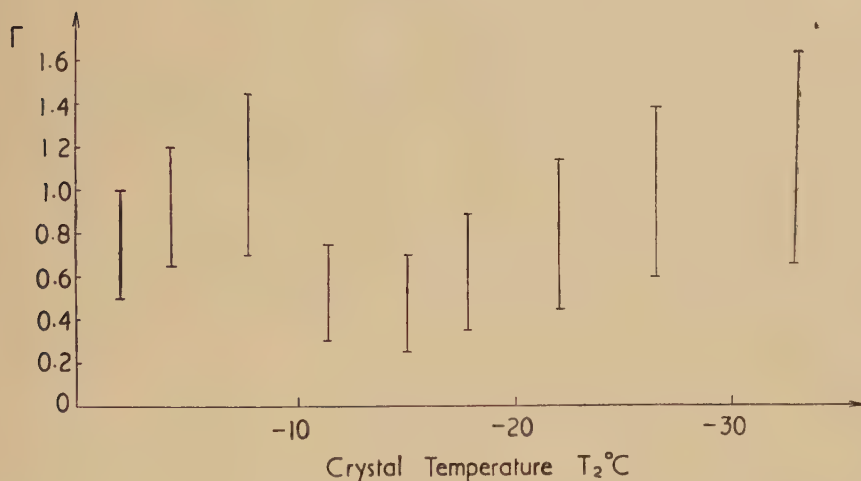


The critical saturation ratios for growth of basal and prism faces as a function of temperature.

development, fig. 9 suggests that there is a correlation between the temperature and the crystal habit, with a suggestion of the sequence plates-prisms-plates-prisms described in § 3. This indicates that the crystal habit is controlled much more by the temperature than by the supersaturation. The manner in which the crystal habit varied with temperature was brought out more clearly by confining attention to those crystals in each batch which had the largest growth rates (and so were probably least influenced by neighbouring crystals), and to regimes of supersaturation in which both $\sqrt{U_a}$ and $\sqrt{U_c}$ were proportional to σ , so that Γ was independent of the supersaturation. Values of Γ were obtained from the slopes of the $\sqrt{U}-\sigma$ plots (e.g. fig. 6), and are shown

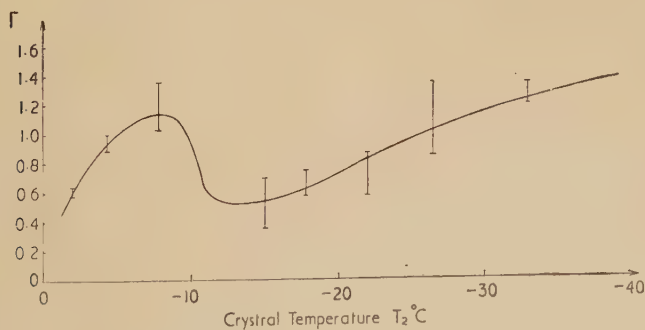
as a function of temperature in fig. 10. This indicates a tendency towards plate-like growth between 0 and -5°C , for prismatic columns between -5°C and -9°C , for plates between -9°C and -26°C and for prisms again below -26°C . Thus, in reducing the scatter in the observations occasioned by the individual peculiarities of each crystal, we have shown that the

Fig. 9



The maximum and minimum values of the limiting habit r obtained at various fixed temperatures when the supersaturation was varied.

Fig. 10



The limiting crystal habit $r = \frac{\partial}{\partial \sigma} \sqrt{U_c} / \frac{\partial}{\partial \sigma} \sqrt{U_a}$ as a function of temperature.

limiting crystal habit is determined largely by the temperature and that although the supersaturation controls very largely the *absolute* growth rate of a face, it appears to exert only a minor and non-systematic influence on the *relative* growth rates of the basal and prism faces.

REFERENCES

- AUFM KAMPE, H. F., WEICKMANN, H. K., and KELLY, J., 1951, *J. Met.*, **8**, 168.
BUNN, C. W., 1949, *Disc. Faraday Soc.*, 132.
FRANK, F. C., 1949, *Disc. Faraday Soc.*, 72.
GOLD, L. W., and POWER, B. A., 1951, *J. Met.*, **9**, 447.
HUMPHREYS-OWEN, S. P., 1949, *Disc. Faraday Soc.*, 144.
MASON, B. J., 1953, *Quart. J. Roy. Met. Soc.*, **79**, 104.
MASON, B. J., and OWSTON, P. G., 1952, *Phil. Mag.*, **43**, 911.
MARSHALL, J. S., and LANGLEBEN, M. P., 1954, *J. Met.*, **11**, 104.
OWSTON, P. G., 1951, *Q. art. Rev. Chem. Soc.*, **5**, 344.
WALL, E., 1947, *Wiss. Arbeit der Franz. Zone*, **1**, 151.
WEICKMANN, H. K., 1947, *Ber. Deutsch. Wetterdnst*, U.S. Zone, Rep. Trans., No. 716 (Völkenrode), M.O.S. (London); 1950, *Die Umschau*, **50**, 116.

XXX. *Theory of Ionization Fluctuations*

By J. E. MOYAL*

Department of Mathematics, The University, Manchester†

[Received August 20, 1954]

SUMMARY

The distributions of the loss of energy by ionization of a fast primary and of the numbers of ion pairs it produces are derived. It is shown that down to quite small values of the primary ionization, both can be represented by the same 'universal' distribution if the variables are reduced by a proper choice of scale and origin, which accounts for the experimental fact that ion pair numbers are proportional to primary energy loss. These conclusions remain valid when one takes into account quantum resonance effects and the details of atomic structure of the absorber.

§ 1. INTRODUCTION

THE main object of the present paper is to derive expressions for the distributions of (a) the loss of energy by ionization of a fast primary particle passing through an absorbing medium; (b) the numbers of ion-pairs produced by such a particle. We shall try in particular to explain the experimental fact that these two distributions are very approximately proportional to each other: i.e. that the energy lost by the primary particle per ion-pair produced is approximately constant (of the order of 35 ev).

Landau (1944) has shown that under certain simplifying assumptions, the distribution of energy loss can be expressed as a universal curve in terms of certain reduced energy variables (depending on the charge, mass and velocity of the primary, the atomic properties and the thickness of the absorber). We shall first derive a closed analytic expression for Landau's distribution. In view of discrepancies between this distribution and the results of recent experimental work (see West 1953) we shall examine possible departures from it due to: (a) small thicknesses of absorber; (b) the influence of the detailed atomic structure of the absorber; (c) the influence of quantum resonance effects in distant collisions. Finally, we shall derive a theoretical expression for the distribution of the numbers of ion pairs produced by the primary. This will allow us to decide whether these discrepancies can be due to the usual

* Communicated by G. D. Rochester.

† At present at the F.B.S. Falkiner Nuclear Research and Adolph Basser Computing Laboratories, School of Physics, The University of Sydney, Sydney, Australia.

assumption made in cloud chamber, ionization chamber and proportional counter work of a constant energy loss per ion-pair. The experimental evidence will be analysed in a forthcoming paper by Owen and Eyeions; a review of the subject by Price will appear in *Reports on Progress in Physics*.

§ 2. GENERAL EXPRESSION FOR THE IONIZATION ENERGY DISTRIBUTION

In deriving an expression for the ionization energy distribution, we shall make the following assumptions:

- (1) Successive ionizing collisions are statistically independent.
- (2) The total energy loss of the primary is very much smaller than its initial energy, and hence the decrease of primary energy may be neglected. Our theory will not therefore apply to slow primaries or great thicknesses of absorber. We also assume that energy losses due to radiation or nuclear interactions are negligible.
- (3) The absorbing medium has a homogeneous constitution.

We shall develop the theory first for an arbitrary total cross section $\sigma(E)$, where $N\sigma(E) dE dt$ is the probability of an energy loss between E and $E+dE$ in an absorber thickness dt , N being the number of absorber atoms per unit volume. The *primary ionization rate* is then

$$q = N \int_0^\infty \sigma(E) dE,$$

and the ionization energy distribution per collision is

$$\phi(E) = \frac{N\sigma(E)}{q}, \quad \text{with} \quad \int_0^\infty \phi(E) dE = 1$$

($q dt$ is the probability of an ionizing collision in the thickness dt , $\phi(E) dE$ the probability of an energy loss between E and $E+dE$ given that a collision has occurred).

Let $\chi(E, t) dE$ be the probability of an energy loss between E and $E+dE$ in a thickness t . It is easily seen to follow from assumptions (2.1), (2.2) and (2.3) that

$$\chi(E, t_1 + t_2) = \int_0^E \chi(E - W, t_1) \chi(W, t_2) dW. \quad \dots \quad (2.1)$$

For a small thickness δt , the probability that no energy is lost is $1 - q\delta t + o(\delta t)$; the probability of an energy loss between E and $E+dE$ is $q\phi(E) dE\delta t + o(\delta t)$; hence

$$\chi(E, \delta t) = (1 - q\delta t)\delta(E) + q\phi(E)\delta t + o(\delta t); \quad \dots \quad (2.2)$$

in particular, $\chi(E, 0) = \delta(E)$.*

We introduce the Laplace transform of $\chi(E, t)$:

$$M(\alpha, t) = \int_0^\infty \exp(-\alpha E) \chi(E, t) dE. \quad \dots \quad (2.3)$$

* The Dirac δ -function $\delta(E)$ should not be confused with δt .

It follows from (2.1) that

$$M(\alpha, t_1 + t_2) = M(\alpha, t_1)M(\alpha, t_2), \quad (2.4)$$

and hence from (2.2) and (2.4) (noting that $M(\alpha, 0) = 1$) that

$$\begin{aligned} \frac{\partial M(\alpha, t)}{\partial t} &= \lim_{\delta t \rightarrow 0} \frac{1}{\delta t} \{M(\alpha, \delta t) - 1\} M(\alpha, t) \\ &= \lim_{\delta t \rightarrow 0} \frac{1}{\delta t} \left\{ (1 - q\delta t) + q\delta t \int_0^\infty \exp(-\alpha E) \phi(E) dE + o(\delta t) - 1 \right\} M(\alpha, t) \\ &= \left\{ q \int_0^\infty [\exp(-\alpha E) - 1] \phi(E) dE \right\} M(\alpha, t). \end{aligned} \quad (2.5)$$

The solution of the differential eqn. (2.5) with initial condition $M(\alpha, 0) = 1$ is

$$M(\alpha, t) = \exp \left\{ qt \int_0^\infty [\exp(-\alpha E) - 1] \phi(E) dE \right\} = \exp [QR(\alpha)], \quad (2.6)$$

where $Q = qt$ is the mean number of collisions (i.e. the primary ionization) in the thickness t , and

$$R(\alpha) = \int_0^\infty [\exp(-\alpha E) - 1] \phi(E) dE. \quad (2.7)$$

The standard inversion formula for Laplace transforms then gives

$$\chi(E, Q) = \frac{1}{2\pi i} \int_{c-i\infty}^{c+i\infty} \exp[QR(z) + zE] dz \quad (2.8)$$

(it is convenient to express χ in terms of the mean collision number Q instead of the thickness t).

An asymptotic expansion for χ may be found from (2.8) by the saddle point method (see e.g. Jeffreys 1946 and Daniels 1954). As is usual in applications of this method, we can accept as a sufficient approximation to χ the first term of this expansion, namely, the expression

$$\chi(E, Q) dE = \frac{1}{c} [2\pi QR''(\alpha)]^{-1/2} \exp \{Q[R(\alpha) - \alpha R'(\alpha)]\} dE, \quad (2.9)$$

where α is related to E by the expression

$$E = -QR'(\alpha) = Q \int_0^\infty E \exp(-\alpha E) \phi(E) dE, \quad (2.10)$$

$$R''(\alpha) = \int_0^\infty E^2 \exp(-\alpha E) \phi(E) dE, \quad (2.11)$$

and c is a normalization constant, chosen to make

$$\int_0^\infty \chi(E, Q) dE = 1.$$

The most probable energy loss E_p is by definition the value of E for which $\chi(E, Q)$ is maximum. Maximizing the right-hand side of (2.9) with respect to α , we see that $E_p = -QR'(\alpha_p)$, where α_p is the solution of

$$R'''(\alpha_p) + 2Q\alpha_p[R''(\alpha_p)]^2 = 0. \quad (2.12)$$

The integral above is taken from 0 to ∞ because α decreases from ∞ to 0 as ϵ increases from 0 to ∞ . This can be seen from relation (2.9) which connects ϵ to α :

$$\frac{\epsilon}{Q} = -R'(\alpha) = \int_{\alpha}^{\infty} e^{-x} \frac{dx}{x} = -\text{Ei}(-\alpha); \quad . \quad . \quad . \quad (3.8)$$

the exponential integral $\text{Ei}(x)$ is tabulated (cf. Janke-Emde 1938 or *British Association Tables* 1951). For small values of α , however, ($\alpha \leq 1$), it is more convenient for computation purposes to transform (3.8) as follows:

$$\begin{aligned} \frac{\epsilon}{Q} &= \int_1^{\infty} e^{-x} \frac{dx}{x} + \int_0^1 (e^{-x} - 1) \frac{dx}{x} - \int_0^{\alpha} (e^{-x} - 1) \frac{dx}{x} - \log \alpha \\ &= -C - \log \alpha - \int_0^{\alpha} (e^{-x} - 1) \frac{dx}{x} \\ &= -C - \log \alpha - \sum_{n=1}^{\infty} (-1)^n \frac{\alpha^n}{n \cdot n!}, \quad . \quad . \quad . \quad (3.8a) \end{aligned}$$

where $C=0.577$ is Euler's constant. The numerical evaluation of χ is discussed in the next section in terms of corrections for small Q to Landau's universal distribution.

Substituting from the above in (2.12), we find the value of α_p of α which maximizes (3.6) by solving

$$2Q \exp(-\alpha_p) = 1 + \frac{1}{\alpha_p}, \quad . \quad . \quad . \quad (3.9)$$

graphically (fig. 1), and the corresponding most probable value of the energy loss ϵ_p from (3.8): ϵ_p is shown as a function of Q in fig. 2. It is seen that the equation has no solution for $Q < 2.44$, indicating that for such low values of Q , $\chi(\epsilon, Q)$ does not go through a maximum, but decreases more or less exponentially as ϵ increases. However, the accuracy of the saddle-point approximation is poor for such low Q ; for $Q \geq 5$, we see that $\alpha_p < 0.13$: hence we can approximate to (3.9) by the equation

$$\frac{1}{2Q} \frac{1}{\alpha_p} \left(1 + \frac{1}{\alpha_p} \right) = \frac{1}{\alpha_p} - 1, \quad . \quad . \quad . \quad (3.10)$$

whose solution is to a good approximation

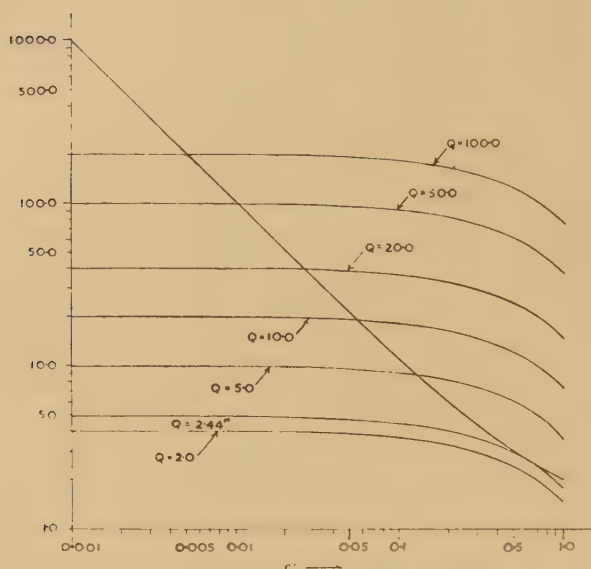
$$\frac{1}{\alpha_p} = 2Q - 2 - \frac{1}{2Q - 1}, \quad . \quad . \quad . \quad (3.11)$$

Taking the first three terms in the right-hand side of (3.9) we obtain for the most probable energy loss the approximate expression

$$\epsilon_p = \frac{E_p}{E_0} = Q \left\{ \log \left(2Q - 2 - \frac{1}{2Q - 1} \right) - C + \frac{2Q - 1}{(2Q - 2)(2Q - 1) - 1} \right\}, \quad (3.12)$$

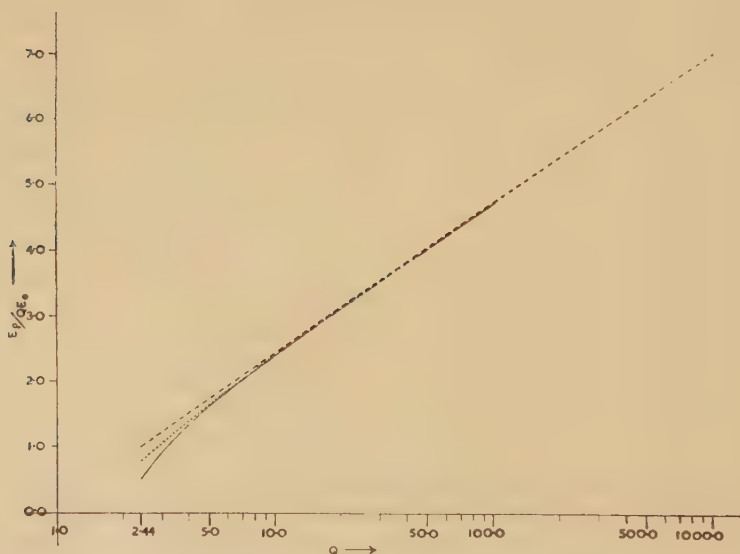
which for $Q \geq 5$ departs by less than 1% from the value obtained by the graphical solution of (3.9) (cf. fig. 2).

Fig. 1



Solution of eqn. (3.9): the values of ν_p are given by the abscissae of the intersections of the curve $1 + 1/\nu$ with the curves $2Qe^{-\nu}$ for values of $Q = 2.44, 5, 10, 20, 50, 100$; there is no intersection (and hence no maximum) for $Q < 2.44$.

Fig. 2



The most probable energy loss E_p (in units QE_0) as a function of the primary ionization Q : the full curve is obtained by numerical solution of eqn. (3.9), the dotted and dashed curves represent respectively the approximations of eqn. (3.12), and (4.4).

§ 4. THE LANDAU APPROXIMATION

One finds that for large Q , the major contribution to $\chi(\epsilon, Q)$ in (3.6) comes from small values of α (as we have seen, α_p is small for $Q \geq 5$, and the curve for χ is sharply centred about ϵ_p). Hence, following Landau, we obtain an asymptotic expression for χ valid for large Q by neglecting terms of order α compared to $\log \alpha$: thus, we take

$$R(\alpha) = \alpha(C - 1 + \log \alpha). \quad (4.1)$$

Substituting these values, (3.6) and (3.8 a) become

$$\chi(\epsilon, Q) d\epsilon = \frac{1}{c} \sqrt{\left(\frac{\alpha}{2\pi Q}\right)} \exp(-Q\alpha) d\epsilon,$$

where
$$c = \frac{1}{\sqrt{(2\pi)}} \int_0^\infty \exp(-Q\alpha) \frac{Q d\alpha}{\sqrt{(Q\alpha)}} = \frac{1}{\sqrt{2}}, \quad (4.2)$$

$$\frac{\epsilon}{Q} = -C - \log \alpha. \quad (4.3)$$

To the same order of approximation, we may take for the most probable values

$$\alpha_p' = \frac{1}{2Q} \quad \text{and} \quad \frac{\epsilon_p'}{Q} = \frac{E_p'}{BZt} = -C + \log 2Q. \quad (4.4)$$

Changing to the *reduced energy variable*

$$\omega = \frac{\epsilon - \epsilon_p'}{Q} = \frac{E - E_p'}{BZt} = -\log 2Q\alpha, \quad (4.5)$$

we find the following explicit expression for Landau's distribution

$$\chi_L(\omega) d\omega = \frac{1}{\sqrt{(2\pi)}} \exp\left\{-\frac{1}{2}[\omega + \exp(-\omega)]\right\} d\omega. \quad (4.6)$$

The *half-width* $\Delta\omega$ of this distribution is easily found to be $\Delta\omega = 3.58$.

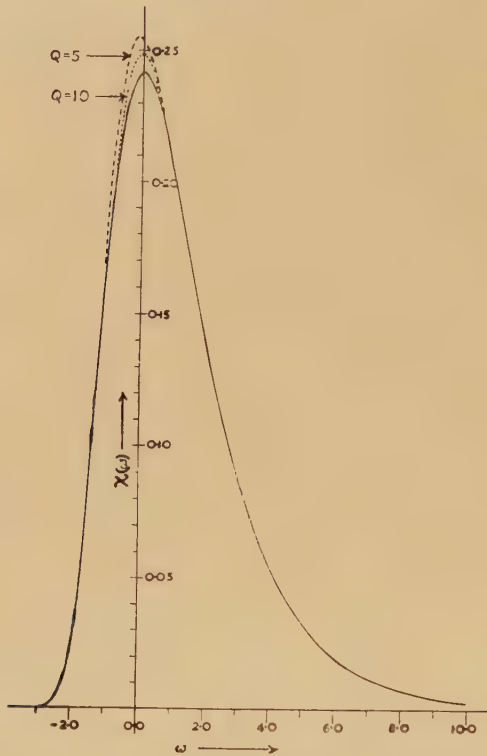
We see thus that the asymptotic expression for χ has a 'universal' form independent of Q when the energy is expressed in terms of the reduced variable ω . The accuracy of this expression has been assessed by computing χ for small values of Q from the more accurate expression (3.6) and changing over to the reduced variable (4.5): the results are shown in fig. 3. Surprisingly, *no appreciable departure is found from Landau's distribution for $Q \geq 20$* ; the departure for $Q=10$ and $Q=5$ is indicated on the figure by dotted lines. We must mention that the expressions for Q and E_p above are not the same as Landau's: the relativistic log rise with increasing energy is absent, because we have neglected quantum resonance effects (see the discussion at the end of § 6).

§ 5. EFFECTS OF ATOMIC STRUCTURE

In order to assess the detailed effects of the atomic structure of the absorber on the distribution of ionization energy, we shall use a crude

classical model: we assume that the classical cross section is valid for the electrons in each shell of the atom, with a minimum transferable energy

Fig. 3



Distribution of primary energy loss: the full curve is Landau's 'universal' distribution (4.6), the dashed curve is computed from eqns. (3.6) and (3.8), for $Q=5$ and 10 .

equal to the ionization potential of the shell. Let I_j be the ionization potential of the j th electron, $j=1, 2, \dots, Z$; then the total cross section is

$$\sigma(E) dE = \sum_{j=1}^Z \sigma_j(E) dE, \text{ with } N\sigma_j(E) = \begin{cases} B/E^2 & \text{for } E \geq I_j, \\ 0 & \text{,, } E < I_j. \end{cases} \quad (5.1)$$

where B has the same definition as in eqn. (3.2). Then

$$Q = Nt \int_0^\infty \sigma(E) dE = Bt \sum_{j=1}^Z \int_{I_j}^\infty \frac{dE}{E^2} = Bt \sum_{j=1}^Z \frac{1}{I_j} = \frac{BZt}{E_a}, \quad (5.2)$$

where

$$\frac{Z}{E_a} = \sum_{j=1}^Z \frac{1}{I_j}, \quad \dots \dots \dots (5.3)$$

and

$$\phi(E) dE = \frac{E_a}{BZ} N \sum_{j=1}^Z \sigma_j(E) dE. \quad \dots \dots \dots (5.4)$$

(Changing to the energy variable $\epsilon = E/E_a$, and substituting in the expressions of § 2, we find $R(\alpha)$ and hence $\chi(\epsilon, Q)$. It turns out that an asymptotic expression for χ similar to that derived in § 4 is valid for values of $Q \geq 20$. Restricting our attention to this case, we find that to the same order of approximation as in § 4,

$$R(\alpha) = \alpha \left[C + 1 - \log \left(\frac{\alpha E_b}{E_a} \right) \right], \quad . \quad . \quad . \quad . \quad . \quad (5.5)$$

where $\log E_b = (1/Z) \sum_{j=1}^Z \log I_j$. (Note that $\bar{E} = BZt \log (E_m/E_b)$; i.e. in the present classical model, E_a and E_b are the average ionization potentials appropriate for the calculation of respectively the primary ionization Q and the average energy loss \bar{E} .) We then find for the most probable values $\alpha_p' = 1/2Q$, and hence

$$\begin{aligned} \frac{\epsilon_p'}{Q} - \frac{E_p'}{BZt} &= -C + \log \frac{2QE_a}{E_b} \\ &= -C + \log \frac{2BZt}{E_b}. \quad . \quad . \quad . \quad . \quad (5.6) \end{aligned}$$

Introducing the reduced energy variable

$$\omega = \frac{\epsilon - \epsilon_p'}{Q} = \frac{E - E_p'}{BZt} = -\log 2Q\alpha, \quad . \quad . \quad . \quad . \quad (5.7)$$

we see at once that the asymptotic distribution is exactly the same as Landau's, namely

$$\chi_L(\omega) d\omega = \frac{1}{\sqrt{(2\pi)}} \exp \left\{ -\frac{1}{2} [\omega + \exp(-\omega)] \right\} d\omega. \quad . \quad . \quad (5.8)$$

Thus, the details of atomic structure, with the assumptions made above, have no effect on the asymptotic distribution* but only modify the expression for the average number of collisions Q and the most probable energy loss E_p ; these conclusions are not likely to be modified by any more refined theory of these effects, though we may expect improvements in the expressions for Q and E_p .

§ 6. QUANTUM RESONANCE EFFECTS

The classical cross section proportional to $1/E^2$ is valid for values of $E \gg I$, the average ionization potential of the absorber. Its failure in case $\epsilon^2/\hbar v = c/137v \ll 1$ (where \hbar is $\frac{1}{2}\pi$ times Planck's constant) may be ascribed to quantum resonance effects in distant collisions, which increase the cross section for values of E near I , and consequently approximately double the mean energy loss (see e.g. Bohr, *loc. cit.*, p. 89 for a discussion). In order to assess the effect of this resonant increase on the ionization

* Blunk *et al.* (1950, 1951) appear to arrive at a contrary conclusion.

energy distribution, we shall postulate (since an exact expression is not available) a cross section

$$\sigma(E) dE = \frac{BZ}{N} \frac{dE}{(E-I)^2 + \Gamma^2}, \quad (6.1)$$

of the usual form for quantum resonance effects, Γ being the half-width of the resonance curve. We expect that $\Gamma < I$; hence σ is approximately equal to the classical cross section when $E \gg I$. In calculating the ionization energy distribution, we must set $\sigma(E) = 0$ for non-ionizing collisions where $E < I$. Hence

$$\left. \begin{aligned} Q &= Nt \int_I^\infty \sigma(E) dE = BZt \int_I^\infty \frac{dE}{(E-I)^2 + \Gamma^2} = BZt \int_0^\infty \frac{dx}{x^2 + \Gamma^2} = \frac{\pi}{2} \frac{BZt}{\Gamma}, \\ \phi(E) dE &= \frac{2\Gamma}{\pi} \frac{dE}{(E-I)^2 + \Gamma^2}. \end{aligned} \right\} \quad (6.2)$$

Transforming to the energy variable $\epsilon = (E-I)/\Gamma$ and substituting in the expressions of § 2, we find that

$$R(\alpha) = \frac{2}{\pi} \int_0^\infty [\exp(-\alpha\epsilon) - 1] \frac{d\epsilon}{1 + \epsilon^2} = -1 + \frac{2}{\pi} (\sin \alpha \operatorname{Ci} \alpha - \cos \alpha \operatorname{si} \alpha), \quad (6.3)$$

where $\operatorname{Ci} \alpha$, $\operatorname{si} \alpha$ are the cosine and sine integrals respectively (cf. Jahnke-Emde, *loc. cit.*, p. 3). For the same reasons as in § 5, we need only consider the asymptotic distribution. It is easily seen from the series expansions of $\operatorname{Ci} \alpha$, $\operatorname{si} \alpha$ that to the same order of approximation as in § 4,

$$R(\alpha) = \frac{2}{\pi} \alpha (C - 1 + \log \alpha), \quad (6.4)$$

$$\alpha_p' = \frac{\pi}{4Q}, \quad \text{and hence} \quad \frac{\epsilon_p'}{Q} = \frac{2}{\pi} \frac{E_p' - I}{BZt} = \frac{2}{\pi} \left(\log \frac{4Q}{\pi} - C \right). \quad (6.5)$$

Hence we see that as in § 5, if we change over to the reduced energy variable

$$\omega = \frac{\epsilon - \epsilon_p'}{Q} = \frac{2}{\pi} \frac{E - E_p'}{BZt} = \log \left(\frac{\pi}{4Q\alpha} \right), \quad (6.6)$$

then the asymptotic energy distribution takes the 'universal' form

$$\chi_L(\omega) d\omega = \frac{1}{\sqrt{2\pi}} \exp \left\{ -\frac{1}{2} [\omega + \exp(-\omega)] \right\} d\omega. \quad (6.7)$$

Thus quantum resonance effects too modify only the expressions for Q and E_p , but not that for $\chi_L(\omega)$, and here again a more exact theory of these effects is unlikely to change these conclusions (though we may expect a modification of the expressions (6.2) and (6.7) for Q and E_p). An estimate of Γ may be obtained by equating the primary ionization rate q with the value calculated by Bethe (1933)

$$q = \frac{BZ}{I_0} r \left\{ \log \frac{2\mu c^2 \beta^2}{I_0(1-\beta^2)} + s - \beta^2 \right\} = \frac{2}{\pi} \frac{BZ}{\Gamma},$$

where $\beta = v/c$, I_0 is the outer shell ionization potential, r and s are constants depending on the absorber (for hydrogen, $r=0.285$ and $s=3.04$). With this estimate, Q and E_p exhibit a relativistic log rise with increasing energy similar to the expressions given by Landau (*loc. cit.*). Alternatively, one may estimate Γ from the experimental values found for q .

§ 7. THE DISTRIBUTION OF NUMBERS OF ION PAIRS

The production of ions by a fast primary particle constitutes a multiplicative or branching stochastic process: the electron ejected in a primary ionizing collision may, if it has enough energy, ionize another atom; the secondary electrons may then ionize again, and so on, the process ending when all secondaries have become too slow to ionize further. We shall develop the theory under the assumption that the collection or recording of ions is delayed long enough for the process to terminate, so that the ion pair distribution per collision is the same for all collisions: this assumption is valid as a rule in ionization or cloud chamber work: post-expansion cloud chamber tracks form however an exception, since they record only the primary ionization. We shall also neglect extraneous effects such as increase in ionization due to acceleration of the electrons in electrode fields and to photoelectric effects in the gas or chamber walls, which become important in proportional counter work.

Let then q_k be the probability that k ion pairs are produced in any given ionizing collision, with $k=1, 2, \dots$ and $\sum q_k=1$; let $p_n(t)$ be the probability that a total number n of ion pairs is produced in an absorber thickness t , and write q as before for the primary ionizing collision rate. It then follows from assumptions (2.1), (2.2) and (2.3) that

$$p_n(t_1+t_2) = \sum_{j=0}^n p_j(t_1) p_{n-j}(t_2), \quad . \quad . \quad . \quad . \quad . \quad (7.1)$$

$$p_n(t+\delta t) = (1-q\delta t)\delta_{n0} + qq_n\delta t + o(\delta t). \quad . \quad . \quad . \quad . \quad (7.2)$$

Introducing the Laplace transform of the ion pair distribution $p_n(t)$

$$M(\alpha, t) = \sum_{n=0}^{\infty} e^{-n\alpha} p_n(t), \quad . \quad . \quad . \quad . \quad . \quad (7.3)$$

we find as in § 2 that

$$M(\alpha, t_1+t_2) = M(\alpha, t_1) \cdot M(\alpha, t_2), \quad . \quad . \quad . \quad . \quad (7.4)$$

$$\frac{\partial M(\alpha, t)}{\partial t} = \left\{ q \sum_{n=1}^{\infty} (e^{-n\alpha} - 1) q_n \right\} M(\alpha, t), \quad . \quad . \quad . \quad . \quad (7.5)$$

and hence that

$$M(\alpha, t) = \exp \left\{ qt \sum_{n=1}^{\infty} (e^{-n\alpha} - 1) q_n \right\} = \exp [QR(\alpha)], \quad . \quad . \quad (7.6)$$

where $Q=qt$ as before, and

$$R(\alpha) = \sum_{n=1}^{\infty} (e^{-n\alpha} - 1) q_n. \quad . \quad . \quad . \quad . \quad (7.7)$$

The inversion of the Laplace transform (7.6) is given by the well-known formula

$$p_n(Q) = \frac{1}{2\pi i} \int_{c-\pi i}^{c+\pi i} \exp [QR(z) + nz] dz. \quad (7.8)$$

This integral can be evaluated by the saddle-point method: the first approximation to it (which may be assumed as previously sufficiently accurate for our purpose) is

$$p_n(Q) = \frac{1}{c} [2\pi QR''(\alpha_n)]^{-1/2} \exp \{Q[R(\alpha_n) - \alpha_n R'(\alpha_n)]\}, \quad (7.9)$$

where α_n is related to n by

$$n = -QR'(\alpha_n) = Q \sum_{k=1}^{\infty} k \exp(-k\alpha_n) q_k, \quad (7.10)$$

$$R''(\alpha) = \sum_{k=1}^{\infty} k^2 \exp(-k\alpha) q_k,$$

and c is as before a normalization constant

$$\begin{aligned} c &= \sum_{n=0}^{\infty} [2\pi QR''(\alpha_n)]^{-1/2} \exp \{Q[R(\alpha_n) - \alpha_n R'(\alpha_n)]\} \\ &\simeq \frac{1}{\sqrt{(2\pi)}} \int_{\alpha_0}^{\alpha_{\infty}} [QR''(\alpha)] \exp \{Q[R(\alpha) - \alpha R'(\alpha)]\} d\alpha + \frac{1}{2} p_0(t). \end{aligned} \quad (7.11)$$

The last approximate expression for c is obtained by the use of Euler's summation formula, with $\alpha_0, \alpha_{\infty}$ corresponding respectively by (7.10) to $n=0$ and $n=\infty$. These expressions are close analogues of those found in § 2. Similarly, the most probable number of ion pairs is, as in § 2, the number n_p (which need no longer be an integer) corresponding by (7.10) to the solution α_p of

$$R'''(\alpha_p) + 2Q\alpha_p [R''(\alpha_p)]^2 = 0. \quad (7.12)$$

§ 8. ION PAIR DISTRIBUTION WITH THE CLASSICAL CROSS SECTION

We shall now develop the theory of ion pair distribution for the following crude model: we assume the classical cross section for ionization by the secondary electrons as well as by the primary particle, and set this cross section equal to zero if the energy of the electron is less than the mean ionization potential I of the absorber. Let E_0 be the energy of the primary particle, E_1, E_2, \dots those of the secondary electrons successively ejected in the chain process resulting from a single primary ionizing collision. The total cross section $\sigma(E; E_k) dE$ for an ionization energy loss between E and $E+dE$ by the k th electron of energy E_k is

$$\sigma(E; E_k) = \begin{cases} \left(\frac{\pi \epsilon^4}{E_k} \right) \frac{1}{E^2} & \text{if } E_k \geq I \quad \text{and} \quad E \leq E_k, \\ 0 & \text{if } E_k < I \quad \text{or} \quad E > E_k; \end{cases} \quad (8.1)$$

hence, its collision probability per unit thickness is

$$\lambda(E_k) = \begin{cases} N \int_I^{E_k} \sigma(E; E_k) dE = \frac{\pi \epsilon^4 N}{E_k} \left(\frac{1}{I} - \frac{1}{E_k} \right) & \text{if } E_k \geq I, \\ 0 & \text{if } E_k < I, \end{cases} \quad (8.2)$$

while the probability that it should *not* ionize further in a thickness t is

$$\kappa(E_k, t) = \exp[-\lambda(E_k)t] = \begin{cases} \exp\left\{-\frac{\pi \epsilon^4 N}{E_k} \left(\frac{1}{I} - \frac{1}{E_k} \right) t\right\} & \text{if } E_k \geq I, \\ 1 & \text{if } E_k < I. \end{cases} \quad (8.3)$$

The probability that the primary collision produce a first electron of energy between E_1 and $E_1 + dE_1$ is $I dE_1 / (E_1 + I)^2$: hence, the probability that just one ion pair be produced in a thickness t is

$$\int_0^\infty \kappa(E_1, t) \frac{I dE_1}{(E_1 + I)^2} = \frac{1}{2} + \frac{I^2}{\pi \epsilon^4 N t} [1 - \exp(-\pi \epsilon^4 N t / 2 I^2)]. \quad (8.4)$$

The second term in the right-hand side of (8.4) is negligible for any reasonably large value of t (if e.g. $I = 25$ ev then for a monoatomic gas $\pi \epsilon^4 N / I^2 \simeq 2.8 \times 10^3 \text{ cm}^{-1}$); hence the probability q_1 of exactly one ion pair per collision is just the probability that the first electron has an energy $\leq I$: i.e. $q_1 = \frac{1}{2}$. Similarly, we can simplify the calculation of q_2, q_3, \dots by setting $\kappa(E, t) = 0$ for $E > I$ and letting $t \rightarrow \infty$ in the final result.

The calculations get progressively more complicated for the succeeding q_k : details for q_2 will be found in the Appendix. However, the distribution

$$q_k = \frac{a}{k^2 + 1}, \quad (k = 1, 2, \dots) \quad (8.5)$$

(where a is a normalization constant chosen to make $\sum q_k = 1$) fits approximately the first few q_k , and has the right sort of behaviour for large k (analogous to the $1/E^2$ law for the distribution of energy loss per collision). The value of a may be obtained from the formula (see e.g. Knopp 1928)

$$\sum_{k=1}^\infty \frac{1}{k^2 + 1} = \frac{\pi}{2} \coth \pi - \frac{1}{2} = 1.077; \quad \text{hence } a = 0.929. \quad (8.6)$$

The distribution q_k is independent of I : this gives us some confidence in its approximate validity in spite of the neglect of inner shell contributions. In fact, it appears from a rough estimate of the latter's effect, using the model of § 5, that the q_k are not appreciably modified, provided that the inner shell ionization potentials are much greater than that of the outer shell.

Substitution of (8.9) in the expressions of § 7 gives

$$\frac{1}{a} R(\alpha) = \sum_{k=1}^\infty \frac{e^{-k\alpha} - 1}{k^2 + 1}; \quad \frac{1}{a} R'(\alpha) = - \sum_{k=1}^\infty \frac{k e^{-k\alpha}}{k^2 + 1}; \quad \frac{1}{a} R''(\alpha) = \sum_{k=1}^\infty \frac{k^2 e^{-k\alpha}}{k^2 + 1}. \quad (8.7)$$

The series above converge very slowly for small values of α ; for the purposes of computation, we transform the last two as follows:

$$\left. \begin{aligned} \frac{1}{a} R'(\alpha) &= \sum_{k=1}^{\infty} \frac{e^{-k\alpha}}{k(k^2+1)} - \sum_{k=1}^{\infty} \frac{e^{-k\alpha}}{k} = \sum_{k=1}^{\infty} \frac{e^{-k\alpha}}{k(k^2+1)} + \log(1-e^{-\alpha}), \\ \frac{1}{a} R''(\alpha) &= \sum_{k=1}^{\infty} e^{-k\alpha} - \sum_{k=1}^{\infty} \frac{e^{-k\alpha}}{k^2+1} = \frac{1}{e^{\alpha}-1} - \frac{1}{a} [R(\alpha)+1]. \end{aligned} \right\} \quad (8.8)$$

For values of $\alpha < 0.04$, it is more convenient to compute by numerical integration from the following transformed expression:

$$\left. \begin{aligned} \frac{1}{a} [R(\alpha)+1] &= \int_{\alpha}^{\infty} \frac{\sin(\theta-\alpha)}{e^{\theta}-1} d\theta \\ &= \cos \alpha \left\{ \sum_{k=1}^{\infty} \frac{1}{k^2+1} - \int_0^{\alpha} \frac{\sin \theta}{e^{\theta}-1} d\theta \right\} + \sin \alpha \\ &\quad \times \left\{ \log(1-e^{-\alpha}) + \sum_{k=1}^{\infty} \frac{1}{k(k^2+1)} - \int_0^{\alpha} \frac{1-\cos \theta}{e^{\theta}+1} d\theta \right\}, \\ \frac{1}{a} R'(\alpha) &= - \int_{\alpha}^{\infty} \frac{\cos(\theta-\alpha)}{e^{\theta}-1} d\theta = -\sin \alpha \left\{ \sum_{k=1}^{\infty} \frac{1}{k^2+1} - \int_0^{\alpha} \frac{\sin \theta}{e^{\theta}-1} d\theta \right\} \\ &\quad + \cos \alpha \left\{ \log(1-e^{-\alpha}) + \sum_{k=1}^{\infty} \frac{1}{k(k^2+1)} - \int_0^{\alpha} \frac{1-\cos \theta}{e^{\theta}-1} d\theta \right\}. \end{aligned} \right\} \quad (8.9)$$

The substitution of these expressions in (7.9) and (7.10), taking $Q=BZt/I$, yields the ion pair distribution $p_n(Q)$: in order to compare it with that of the ionization energy, it is important to evaluate its asymptotic expression for large Q . It is easily seen from the transformed expressions (8.9) that to the same order of approximation as in § 4,

$$R(\alpha) = a\alpha(b-1+\log \alpha); \quad \alpha_p' = \frac{1}{2Qa}; \quad \frac{n_p'}{Qa} = -b + \log 2Qa; \quad . \quad (8.10)$$

where a is defined by (8.6) and $b = \sum 1/k(k^2+1) = 0.672$. Substituting in (7.9) and changing to the reduced variable

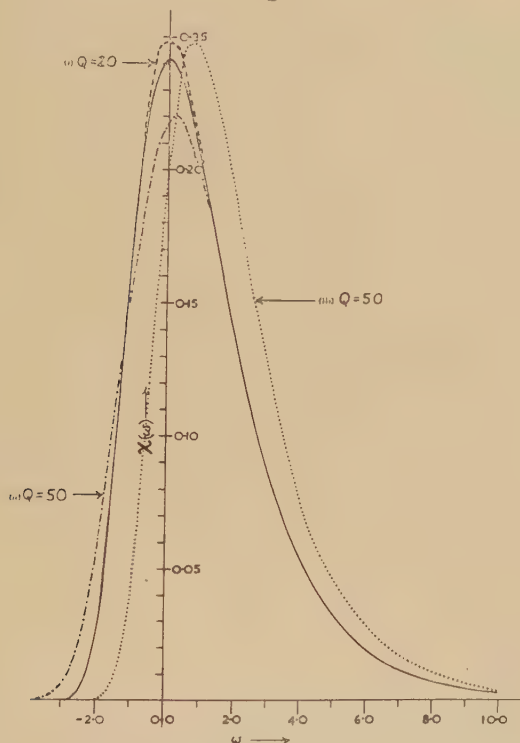
$$\omega = \frac{n-n_p'}{Qa} = -\log 2Qa\alpha, \quad . \quad . \quad . \quad (8.11)$$

we are led again, as in the case of ionization energy, to Landau's 'universal' distribution: that is, we find that

$$\left. \begin{aligned} p_n(Q) &= \frac{1}{Qa} \chi_L \left(\frac{n-n_p'}{Qa} \right), \\ \text{where } \chi_L(\omega) &= \frac{1}{\sqrt{(2\pi)}} \exp \left\{ -\frac{1}{2} [\omega + \exp(-\omega)] \right\}. \end{aligned} \right\} \quad . \quad . \quad . \quad (8.12)$$

The deviation from Landau's distribution for small values of Q is somewhat more marked than is the case for the energy loss distribution: it is shown in fig. 4, where $Qap_n(Q)$, computed from expressions (8.8) and (8.9) for $Q=20$, is plotted against ω .

Fig. 4



Distribution of numbers of ion pairs: the full curve is Landau's distribution (8.12), curve (i) is computed with the classical cross section, § 8 for $Q=20$, curves (ii) and (iii) with the quantum resonance cross section, § 9, for $Q=50$ and respectively $g=0.17$ and 0.50 .

§ 9. ION PAIR DISTRIBUTION WITH QUANTUM RESONANCE EFFECTS

The effect of quantum resonance is to increase the primary energy loss cross section for values of the energy near the ionization potential I , and hence to increase the probability q_1 of producing a single ion pair per collision. Repeating the calculations of § 8 with the cross section (6.1) for the primary, and the classical cross section for the (slow) ejected electrons, we find that

$$q_1 = \frac{2\Gamma}{\pi} \int_0^I \frac{dE_0}{E_0^2 + \Gamma^2} = \frac{2}{\pi} \tan^{-1} \frac{I}{\Gamma}. \quad (9.1)$$

For relativistic primaries, where I/Γ is large, we have approximately

$$q_1 \simeq 1 - \frac{2}{\pi} \frac{\Gamma}{I}. \quad (9.1a)$$

Continuing the calculations in the same way, one finds that the distribution q_k can be fitted approximately by the relation

$$q_k = g \left(\frac{a}{k^2 + 1} \right), \quad \text{where} \quad g = \frac{4}{\pi(2-a)} \frac{\Gamma}{I} = 1.190 \frac{\Gamma}{I}, \quad (k=2, 3, \dots); \quad (9.2)$$

one can easily verify that $\sum_1^\infty q_k = 1$. This may be interpreted by saying that at every collision there is a chance $1-g$ of a resonant collision, and a chance g of a non-resonant one, given which the distribution of ion pairs is the same as in § 8.

Let us now write $R_c(\alpha)$, $R_c'(\alpha)$, etc. for the expressions found in § 8. and $R_Q(\alpha)$, $R_Q'(\alpha)$, etc. for those corresponding to the quantum resonance cross section. It then follows from the foregoing that

$$R_Q(\alpha) = (1-g)(e^{-\alpha} - 1) + gR_c(\alpha); \quad R_Q'(\alpha) = -(1-g)e^{-\alpha} + gR_c'(\alpha); \quad (9.3)$$

and so on. To the same order of approximation as in § 4, we then have

$$\left. \begin{aligned} R_Q(\alpha) &= -(1-g)\alpha + ga\alpha(b-1+\log \alpha); \\ R_Q'(\alpha) &= -(1-g) + ga(b+\log \alpha); \quad \text{etc.} \end{aligned} \right\} \quad \dots \quad (9.4)$$

and hence

$$\alpha_p' = \frac{1}{2Qga} = \frac{1}{2.21Q} \frac{I}{\Gamma}; \quad n_p' = Q[1-g+ga(\log 2Qga-b)], \quad (9.5)$$

where $Q = \pi BZt/2\Gamma$. Substituting in (7.9) in terms of the reduced variable

$$\omega = \frac{n-n_p'}{Qga} = -\log 2Qga\alpha, \quad \dots \quad (9.6)$$

we find as in § 8 that

$$\left. \begin{aligned} p_n(Q) &= \frac{1}{Qga} \chi_L \left(\frac{n-n_p'}{Qga} \right), \\ \text{where} \quad \chi_L(\omega) &= \frac{1}{\sqrt{(2\pi)}} \exp \left\{ -\frac{1}{2} [\omega + \exp(-\omega)] \right\}. \end{aligned} \right\} \quad \dots \quad (9.7)$$

The deviation from Landau's distribution is more pronounced than is the case with the ion pair distribution found in § 8, but is still not very marked. This may be seen in fig. 4, where the curves of $Qgap_n(Q)$ as a function of ω , computed from expressions (9.3), are shown for $Q=50$, $g=0.5$ and $g=0.17$. We may remark that if Γ is evaluated by equating $q=\pi BZ/2\Gamma$ to the experimental values of primary ionization (cf. § 6), one finds that near minimum ionization g is approximately equal to $\frac{1}{2}$ for most gases.

The tendency of the ion pair distribution to the same (Landau) distribution as the primary energy loss accounts (at least in the case of fast primaries) for the experimental fact that the energy lost per ion pair is a constant, approximately independent of the primary energy: furthermore, we may presume that this result is not sensitive to the actual value of the cross section, since it holds for both the classical

(§8) and the quantum resonance (§9) cross sections. Comparing the expressions for ω in §§8 and 9 with those respectively in §§4 and 6, we see that the energy per ion pair must be approximately equal to the average ionization potential. This is substantially less than the experimental values (of the order of 35 eV), presumably because the latter refers to total energy loss, including excitation of the atoms, whereas our calculations refer to energy lost by ionization only. Furthermore, the use of a single average ionization potential is undoubtedly a very rough approximation, especially at the higher atomic numbers, where inner shell ionization and excitation, Auger effects and the like must contribute substantially to ionization and primary energy loss. We cannot in fact expect the theory in the present section to have more than qualitative validity for elements heavier than helium.

§ 10. CONCLUSIONS

We conclude from the foregoing:

(1) That Landau's 'universal' distribution appears to be valid for both primary energy loss and numbers of ion pairs, which explains their proportionality in the case of fast primaries.

(2) That it remains valid down to unexpectedly small values of the primary ionization Q .

(3) That none of the effects considered in this paper (atomic structure, quantum resonance, proportionality of numbers of ion pairs to primary energy loss) explain the experimentally found deviations from it.

ACKNOWLEDGMENTS

It is a pleasure for me to acknowledge my indebtedness to Dr. B. G. Owen and Mr. D. A. Eyeions, at whose request I considered the present problem, for many invaluable discussions and suggestions. I am also greatly indebted to Mrs. A. Linnert, who carried out the computations and drew the graphs.

REFERENCES

- BETHE, 1933, *Handbuch der Physik* (Berlin: Springer), Vol. 24, 1, p. 518.
 BLUNCK and LEISEGANG, 1950, *Z. Phys.*, **128**, 500.
 BLUNCK and WESTPHAL, 1951, *Z. Phys.*, **130**, 641.
 BOHR, 1948, *The Penetration of Atomic Particles through Matter* (Copenhagen: Det Kgl. Danske Videnskabernes Selskab), pp. 64, 76, 80.
 BRITISH ASSOCIATION TABLES, 1951 (Cambridge: University Press), Vol. 1, 3rd edn., pp. 31-33.
 DANIELS, 1955, *Annals of Math. Statistics* (to be published).
 JAHNKE-EMDE, 1938, *Tables of Functions* (New York: Dover Publications), 2nd edn., pp. 6-8.
 JEFFREYS and JEFFREYS, 1946, *Methods of Mathematical Physics* (Cambridge: University Press), 1st edn., pp. 472-6.
 KNOPP, 1928, *Theory and Application of Infinite Series* (London and Glasgow: Blackie), p. 378.
 LANDAU, 1944, *J. Phys. U.S.S.R.*, **8**, 201.
 WEST, 1953, *Proc. Phys. Soc. A*, **66**, 306.

APPENDIX

Calculation of q_2

In order to evaluate q_2 , we note first that the probability that electron 1, of energy $E_1 \geq I$, suffer an ionizing collision between thicknesses τ and $\tau + d\tau$, thereby producing electrons 2 and 3 with energies respectively between E_2 , $E_2 + dE_2$ and E_3 , $E_3 + dE_3$, where $E_3 = E_1 - E_2 - I$, and that electrons 2 and 3 ionize no further between thicknesses τ and t , is

$$\kappa(E_1\tau) \cdot N\sigma(E_2; E_1) dE_2 d\tau \cdot \kappa(E_2, t-\tau) \cdot \kappa(E_1 - E_2 - I, t-\tau), \quad (A1)$$

where σ and κ are given respectively by eqns. (8.1) and (8.3). We then obtain q_2 by multiplying (A1) by the probability distribution $IdE_1/(E_1 + I)^2$ of electron 1, integrating with respect to E_2 (from 0 to $E_1 - I$), to E_1 (from I to ∞), to τ (from 0 to t), and finally making $t \rightarrow \infty$: thus

$$q_2 = \lim_{t \rightarrow \infty} \int_I^\infty \frac{IdE_1}{(E_1 + I)^2} \int_0^t \kappa(E_1, \tau) d\tau \int_0^{E_1 - I} \sigma(E_2; E_1) \kappa(E_2, t-\tau) \times \kappa(E_1 - E_2 - I, t-\tau) dE_2. \quad (A2)$$

The only positive contribution to q_2 in the above comes from the range of values of E_1 and E_2 which make E_2 and $E_3 = E_1 - E_2 - I$ both $< I$, and hence $I \leq E_1 < 3I$. If $E_1 \geq 3I$, then one at least of electrons 2 and 3 will have an energy $\geq I$, and will therefore ionize further. If $I \leq E_1 < 2I$, then $E_2 + E_3 < I$, and therefore both E_1 and E_2 are $< I$, and will not ionize; hence, we get from this range the contribution

$$\int_I^{2I} \frac{IdE_1}{(E_1 + I)^2} = \frac{1}{6}.$$

If $2I \leq E_1 < 3I$, then the requirement that $E_2 < I$ and $E_1 - E_2 - I < I$ means that the range of E_2 must be limited to $E - 2I < E_2 < I$. The last two integrals in the right-hand side of (A2) yield in this range

$$\int_0^\infty \exp[-\lambda(E_1)\tau] d\tau \int_{E_1 - 2I}^I \frac{\pi\epsilon^4 N}{E_1} \frac{dE_2}{(E_2 + I)^2} = \frac{E_1(3I - E_1)}{2(E_1 - I)^2};$$

integrating with respect to E_1 , we obtain the contribution

$$\int_{2I}^{3I} \frac{E_1(3I - E_1)}{2(E_1 - I)^2} \cdot \frac{IdE_1}{(E_1 + I)^2} = \frac{1}{12} - \frac{1}{8} \log \frac{3}{2}.$$

Adding these two contributions, we finally obtain

$$q_2 = \frac{1}{4} - \frac{1}{8} \log \frac{3}{2} = 0.199. \quad (A3)$$

Note added in proof.—Contrary to the conclusions stated above, it now appears from a critical analysis by Dr. E. P. George of the available experimental data that agreement with the theory is substantially improved, at least for gases, by the results of § 6 (owing to the broadening of the scale for the reduced distribution by a factor $\pi/2$: cf. eqn. (6.6)); this was also pointed out to me in a letter by Dr. B. T. Price. It now seems possible that, with the introduction of a more exact cross section, the theory should account for all the facts.

Dr. U. Fano has pointed out that the approximate distribution (4.6) does not agree with Landau's numerical evaluation for large ω owing to the breakdown of the saddle-point method in this range. This is not very important as regards comparison with experiment, because the frequency of events with energy loss greater than twice the probable value is small (of the order of 5%).

XXXI. *Atmospheric Scattering and Absorption of Ultra-violet Sunlight*

By G. F. WALTON

University of St. Andrews ; Queen's College, Dundee*

[Received November 10, 1954]

ABSTRACT

The scattering of a parallel beam of unpolarized sunlight in a plane-stratified atmosphere is considered, taking into account the polarization of scattered light and allowing for the optical anisotropy of the molecules of air. Allowance is also made for the attenuation of the ultra-violet light due to absorption by atmospheric ozone. Expressions are derived for the intensities of the primary, secondary, and tertiary scattered light emitted and received in any direction and at any point in the atmosphere.

§ 1. INTRODUCTION

IN this paper we consider part of the problem of the ultra-violet 'illumination' of the earth's atmosphere and surface by scattered sunlight. Of special interest is the ultra-violet radiation which is received at the earth's surface from various directions and for various positions of the sun in the sky.

We confine our attention to wavelengths for which the absorption coefficients of ozone may be assumed to be independent of atmospheric pressure and temperature. The problem is also restricted to a plane-stratified atmosphere, assumed to rest on a flat surface. Reflection at the ground and refraction are neglected, as also are the scattering effects of dust and haze. It is assumed that energy is not transformed from one wavelength to another by absorption and re-emission.

A similar restricted problem, but referring to the scattering of visible light in an ozone-free atmosphere, has been treated by Hammad (1948) and Chandrasekhar (1948) on different bases, but both take account of the polarization of the scattered light. Hammad modified an earlier step-by-step treatment (Hammad and Chapman 1939), considering only primary and secondary scattering, but his adopted law of scattering allowed for the anisotropy of the scattering molecules.

By Chandrasekhar's method, an equation of transfer is formulated. The solution of the associated integral equations yields an expression for the intensity of the scattered light, which includes contributions from all orders of scattering. Difficulties arise in this method when allowance is made for the anisotropy of the molecules (Chandrasekhar 1950 d).

* Communicated by the Author.

Since such allowance is desirable (Hammad 1953), and since a comparison of the contributions due to various orders of scattering is of interest in work on the vertical distribution of ozone (Chapman 1935, Dobson 1951), we here proceed in steps. However, we incorporate Chandrasekhar's treatment of polarization, which facilitates the derivation of the secondary and tertiary expressions.

§ 2. NOTATION

Let M_0 and M signify the total mass of ozone and air respectively contained in a vertical column of unit cross-sectional area extending throughout the atmosphere; m_0 and m the fraction of ozone and air respectively contained in this column above a height h . Then

$$M_0 m_0 = \int_h^\infty \rho_0(h) dh \text{ and } M m = \int_h^\infty \rho(h) dh, \quad \dots \quad (2.1)$$

where $\rho_0(h)$ and $\rho(h)$ denote the density of ozone and air respectively at the height h . At the top of the atmosphere $m_0 = m = 0$; at the bottom $m_0 = m = 1$. The variable m will be called the level, and the vertical distribution of ozone may be regarded as characterized by a function $m_0(m)$.

The mass absorption coefficient of ozone and the mass scattering coefficient of air, for light of wavelength λ , will be denoted by $\alpha(\lambda)$ and $\sigma(\lambda)$ respectively, or, briefly by α and σ . We also write

$$a = \alpha M_0 \text{ and } s = \sigma M. \quad \dots \quad (2.2)$$

Consider any point O in the atmosphere and construct rectangular Cartesian axes OX , OY , and OZ such that the positive direction of the Z -axis is vertically downwards, and such that the sun (regarded as a point) lies in the negative quadrant of the plane YOZ . Any direction may be specified by the polar angles (θ, ϕ) relative to OZ and the plane YOZ . We let $d\omega$, $d\omega'$, and $d\omega_0$ respectively denote small solid angles about this direction, any other direction (θ', ϕ') , and the direction $(\theta_0, 0)$ of the solar beam, θ_0 signifying the zenith distance of the sun. We shall also write

$$\mu = \cos \theta, \mu' = \cos \theta', \text{ and } \mu_0 = \cos \theta_0.$$

The intensity of monochromatic light which is received at height h and is travelling in the direction (θ, ϕ) , when the solar zenith distance is θ_0 , will be denoted by $R(h, \theta, \phi, \theta_0)$. The letters d and u will follow the symbol R when we wish to distinguish between light travelling downwards and upwards respectively. We let $E(h, \theta, \phi, \theta_0)$ signify the rate of emission of monochromatic light-energy per unit mass of air at height h , per unit solid angle about the direction (θ, ϕ) , when the solar zenith distance is θ_0 . The parts of these functions referring to direct sunlight, primary, secondary, and tertiary scattered light will be distinguished by the addition of the suffixes 0, 1, 2, and 3 respectively. The variables h, θ , and θ_0 specified in these functions will often be replaced by the corresponding variables m, μ , and μ_0 .

§ 3. A REPRESENTATION OF PARTIALLY PLANE-POLARIZED LIGHT

It may be shown (Chandrasekhar 1946) that the intensity of partially plane-polarized light (which is the most general type of light we consider in this problem) may be represented by three parameters, equivalent to three of the parameters introduced by Stokes (1852). For instance, if R_* and R_l denote the components of the light-intensity in the direction l and in the direction r at right angles to it, the intensity $R(\psi)$ resolved in a direction inclined at an angle ψ to the direction of l is given by

$$R(\psi) = R_l \cos^2 \psi + R_r \sin^2 \psi + R_u \cos \psi \sin \psi, \quad (3.1)$$

where R_u denotes the third Stokes parameter. In the particular case of unpolarized (natural) light, $R(\psi)$ must be independent of ψ , whence

$$R_l = R_r = \frac{1}{2}R, \text{ and } R_u = 0, \quad (3.2)$$

where R denotes the total intensity.

In the following work the intensity of received light is represented by a vector \mathbf{R} , or $\{R_l, R_r, R_u\}$, the symbol R being reserved for the total intensity ($R_l + R_r$). Similarly, the rate of emission of energy, per unit mass of air per unit solid angle, is represented by a vector \mathbf{E} , or $\{E_l, E_r, E_u\}$, and E denotes ($E_l + E_r$).

§ 4. THE ATTENUATION OF DIRECT SUNLIGHT

The intensity of the light received at any height and in any direction will depend on the amount of attenuation, due to absorption by molecules of ozone and scattering by molecules of air, which the light has undergone. This dependence may be expressed by the relation

$$\mathbf{R}(h, \theta, \phi, \theta_0) = \mathbf{R}(h', \theta, \phi, \theta_0) \exp \left[- \int_h^{h'} (\alpha \rho_0 + \sigma \rho) \sec \theta \, dh \right]. \quad (4.1)$$

In the case of direct sunlight, which we assume is unpolarized, the relations (3.2) are satisfied. By (3.2) and (4.1) we have

$$\mathbf{R}d_0(h, \theta_0, 0, \theta_0) d\omega_0 = \begin{bmatrix} \frac{1}{2} \\ \frac{1}{2} \\ 0 \end{bmatrix} I_\infty \exp \left[- \int_h^\infty (\alpha \rho_0 + \sigma \rho) \sec \theta \, dh \right], \quad (4.2)$$

where $\mathbf{R}d_0(h, \theta_0, 0, \theta_0)$ represents the intensity of direct sunlight received at height h and travelling downwards in the directions confined to the solid angle about the direction $(\theta_0, 0)$; and I_∞ briefly denotes $\mathbf{R}d_0(\infty, \theta_0, 0, \theta_0)$ and is the total solar monochromatic energy received outside the atmosphere on a unit area placed normal to this direction per unit time. From (2.1), (2.2), and (4.2) we get

$$\mathbf{R}d_0(m, \mu_0, 0, \mu_0) = \begin{bmatrix} \frac{1}{2} \\ \frac{1}{2} \\ 0 \end{bmatrix} I_\infty \exp [-(am_0 + sm)/\mu], \quad (4.3)$$

where $\mathbf{R}d_0(m, \mu_0, 0, \mu_0)$ replaces $\mathbf{R}d_0(h, \theta_0, 0, \theta_0)$ (see § 2). Also

$$\mathbf{R}d_0(m, \mu, \theta, \mu_0) = 0 \text{ when } \mu \neq \mu_0, \text{ and } \mathbf{R}u_0(m, \mu, \phi, \mu_0) \equiv 0. \quad (4.4)$$

§ 5. THE LAW OF SCATTERING BY ANISOTROPIC MOLECULES

The Rayleigh law of scattering, generalized to include the case of scattering of arbitrarily polarized light characterized by a set of Stokes parameters (Chandrasekhar 1950 a) may be expressed as follows :

$$\mathbf{E}(m, \mu, \phi, \mu_0) = (\sigma/4\pi) \mathbf{P}(\mu, \phi, \mu', \phi') \mathbf{R}(m, \mu', \phi', \mu_0) d\omega'. \quad (5.1)$$

Here $\mathbf{R}(m, \mu', \phi', \mu_0)$ represents the intensity of the light received at level m and travelling in the directions confined to the solid angle $d\omega'$ about the direction $(\cos^{-1} \mu', \phi')$; $\mathbf{E}(m, \mu, \phi, \mu_0)$ represents the rate of emission of scattered energy, at the same point per unit mass, per unit solid angle about the direction $(\cos^{-1} \mu, \phi)$; and $\mathbf{P}(\mu, \phi, \mu', \phi')$ denotes the phase-matrix for Rayleigh scattering.

The explicit form of $\mathbf{P}(\mu, \phi, \mu', \phi')$ has been derived by Chandrasekhar (1950 b), who has also shown (1950 c) that when the anisotropy of the scattering molecules is included, $\mathbf{P}(\mu, \phi, \mu', \phi')$ in the case of partially plane-polarized light should be replaced by

$$\left(\frac{1-\gamma}{1+2\gamma} \right) \mathbf{P}(\mu, \phi, \mu', \phi') + \frac{3\gamma}{2(1+2\gamma)} \begin{bmatrix} 1 & 1 & 0 \\ 1 & 1 & 0 \\ 0 & 0 & 0 \end{bmatrix}, \quad (5.2)$$

where $\gamma = \delta/(2-\delta)$, and δ is the depolarization factor.

In the present work it is convenient to denote (5.2) by

$$3\mathbf{Q}(\mu, \phi, \mu', \phi')/(2+\delta).$$

The law of scattering by anisotropic molecules then assumes the following form :

$$\mathbf{E}(m, \mu, \phi, \mu_0) = \frac{3\sigma}{8\pi(1+\frac{1}{2}\delta)} \mathbf{Q}(\mu, \phi, \mu', \phi') \mathbf{R}(m, \mu', \phi', \mu_0) d\omega'. \quad (5.3)$$

The explicit form of $\mathbf{Q}(\mu, \phi, \mu', \phi')$ may be written as follows :

$$\mathbf{Q}(\mu, \phi, \mu', \phi') = \mathbf{Q}^{(0)}(\mu, \mu') + (1-\delta)(1-\mu^2)^{1/2}(1-\mu'^2)^{1/2} \mathbf{Q}^{(1)}(\mu, \phi, \mu', \phi') \\ + (1-\delta) \mathbf{Q}^{(2)}(\mu, \phi, \mu', \phi'), \quad (5.4)$$

where

$$\mathbf{Q}^{(0)}(\mu, \mu') = (1-\delta) \begin{bmatrix} (1-\mu^2-\mu'^2+\frac{3}{2}\mu^2\mu'^2) & \frac{1}{2}\mu^2 & 0 \\ \frac{1}{2}\mu'^2 & \frac{1}{2} & 0 \\ 0 & 0 & 0 \end{bmatrix} + \frac{1}{2}\delta \begin{bmatrix} 1 & 1 & 0 \\ 1 & 1 & 0 \\ 0 & 0 & 0 \end{bmatrix},$$

$$\mathbf{Q}^{(1)}(\mu, \phi, \mu', \phi') = \begin{bmatrix} 2\mu\mu' \cos(\phi' - \phi) & 0 & \mu \sin(\phi' - \phi) \\ 0 & 0 & 0 \\ -2\mu' \sin(\phi' - \phi) & 0 & \cos(\phi' - \phi) \end{bmatrix},$$

and $\mathbf{Q}^{(2)}(\mu, \phi, \mu', \phi')$

$$= \begin{bmatrix} \frac{1}{2}\mu^2\mu'^2 \cos 2(\phi' - \phi) & -\frac{1}{2}\mu^2 \cos 2(\phi' - \phi) & \frac{1}{2}\mu^2\mu' \sin 2(\phi' - \phi) \\ -\frac{1}{2}\mu'^2 \cos 2(\phi' - \phi) & \frac{1}{2} \cos 2(\phi' - \phi) & -\frac{1}{2}\mu' \sin 2(\phi' - \phi) \\ -\mu\mu'^2 \sin 2(\phi' - \phi) & \mu \sin 2(\phi' - \phi) & \mu\mu' \cos 2(\phi' - \phi) \end{bmatrix} \quad (5.5)$$

§ 6. THE EMISSION AND RECEPTION OF PRIMARY SCATTERED LIGHT

The rate of emission of primary scattered light, per unit mass of air at level m , per unit solid angle about the direction $(\cos^{-1}\mu, \phi)$ will be represented by $\mathbf{E}_1(m, \mu, \phi, \mu_0)$. It follows from (5.3) that

$$\mathbf{E}_1(m, \mu, \phi, \mu_0) = \frac{3\sigma}{8\pi(1+\frac{1}{2}\delta)} \mathbf{Q}(\mu, \phi, \mu_0, 0) \mathbf{R}_0(m, \mu_0, 0, \mu_0) d\omega_0. \quad (6.1)$$

Substituting for $\mathbf{R}_0(m, \mu_0, 0, \mu_0)$ from (4.3) and (4.4), we have

$$\mathbf{E}_1(m, \mu, \phi, \mu_0) = \frac{3\sigma I_\infty}{16\pi(1+\frac{1}{2}\delta)} \mathbf{A}(\mu, \phi, \mu_0) K(m, \mu_0), \quad (6.2)$$

where

$$\mathbf{A}(\mu, \phi, \mu_0) = \mathbf{Q}(\mu, \phi, \mu_0, 0) \begin{bmatrix} 1 \\ 1 \\ 0 \end{bmatrix}, \quad (6.3)$$

and*

$$K(m, \mu) = \exp[-(am_0 + sm)/\mu_0]. \quad (6.4)$$

Putting $\phi' = 0$ and substituting μ_0 for μ' in (5.4), and carrying out the matrix-multiplication in (6.3), we get

$$\mathbf{A}(\mu, \phi, \mu_0) = \mathbf{A}^{(0)}(\mu, \mu_0) + 2(1-\delta)(1-\mu^2)^{1/2}(1-\mu_0^2)^{1/2}\mu_0 \mathbf{A}^{(1)}(\mu, \phi) + \frac{1}{2}(1-\delta)(1-\mu_0^2)\mathbf{A}^{(2)}(\mu, \phi), \quad (6.5)$$

where

$$\mathbf{A}^{(0)}(\mu, \mu_0) = \frac{1}{2}(1-\delta) \begin{bmatrix} 2-\mu^2-2\mu_0^2+3\mu^2\mu_0^2 \\ 1+\mu_0^2 \\ 0 \end{bmatrix} + \delta \begin{bmatrix} 1 \\ 1 \\ 0 \end{bmatrix},$$

$$\mathbf{A}^{(1)}(\mu, \phi) = \begin{bmatrix} \mu \cos \phi \\ 0 \\ \sin \phi \end{bmatrix}, \text{ and } \mathbf{A}^{(2)}(\mu, \phi) = \begin{bmatrix} -\mu^2 \cos 2\phi \\ + \cos 2\phi \\ -\mu \sin 2\phi \end{bmatrix}. \quad (6.6)$$

From (6.2) we derive the following expression, which refers to the total intensity (see § 3) :

$$E_1(m, \mu, \phi, \mu_0) = \frac{3\sigma I_\infty}{16\pi(1+\frac{1}{2}\delta)} A(\mu, \phi, \mu_0) K(m, \mu_0), \quad (6.7)$$

where, by adding the first and second rows of $\mathbf{A}(\mu, \phi, \mu_0)$, we find that

$$A(\mu, \phi, \mu_0) = \frac{1}{2}(1-\delta)[3-\mu^2-\mu_0^2+3\mu^2\mu_0^2+4\mu\mu_0(1-\mu^2)^{1/2}(1-\mu_0^2)^{1/2}\cos\phi + (1-\mu^2)(1-\mu_0^2)\cos 2\phi] + 2\delta. \quad (6.8)$$

The reception of primary scattered light is treated by the method of Hammad and Chapman (1939), allowance being now made for the absorption by ozone. Corresponding to eqn. (1) of § 12 of the paper cited† we have, in our notation,

$$\mathbf{R}_1(m, \mu, \phi, \mu_0) = \frac{M}{\mu} \int \mathbf{E}_1(m', \mu, \phi, \mu_0) \exp[-(am_0 + sm - am_0' - sm')/\mu] dm', \quad (6.9)$$

* For the sake of brevity, the variables a , s , and m_0 will not be specified in the function K , nor in several functions which are introduced later.

† The author's usage of m differs from that of Hammad and Chapman, who denoted this quantity by \bar{m} .

where m_0' denotes the value of m_0 at level m' , and the limits of integration depend on whether the light is travelling downwards or upwards. We find that, for light travelling downwards ($0 < \mu \leq 1$)

$$\mathbf{R}d_1(m, \mu, \phi, \mu_0) = \frac{M}{\mu} \int_0^m \mathbf{E}_1(m', \mu, \phi, \mu_0) \exp[-(am_0 + sm - am_0' - sm')/\mu] dm', \quad (6.10)$$

and, for light travelling upwards ($-1 \leq \mu < 0$),

$$\mathbf{R}u_1(m, \mu, \phi, \mu_0) = -\frac{M}{\mu} \int_m^1 \mathbf{E}_1(m', \mu, \phi, \mu_0) \exp[-(am_0 + sm - am_0' - sm')/\mu] dm'. \quad (6.11)$$

Substituting for $\mathbf{E}_1(m', \mu, \phi, \mu_0)$ in accordance with (6.2), we have

$$\mathbf{R}d_1(m, \mu, \phi, \mu_0) = \frac{3s I_\infty}{16\pi(1 + \frac{1}{2}\delta)\mu} \mathbf{A}(\mu, \phi, \mu_0) Kd(m, \mu, \mu_0), \quad (6.12)$$

and

$$\mathbf{R}u_1(m, \mu, \phi, \mu_0) = \frac{-3s I_\infty}{16\pi(1 + \frac{1}{2}\delta)\mu} \mathbf{A}(\mu, \phi, \mu_0) Ku(m, \mu, \mu_0), \quad (6.13)$$

$$\text{where} \quad Kd(m, \mu, \mu_0) = K(m, \mu) \int_0^m K(m', -\mu) K(m', \mu_0) dm', \quad (6.14)$$

$$\text{and} \quad Ku(m, \mu, \mu_0) = K(m, \mu) \int_m^1 K(m', -\mu) K(m', \mu_0) dm'. \quad (6.15)$$

Expressions for the total intensities $\mathbf{R}d_1$ and $\mathbf{R}u_1$ may be derived from (6.12) and (6.13). These expressions contain (6.8), and will not be given here.

§ 7. THE EMISSION AND RECEPTION OF SECONDARY SCATTERED LIGHT

The rate of emission of secondary scattered light, per unit mass, at level m , per unit solid angle about the direction $(\cos^{-1}\mu, \phi)$ will be represented by $\mathbf{E}_2(m, \mu, \phi, \mu_0)$. It follows from (5.3) that the contribution to \mathbf{E}_2 from primary scattered light received in the solid angle $d\omega'$ about the direction $(\cos^{-1}\mu', \phi')$ is

$$\frac{3\sigma}{8\pi(1 + \frac{1}{2}\delta)} \mathbf{Q}(\mu, \phi, \mu', \phi') \mathbf{R}d_1(m, \mu', \phi', \mu_0) d\omega', \text{ when } 0 < \mu' \leq 1, \quad (7.1)$$

$$\text{and } \frac{3\sigma}{8\pi(1 + \frac{1}{2}\delta)} \mathbf{Q}(\mu, \phi, \mu', \phi') \mathbf{R}u_1(m, \mu', \phi', \mu_0) d\omega', \text{ when } -1 \leq \mu' < 0. \quad (7.2)$$

Forming the sum of the contributions from all directions, and replacing μ' in (7.2) by $-\mu'$, we get

$$\begin{aligned} \mathbf{E}_2(m, \mu, \phi, \mu_0) = & \frac{3\sigma}{8\pi(1 + \frac{1}{2}\delta)} \int_0^{2\pi} \int_0^1 \{ \mathbf{Q}(\mu, \phi, \mu', \phi') \mathbf{R}d_1(m, \mu', \phi', \mu_0) \\ & + \mathbf{Q}(\mu, \phi, -\mu', \phi') \mathbf{R}u_1(m, -\mu', \phi', \mu_0) \} d\phi' d\mu'. \quad (7.3) \end{aligned}$$

Substituting for $\mathbf{R}d_1(m, \mu', \phi', \mu_0)$ and $\mathbf{R}u_1(m, -\mu', \phi', \mu_0)$ in accordance with (6.12) and (6.13) gives

$$\mathbf{E}_2(m, \mu, \phi, \mu_0) = \frac{9\sigma s I_\infty}{128\pi^2(1+\frac{1}{2}\delta)^2} \int_0^{2\pi} \int_0^1 \{ \mathbf{Q}(\mu, \phi, \mu', \phi') \mathbf{A}(\mu', \phi', \mu_0) Kd(m, \mu', \mu_0) \\ + \mathbf{Q}(\mu, \phi, -\mu', \phi') \mathbf{A}(-\mu', \phi', \mu_0) Ku(m, -\mu', \mu_0) \} d\phi' d\mu' / \mu'. \quad (7.4)$$

Our next step is to carry out the integration with respect to ϕ' . To facilitate this step, we express $\mathbf{Q}(\mu, \phi, \mu', \phi')$ and $\mathbf{A}(\mu', \phi', \mu_0)$ in the forms (5.4) and (6.5) respectively, and we note the values of the following integrals, in which p and q are integers :

$$\int_0^{2\pi} \cos p(\phi' - \phi) \cdot \cos q\phi' \cdot d\phi' = \begin{cases} 0 & \text{if } p \neq q \\ \pi \cos p\phi & \text{if } p = q \neq 0 \\ 2\pi & \text{if } p = q = 0, \end{cases}$$

$$\int_0^{2\pi} \cos p(\phi' - \phi) \cdot \sin q\phi' \cdot d\phi' = \begin{cases} 0 & \text{if } p \neq q \\ \pi \sin p\phi & \text{if } p = q, \end{cases}$$

$$\int_0^{2\pi} \sin p(\phi' - \phi) \cdot \cos q\phi' \cdot d\phi' = \begin{cases} 0 & \text{if } p \neq q \\ -\pi \sin p\phi & \text{if } p = q, \end{cases}$$

$$\int_0^{2\pi} \sin p(\phi' - \phi) \cdot \sin q\phi' \cdot d\phi' = \begin{cases} 0 & \text{if } p \neq q \\ \pi \cos p\phi & \text{if } p = q \neq 0. \end{cases} \quad (7.5)$$

We find that non-zero contributions only arise from the integration of the direct products $\mathbf{Q}^{(0)} \mathbf{A}^{(0)}$, $\mathbf{Q}^{(1)} \mathbf{A}^{(1)}$, and $\mathbf{Q}^{(2)} \mathbf{A}^{(2)}$. After some reduction we get

$$\frac{1}{\pi} \int_0^{2\pi} \mathbf{Q}(\mu, \phi, \mu', \phi') \mathbf{A}(\mu', \phi', \mu_0) d\phi' = \sum_{i=1}^3 \mathbf{B}_i(\mu, \phi, \mu_0) \mu'^{(2i-2)}. \quad (7.6)$$

Neglecting terms in δ^2 , we find that $\mathbf{B}_i(\mu, \phi, \mu_0)$ may be expressed as follows:

$$\mathbf{B}_i(\mu, \phi, \mu_0) = \mathbf{B}_i^{(0)}(\mu, \mu_0) + 2(1-2\delta)(1-\mu^2)^{1/2}(1-\mu_0^2)^{1/2}\mu_0 \mathbf{B}_i^{(1)}(\mu, \phi) \\ + \frac{1}{4}(1-2\delta)(1-\mu_0^2) \mathbf{B}_i^{(2)}(\mu, \phi), (i=1, 2, 3), \quad (7.7)$$

where

$$\mathbf{B}_1^{(0)}(\mu, \mu_0) = \frac{1}{2}(1-2\delta) \begin{bmatrix} 4-3\mu^2-4\mu_0^2+5\mu^2\mu_0^2 \\ 1+\mu_0^2 \\ 0 \end{bmatrix} + \frac{1}{2}\delta \begin{bmatrix} 7-2\mu^2-\mu_0^2 \\ 5-\mu_0^2 \\ 0 \end{bmatrix},$$

$$\mathbf{B}_2^{(0)}(\mu, \mu_0) = (1-2\delta) \begin{bmatrix} -3+4\mu^2+5\mu_0^2-6\mu^2\mu_0^2 \\ 1-\mu_0^2 \\ 0 \end{bmatrix} + \frac{1}{2}\delta \begin{bmatrix} -5+6\mu^2+3\mu_0^2 \\ 1+3\mu_0^2 \\ 0 \end{bmatrix},$$

$$\mathbf{B}_3^{(0)}(\mu, \mu_0) = \frac{1}{2}(1-2\delta)(1-3\mu_0^2) \begin{bmatrix} 2-3\mu^2 \\ -1 \\ 0 \end{bmatrix},$$

$$\mathbf{B}_1^{(1)}(\mu, \phi) = \mathbf{B}_2^{(1)}(\mu, \phi) = -\frac{1}{2}\mathbf{B}_3^{(1)}(\mu, \phi) = \mathbf{A}^{(1)}(\mu, \phi),$$

and

$$\mathbf{B}_1^{(2)}(\mu, \phi) = \frac{1}{2}\mathbf{B}_2^{(2)}(\mu, \phi) = \mathbf{B}_3^{(2)}(\mu, \phi) = \mathbf{A}^{(2)}(\mu, \phi); \quad [\text{see (6.6)}]. \quad (7.8)$$

Changing the sign of μ' in (7.6), we also have

$$\frac{1}{\pi} \int_0^{2\pi} \mathbf{Q}(\mu, \phi, -\mu', \phi') \mathbf{A}(-\mu', \phi', \mu_0) d\phi' = \sum_{i=1}^3 \mathbf{B}_i(\mu, \phi, \mu_0) \mu'^{(2i-2)}. \quad (7.9)$$

From (7.4), (7.6) and (7.9) we then have

$$\mathbf{E}_2(m, \mu, \phi, \mu_0) = \frac{9\sigma s I_\infty}{128\pi(1+\frac{1}{2}\delta)^2} \sum_{i=1}^3 \{\mathbf{B}_i(\mu, \phi, \mu_0) L_{2i-1}(m, \mu_0)\}, \quad (7.10)$$

where

$$L_{2i-1}(m, \mu_0) = \int_0^1 [Kd(m, \mu', \mu_0) + Ku(m, -\mu', \mu_0)] \mu'^{(2i-3)} d\mu', \quad (7.11)$$

the functions Kd and Ku being given by (6.14) and (6.15) respectively.

The following expression, referring to the total intensity (see § 3), may be derived from (7.10) :

$$E_2(m, \mu, \phi, \mu_0) = \frac{9\sigma s I_\infty}{128\pi(1+\frac{1}{2}\delta)^2} \sum_{i=1}^3 B_i L_{2i-1}(m, \mu_0), \quad (7.12)$$

where B_i briefly denotes $B_i(\mu, \phi, \mu_0)$. We find that

$$B_1 = \frac{1}{2}(1-2\delta)[5-3\mu^2-3\mu_0^2+5\mu^2\mu_0^2+4\mu\mu_0(1-\mu^2)^{1/2}(1-\mu_0^2)^{1/2}\cos\phi \\ + \frac{1}{2}(1-\mu^2)(1-\mu_0^2)\cos 2\phi] + \delta(6-\mu^2-\mu_0^2),$$

$$B_2 = (1-2\delta)[-2+4\mu^2+4\mu_0^2-6\mu^2\mu_0^2+2\mu\mu_0(1-\mu^2)^{1/2}(1-\mu_0^2)^{1/2}\cos\phi \\ + \frac{1}{2}(1-\mu^2)(1-\mu_0^2)\cos 2\phi] + \delta(-2+3\mu^2+3\mu_0^2),$$

and

$$B_3 = \frac{1}{2}(1-2\delta)[(1-3\mu^2)(1-3\mu_0^2)-8\mu\mu_0(1-\mu^2)^{1/2}(1-\mu_0^2)^{1/2}\cos\phi \\ + \frac{1}{2}(1-\mu^2)(1-\mu_0^2)\cos 2\phi]. \quad (7.13)^*$$

The treatment of the reception of secondary scattered light follows that outlined in § 6 for the reception of primary scattered light. Thus we have

$$\mathbf{R}d_2(m, \mu, \phi, \mu_0) = \frac{9s^2 I_\infty}{128\pi(1+\frac{1}{2}\delta)^2\mu} \sum_{i=1}^3 \{\mathbf{B}_i(\mu, \phi, \mu_0) Ld_{2i-1}(m, \mu, \mu_0)\}, \quad (7.14)$$

and

$$\mathbf{R}u_2(m, \mu, \phi, \mu_0) = - \frac{9s^2 I_\infty}{128\pi(1+\frac{1}{2}\delta)^2\mu} \sum_{i=1}^3 \{\mathbf{B}_i(\mu, \phi, \mu_0) Lu_{2i-1}(m, \mu, \mu_0)\}, \quad (7.15)$$

where

$$Ld_{2i-1}(m, \mu, \mu_0) = K(m, \mu) \int_0^m K(m', -\mu) L_{2i-1}(m', \mu_0) dm', \quad (7.16)$$

and

$$Lu_{2i-1}(m, \mu, \mu_0) = K(m, \mu) \int_m^1 K(m', -\mu) L_{2i-1}(m', \mu_0) dm'. \quad (7.17)$$

*The author has verified that the corresponding expressions of Hammad (1948), which refer to the directions normal and parallel to the plane of scattering, combine to give (7.13), apart from two discrepancies, which have been traced to small errors in Hammad's expressions for B_4 and C_4 .

§ 8. THE EMISSION AND RECEPTION OF TERTIARY SCATTERED LIGHT

The treatment of tertiary scattering follows that outlined in the preceding sections, the number of the azimuthal expressions and the structure of the multiple integrals being greater in this case. Corresponding to (7.3), we have

$$\mathbf{E}_3(m, \mu, \phi, \mu_0) = \frac{3\sigma}{8\pi(1+\frac{1}{2}\delta)} \int_0^{2\pi} \int_0^1 \{ \mathbf{Q}(\mu, \phi, \mu', \phi') \mathbf{R}d_2(m, \mu', \phi', \mu_0) \\ + \mathbf{Q}(\mu, \phi, -\mu', \phi') \mathbf{R}u_2(m, -\mu', \phi', \mu_0) \} d\mu' d\phi'. \quad (8.1)$$

Substituting for $\mathbf{R}d_2(m, \mu', \phi', \mu_0)$ and $\mathbf{R}u_2(m, -\mu', \phi', \mu_0)$ in accordance with (7.14) and (7.15) we get

$$E_3(m, \mu, \phi, \mu_0) = \frac{27\sigma s^2 I_\infty}{1024\pi^2(1+\frac{1}{2}\delta)^3} \sum_{i=1}^3 \int_0^{2\pi} \int_0^1 [\mathbf{Q}(\mu, \phi, \mu', \phi') \mathbf{B}_i(\mu', \phi', \mu_0) \\ \times Ld_{2i-1}(m, \mu', \mu_0) + \mathbf{Q}(\mu, \phi, -\mu', \phi') \mathbf{B}_i(-\mu', \phi', \mu_0) Lu_{2i-1}(m, -\mu', \mu_0)] \\ d\phi' d\mu' / \mu'. \quad (8.2)$$

We effect the integration with respect to ϕ' by the method of § 7, making use of the results (7.5). In this case we write

$$\frac{1}{\pi} \int_0^{2\pi} \mathbf{Q}(\mu, \phi, \mu', \phi') \mathbf{B}_i(\mu', \phi', \mu_0) d\phi' = \sum_{j=1}^3 \mathbf{C}_{ij}(\mu, \phi, \mu_0) \mu'^{(2j-2)}, \quad (i=1, 2, 3), \quad (8.3)$$

the same result being obtained when the sign of μ' is changed. Neglecting terms in δ^2 , we find that $\mathbf{C}_{ij}(\mu, \phi, \mu_0)$ may be expressed as follows :

$$\mathbf{C}_{ij}(\mu, \phi, \mu_0) = \mathbf{C}_{ij}^{(0)}(\mu, \mu_0) + 2(1-3\delta)(1-\mu^2)^{1/2}(1-\mu_0^2)^{1/2} \mu_0 \mathbf{C}_{ij}^{(1)}(\mu, \phi) \\ + \frac{1}{8}(1-3\delta)(1-\mu_0^2) \mathbf{C}_{ij}^{(2)}(\mu, \phi), \quad (i=1, 2, 3; j=1, 2, 3), \quad (8.4)$$

where

$$\mathbf{C}_{11}^{(0)}(\mu, \mu_0) = \frac{1}{2}(1-3\delta) \begin{bmatrix} 8-7\mu^2-8\mu_0^2+9\mu^2\mu_0^2 \\ 1+\mu_0^2 \\ 0 \end{bmatrix} + \frac{1}{2}\delta \begin{bmatrix} 19-9\mu^2-5\mu_0^2+\mu^2\mu_0^2 \\ 10-4\mu_0^2 \\ 0 \end{bmatrix},$$

$$\mathbf{C}_{12}^{(0)}(\mu, \mu_0) = (1-3\delta) \begin{bmatrix} -7+9\mu^2+9\mu_0^2-11\mu^2\mu_0^2 \\ 2-2\mu_0^2 \\ 0 \end{bmatrix} + \frac{1}{2}\delta \begin{bmatrix} -21+25\mu^2+7\mu_0^2-3\mu^2\mu_0^2 \\ 4+4\mu_0^2 \\ 0 \end{bmatrix},$$

$$\mathbf{C}_{13}^{(0)}(\mu, \mu_0) = \frac{1}{2}(1-3\delta) \begin{bmatrix} 6-9\mu^2-10\mu_0^2+15\mu^2\mu_0^2 \\ -3+5\mu_0^2 \\ 0 \end{bmatrix} + \delta \begin{bmatrix} 2-3\mu^2 \\ -1 \\ 0 \end{bmatrix},$$

$$\mathbf{C}_{21}^{(0)}(\mu, \mu_0) = (1-3\delta) \begin{bmatrix} -6+7\mu^2+10\mu_0^2-11\mu^2\mu_0^2 \\ 1-\mu_0^2 \\ 0 \end{bmatrix} \\ + \frac{1}{2}\delta \begin{bmatrix} -14+11\mu^2+14\mu_0^2-3\mu^2\mu_0^2 \\ -3+11\mu_0^2 \\ 0 \end{bmatrix},$$

$$\mathbf{C}_{22}^{(0)}(\mu, \mu_0) = (1 - 3\delta) \begin{bmatrix} 14 - 17\mu^2 - 22\mu_0^2 + 27\mu^2\mu_0^2 \\ -3 + 5\mu_0^2 \\ 0 \end{bmatrix} + \frac{1}{2}\delta \begin{bmatrix} 30 - 27\mu^2 - 18\mu_0^2 + 9\mu^2\mu_0^2 \\ 3 - 9\mu_0^2 \\ 0 \end{bmatrix},$$

$$\mathbf{C}_{23}^{(0)}(\mu, \mu_0) = (1 - 3\delta) \begin{bmatrix} -8 + 12\mu^2 + 12\mu_0^2 - 18\mu^2\mu_0^2 \\ 4 - 6\mu_0^2 \\ 0 \end{bmatrix} + \delta \begin{bmatrix} -6 + 9\mu^2 \\ 3 \\ 0 \end{bmatrix},$$

$$\mathbf{C}_{31}^{(0)}(\mu, \mu_0) = \frac{1}{2}(1 - 3\delta)(1 - 3\mu_0^2) \begin{bmatrix} 4 - 5\mu^2 \\ -1 \\ 0 \end{bmatrix} + \frac{1}{2}\delta(1 - 3\mu_0^2) \begin{bmatrix} 1 \\ 1 \\ 0 \end{bmatrix},$$

$$\mathbf{C}_{32}^{(0)}(\mu, \mu_0) = (1 - 3\delta)(1 - 3\mu_0^2) \begin{bmatrix} -5 + 6\mu^2 \\ 1 \\ 0 \end{bmatrix} + \frac{1}{2}\delta(1 - 3\mu_0^2) \begin{bmatrix} -3 \\ -3 \\ 0 \end{bmatrix},$$

$$\mathbf{C}_{33}^{(0)}(\mu, \mu_0) = \frac{1}{2}(1 - 3\delta)(1 - 3\mu_0^2) \begin{bmatrix} 6 - 9\mu^2 \\ -3 \\ 0 \end{bmatrix},$$

$$\begin{aligned} \mathbf{C}_{11}^{(1)}(\mu, \phi) = \mathbf{C}_{12}^{(1)} = -\frac{1}{2}\mathbf{C}_{13}^{(1)} = \mathbf{C}_{21}^{(1)} = \mathbf{C}_{22}^{(1)} = -\frac{1}{2}\mathbf{C}_{23}^{(1)} = -\frac{1}{2}\mathbf{C}_{31}^{(1)} \\ = -\frac{1}{2}\mathbf{C}_{32}^{(1)} = \frac{1}{4}\mathbf{C}_{33}^{(1)} = \mathbf{A}^{(1)}(\mu, \phi), \end{aligned}$$

and

$$\begin{aligned} \mathbf{C}_{11}^{(2)}(\mu, \phi) = \frac{1}{2}\mathbf{C}_{12}^{(2)} = \mathbf{C}_{13}^{(2)} = \frac{1}{2}\mathbf{C}_{21}^{(2)} = \frac{1}{4}\mathbf{C}_{22}^{(2)} = \frac{1}{2}\mathbf{C}_{23}^{(2)} = \mathbf{C}_{31}^{(2)} = \frac{1}{2}\mathbf{C}_{32}^{(2)} \\ = \mathbf{C}_{33}^{(2)} = \mathbf{A}^{(2)}(\mu, \phi), \end{aligned} \quad (8.5)$$

the forms of $\mathbf{A}^{(1)}(\mu, \phi)$ and $\mathbf{A}^{(2)}(\mu, \phi)$ being given by (6.6).

From (8.2) and (8.3) we have

$$\mathbf{E}_3(m, \mu, \phi, \mu_0) = \frac{27\sigma s^2 I_\infty}{1024\pi(1 + \frac{1}{2}\delta)^3} \sum_{i=1}^3 \sum_{j=1}^3 \{ \mathbf{C}_{ij}(\mu, \phi, \mu_0) M_{2i-1, 2j-1}(m, \mu_0) \}, \quad (8.6)$$

where

$$M_{2i-1, 2j-1}(m, \mu_0) = \int_0^1 [L d_{2i-1}(m, \mu', \mu_0) + L u_{2i-1}(m, -\mu', \mu_0)] \mu'^{(2j-3)} d\mu'. \quad (8.7)$$

The following expression, referring to the total intensity, may be derived from (8.6)

$$E_3(m, \mu, \phi, \mu_0) = \frac{27\sigma s^2 I_\infty}{1024\pi(1 + \frac{1}{2}\delta)^3} \sum_{i=1}^3 \sum_{j=1}^3 C_{ij} M_{2i-1, 2j-1}(m, \mu_0), \quad (8.8)$$

where C_{ij} briefly denotes $C_{ij}(\mu, \phi, \mu_0)$. We find that

$$\begin{aligned}
 C_{11} &= \frac{1}{2}(1-3\delta)[9-7\mu^2-7\mu_0^2+9\mu^2\mu_0^2+4\mu\mu_0(1-\mu^2)^{1/2}(1-\mu_0^2)^{1/2}\cos\phi \\
 &\quad +\frac{1}{4}(1-\mu^2)(1-\mu_0^2)\cos 2\phi]+\frac{1}{2}\delta(29-9\mu^2-9\mu_0^2+\mu^2\mu_0^2), \\
 C_{12} &= (1-3\delta)[-5+9\mu^2+7\mu_0^2-11\mu^2\mu_0^2+2\mu\mu_0(1-\mu^2)^{1/2}(1-\mu_0^2)^{1/2}\cos\phi \\
 &\quad +\frac{1}{4}(1-\mu^2)(1-\mu_0^2)\cos 2\phi]+\frac{1}{2}\delta(-17+25\mu^2+11\mu_0^2-3\mu^2\mu_0^2), \\
 C_{13} &= \frac{1}{2}(1-3\delta)[(1-3\mu^2)(3-5\mu_0^2)-8\mu\mu_0(1-\mu^2)^{1/2}(1-\mu_0^2)^{1/2}\cos\phi \\
 &\quad +\frac{1}{4}(1-\mu^2)(1-\mu_0^2)\cos 2\phi]+\delta(1-3\mu^2), \\
 C_{21} &= (1-3\delta)[-5+7\mu^2+9\mu_0^2-11\mu^2\mu_0^2+2\mu\mu_0(1-\mu^2)^{1/2}(1-\mu_0^2)^{1/2}\cos\phi \\
 &\quad +\frac{1}{4}(1-\mu^2)(1-\mu_0^2)\cos 2\phi]+\frac{1}{2}\delta(-17+11\mu^2+25\mu_0^2-3\mu^2\mu_0^2), \\
 C_{22} &= (1-3\delta)[11-17\mu^2-17\mu_0^2+27\mu^2\mu_0^2+2\mu\mu_0(1-\mu^2)^{1/2}(1-\mu_0^2)^{1/2}\cos\phi \\
 &\quad +\frac{1}{2}(1-\mu^2)(1-\mu_0^2)\cos 2\phi]+\frac{1}{2}\delta(33-27\mu^2-27\mu_0^2+9\mu^2\mu_0^2), \\
 C_{23} &= (1-3\delta)[-2(1-3\mu^2)(2-3\mu_0^2)-4\mu\mu_0(1-\mu^2)^{1/2}(1-\mu_0^2)^{1/2}\cos\phi \\
 &\quad +\frac{1}{4}(1-\mu^2)(1-\mu_0^2)\cos 2\phi]-3\delta(1-3\mu^2), \\
 C_{31} &= \frac{1}{2}(1-3\delta)[(3-5\mu^2)(1-3\mu_0^2)-8\mu\mu_0(1-\mu^2)^{1/2}(1-\mu_0^2)^{1/2}\cos\phi \\
 &\quad +\frac{1}{4}(1-\mu^2)(1-\mu_0^2)\cos 2\phi]+\delta(1-3\mu_0^2), \\
 C_{32} &= (1-3\delta)[-2(2-3\mu^2)(1-3\mu_0^2)-4\mu\mu_0(1-\mu^2)^{1/2}(1-\mu_0^2)^{1/2}\cos\phi \\
 &\quad +\frac{1}{4}(1-\mu^2)(1-\mu_0^2)\cos 2\phi]-3\delta(1-3\mu_0^2), \\
 C_{33} &= \frac{1}{2}(1-3\delta)[3(1-3\mu^2)(1-3\mu_0^2)+16\mu\mu_0(1-\mu^2)^{1/2}(1-\mu_0^2)^{1/2}\cos\phi \\
 &\quad +\frac{1}{4}(1-\mu^2)(1-\mu_0^2)\cos 2\phi]. \quad \dots \dots \dots (8.9)
 \end{aligned}$$

The treatment of the reception of tertiary scattered light follows that outlined in § 6 and § 7 for the reception of primary and secondary scattered light respectively. Thus we write

$$\begin{aligned}
 &\mathbf{R}d_3(m, \mu, \phi, \mu_0) \\
 &= \frac{27s^3I_\infty}{1024\pi(1+\frac{1}{2}\delta)^3\mu} \sum_{i=1}^3 \sum_{j=1}^3 \{ \mathbf{C}_{ij}(\mu, \phi, \mu_0) Md_{2i-1, 2j-1}(m, \mu, \mu_0) \}, \quad (8.10)
 \end{aligned}$$

and

$$\begin{aligned}
 &\mathbf{R}u_3(m, \mu, \phi, \mu_0) \\
 &= -\frac{27s^3I_\infty}{1024\pi(1+\frac{1}{2}\delta)^3\mu} \sum_{i=1}^3 \sum_{j=1}^3 \{ \mathbf{C}_{ij}(\mu, \phi, \mu_0) Mu_{2i-1, 2j-1}(m, \mu, \mu_0) \}, \quad (8.11)
 \end{aligned}$$

where

$$\begin{aligned}
 &Md_{2i-1, 2j-1}(m, \mu, \mu_0) \\
 &= K(m, \mu) \int_0^m K(m', -\mu) M_{2i-1, 2j-1}(m', \mu_0) dm', \quad \dots \dots \dots (8.12)
 \end{aligned}$$

and

$$\begin{aligned}
 &Mu_{2i-1, 2j-1}(m, \mu, \mu_0) \\
 &= K(m, \mu) \int_m^1 K(m', -\mu) M_{2i-1, 2j-1}(m', \mu_0) dm'. \quad \dots \dots \dots (8.13)
 \end{aligned}$$

§ 9. CONCLUSION

The preceding analysis completes the formal solution of the problem considered. We now have expressions for the primary, secondary, and tertiary scattered light-intensities emitted and received in any direction and at any point in the atmosphere. For each order of scattering, the vector representing the light-intensity is given in terms of the product of an azimuthal vector and a function generally involving a multiple integral. Similar products would evidently be derived by extending the treatment to higher orders of scattering.

We have had in mind the scattering of ultra-violet sunlight, but the particular results which would obtain by reducing the absorption coefficient of ozone to zero, might be utilized in the study of the illumination of the earth's atmosphere by visible light. Numerical results for an atmosphere containing an absorbing layer of ozone will be given in a forthcoming paper.

ACKNOWLEDGMENT

The author wishes to thank Professor S. Chapman for introducing him to this subject, and for several stimulating discussions.

REFERENCES

- CHANDRASEKHAR, S., 1946, *Astrophys. J.*, **104**, 111; 1948, *Ibid.*, **107**, 199; 1950, *Radiative Transfer* (Oxford: Clarendon Press), (a) p. 37, (b) p. 40, (c) p. 50, (d) p. 285.
- CHAPMAN, S., 1935, *Phil. Trans.*, **234**, 230.
- DOBSON, G. M. B., 1951, *Quart. J. R. Met. Soc.*, **77**, 493.
- HAMMAD, A., 1948, *Astrophys. J.*, **108**, 338; 1953, *J. Opt. Soc. Amer.*, **43**, 187.
- HAMMAD, A., and CHAPMAN, S., 1939, *Phil. Mag.*, **28**, 99.
- STOKES, G. G., 1852, *Trans. Camb. Phil. Soc.*, **9**, 399.

XXXII. On the Problem of Energy Eigenvalue and Degeneracy in Quantum Mechanics

By H. NARUMI

Yukawa Laboratory, Institute for Chemical Research,
Kyoto University, Kyoto, Japan*

[Received in revised form November 20, 1954]

THE existence of the group of contact transformations, or that of the continuous Schrödinger group whose elements are commutative with Hamiltonian is essentially related not only to the problem of degeneracy, as shown by Jauch and Hill (1940), but also to the problem of quantization. In the present paper it is shown that on the basis of the representations of the semi-simple Lie group generated by the integral operators F_λ ($\lambda=1, 2, \dots, r$), which can be made by the method of *classical analogy* from a set of γ independent integrals of the equations of motion in Newtonian mechanics, an eigenvalue problem can be constructed in terms of a complete set of the generalized Casimir operators

$$G_i = G_i(F_\lambda); \quad (i=1, 2, \dots, l), \quad . \quad . \quad . \quad (1)$$

where l means the rank of the semi-simple group, and all G_i constructed from the invariants of the adjoint group are commutative with any F_λ . An explicit formula of G_i , as pointed out by Racah (1950, 1951), is

$$\sum_{\lambda, \mu, \dots, \nu} g_{\lambda\mu\dots\nu} F^\lambda F^\mu \dots F^\nu = \sum_{\lambda, \mu, \dots, \nu} g^{\lambda\mu\dots\nu} F_\lambda F_\mu \dots F_\nu \quad . \quad . \quad . \quad (2)$$

and metric fundamental tensors are given by

$$g_{\lambda\mu\dots\nu} = \sum_{\alpha, \beta, \dots} c_{\lambda\alpha}^\beta c_{\mu\beta}^\gamma \dots c_{\nu\gamma}^\alpha \quad . \quad . \quad . \quad (3)$$

The structure constants $c_{\lambda\mu}^\nu$ of the Lie group may be at most operators depending on the Hamiltonian alone, and in principle they are not always identical with classical ones. The quantization procedure by the use of the representations of these operators is generally applicable to any quantum-mechanical system, as far as it is possible to find the above mentioned Schrödinger group for the system, although this restriction is considerably rigorous.

Let us consider the present problem about a typical example of the hydrogen like atom. The six integral operators commutative with the non-relativistic Hamiltonian

$$H = p^2/2m + Ze^2/r^2 \quad . \quad . \quad . \quad (4)$$

of this system are, as well-known, the Lenz-Pauli vector integral

$$\mathbf{A} = (1/2mZe^2)(\mathbf{M} \times \mathbf{p} - \mathbf{p} \times \mathbf{M}) + \mathbf{r}/r \quad . \quad . \quad . \quad (5)$$

in addition to the orbital angular momentum operator $\mathbf{M} = \mathbf{r} \times \mathbf{p}$, where m , \mathbf{p} , and e are the electron mass and momentum, and the elementary

* Communicated by the Author.

charge, respectively ; r , the distance between a given nucleus and electron, Ze , the nuclear charge. For the negative energy state the Balmer formula was formerly derived by Hulthén (1933) using the commutation relation of the above integral (5) and it was already shown by Fock (1936) and Bargmann (1936) that the Schrödinger group of this system is isomorphic with the four-dimensional rotation group, while from our point of view the set composed of the above six operators might be regarded as a semi-simple group of the rank 2, therefore there must exist a set of two generalized Casimir operators. But in this case it can be found that only one ordinary Casimir operator (1931) of these has the following functional relation with the Hamiltonian :

$$G = -\frac{1}{2} \sum_{\lambda=1}^4 F_{\lambda}^2 = -(Z^2 e^4 m / 2 \hbar^2 H) - 1, \quad . \quad . \quad . \quad (6)$$

where \hbar is the Planck constant h divided by 2π . Each highest weight characterizing the irreducible representations of the Lie group is $(0, 0)$, $(1, 0)$, \dots , $(k, 0)$, \dots , and then the degrees of their representations are $1^2, 2^2, \dots, (k+1)^2, \dots$, respectively. The eigenvalue of the Casimir operator determined by a given highest weight $(k, 0)$ is $k(k+2)$, which is also connected with the eigenvalue of angular momentum in the four-dimensional Euclid space. Consequently by substituting n for $k+1$ the relation (6) can be reduced to

$$n^2 - 1 = -(Z^2 e^4 m / 2 \hbar^2 H_n') - 1.$$

or

$$H_n' = -Z^2 e^4 m / 2 \hbar^2 n^2; \quad (n=1, 2, \dots). \quad . \quad . \quad . \quad (7)$$

which is the well-known Balmer formula accompanied with the degree of degeneracy $(k+1)^2 = n^2$ as mentioned above.

On the other hand it is known that the Schrödinger group of the positive energy state of this system is isomorphic with the Lorentz group. In the case of the continuous eigenvalue we (1953) found an infinite continuous (unitary) representation of a non-compact Lie group, which will be presented elsewhere, besides some applications of this procedure to other examples and the perturbation theory had also been formulated.

REFERENCES

- BARGMANN, V., 1936, *Z. Phys.*, **99**, 576.
 CASIMIR, H., 1931, *Proc. Roy. Acad. Amsterdam*, **34**, 144.
 FOCK, V., 1936, *Z. Phys.*, **98**, 145.
 HULTHÉN, L., 1933, *Z. Phys.*, **86**, 21.
 JAUCH, J. M., and HILL, E. L., 1940, *Phys. Rev.*, **57**, 641.
 NARUMI, H., and MATSUO, S., 1953, read in the annual meeting of the Physical Society of Japan.
 RACA, G., 1950, *Rendiconti dell'Accademia Nazionale dei Lincei*, **8**, 108; 1951, *Lectures on Group Theory and Spectroscopy*, Princeton (unpublished).

XXXIII. *Neutron Attenuation Measurements in Heavy and Light Water at Energies between 109 and 169 mev*

By R. ALPHONCE, A. JOHANSSON, A. E. TAYLOR* and G. TIBELL
The Gustaf Werner Institute for Nuclear Chemistry, University of
Uppsala, Uppsala, Sweden†

[Received November 18, 1954]

ABSTRACT

The difference between the total cross section of deuterium and hydrogen has been obtained at effective energies of 109, 117, 132, 149 and 169 mev from attenuation measurements on light and heavy water. Using published values of the hydrogen cross section, the oxygen total cross section was also obtained at these energies.

§ 1. INTRODUCTION

PREVIOUS measurements of the difference between the neutron total cross sections of deuterium and hydrogen have been made in the high energy region at 42 mev (Hildebrand and Leith 1950), 85 mev (Cook, McMillan, Peterson and Sewell 1949), 95 mev (DeJuren and Knable 1950), 270 mev (DeJuren 1950), 280 mev (Fox, Leith, Wouters and MacKenzie 1950) and 400 mev (Nedzel 1954). Neutrons produced by the 230 cm Uppsala synchro-cyclotron were used in the present work, and the experimental method was similar to that used in determinations of neutron total cross sections at Harwell, England (Taylor and Wood 1953). The results at 169 mev have been communicated earlier (Taylor 1953).

§ 2. EXPERIMENTAL

(a) *Geometrical Layout*

The circulating proton beam in the cyclotron was intercepted by a beryllium target (30 mm thick), the radial position of which was changed in order to obtain the different neutron energies. The neutrons emerging from the target passed successively through a thin aluminium window in the tank wall, a steel collimator, the attenuator, another steel collimator situated in the concrete shielding wall, and then struck the polythene scatterer (fig. 1). The target, collimator holes, attenuator holder, and polythene scatterer were carefully aligned. The distance between the target and polythene scatterer was 14 m, between target and attenuator 8.5 m, and the diameter of the steel collimator holes was 39 mm.

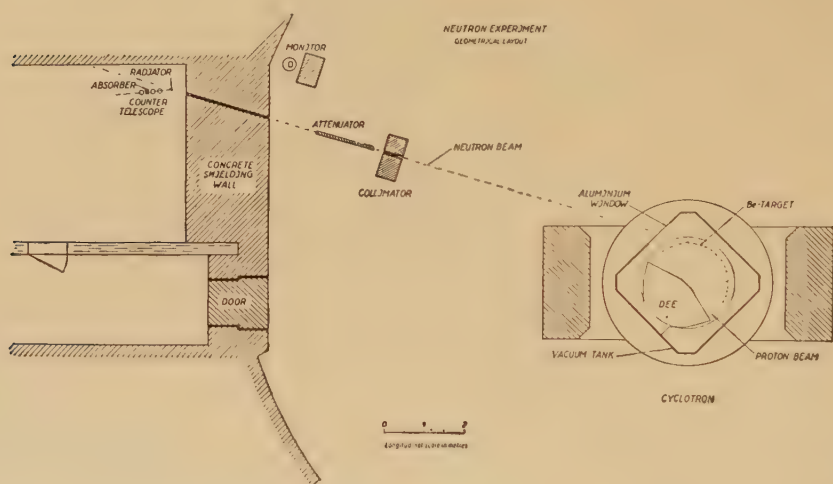
* Now at A.E.R.E., Harwell, Berks., England.

† Communicated by Professor The Svedberg, F.R.S.

(b) Neutron Detector

Recoil protons emerging from the polythene scatterer (17 mm thick and 50 mm diameter) at an angle of 20° to the direction of the neutron beam were detected by a triple coincidence counter telescope using scintillation counters. The polythene scatterer was perpendicular to the direction of the telescope. Each scintillation counter consisted of a polystyrene crystal (7 mm thick and 25 mm square) mounted on top of a photomultiplier tube (EMI 5311) in a light tight aluminium case. An aluminium absorber was placed between the last two counters in order to set a lower energy limit to the recoil protons detected (see table). The coincidence circuit was of the bridge type using germanium diodes, and had a resolving time of 10^{-8} sec. A block diagram of the electronic equipment is shown in fig. 2.

Fig. 1



In order to find the best operating conditions of the coincidence circuit the counting rate was recorded for various counter and discriminator voltages until a plateau of counting rate against voltage was obtained.

(c) Neutron Monitor

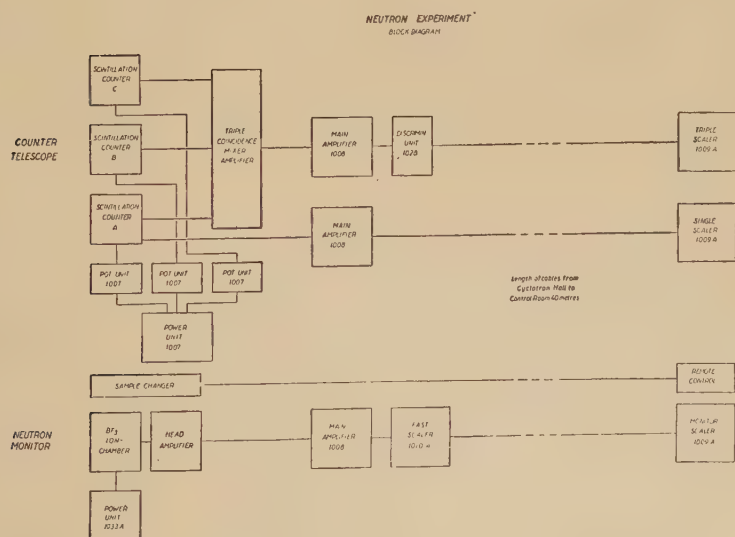
The neutron output of the cyclotron was monitored by a BF_3 counter placed in a cylinder of paraffin wax, situated behind a concrete shielding in the cyclotron hall. The operating conditions were determined as for the counter telescope.

(d) Attenuators

The ordinary and heavy water samples were contained in copper tubes (52 mm diameter) with copper end windows (0.5 mm thick). A remotely controlled sample changer held the required sample in position, and also had a position for an unattenuated beam. The tubes of ordinary and heavy water were of such lengths that they contained the same number of oxygen atoms when filled. The heavy water contained 99.75% of D_2O .

Effective neutron energy Mev	169 ± 3	149 ± 2	132 ± 2	117 ± 2	109 ± 2
Energy band width Mev	19	23	25	31	22
Contribution to the counting rate from carbon content of scatterer %	10	12	12	12	8
Aluminium g cm^{-2}	12.97	9.19	6.48	3.78	5.24
Deuterium minus hydrogen cross section 10^{-27} cm^2	23.1 ± 2.0	24.8 ± 2.0	25.3 ± 2.4	27.2 ± 2.4	29.1 ± 3.6
Oxygen cross section 10^{-27} cm^2	431 ± 6	473 ± 6	518 ± 6	598 ± 6	656 ± 6
Hydrogen cross section used in deriving oxygen cross section 10^{-27} cm^2	48 ± 2	50 ± 2	54 ± 2	59 ± 2	64 ± 2

Fig. 2



§ 3. EFFECTIVE NEUTRON ENERGY

The counting rates were recorded for various thicknesses of absorber in the telescope and these thicknesses were converted to neutron energies using the range-energy relation and the relativistic formula connecting recoil proton energy to incident neutron energy. The effective neutron energy was taken as the mean value of the neutron energies weighted by the corresponding number of recoil protons. This method assumes

that the total cross section does not vary appreciably over the energy band in question. Further, if an energy band greater than 13 mev is used there will be a contribution to the detected protons from the carbon content of the polythene and this will have a different effective neutron energy. To estimate this effect the counting rate was measured for a carbon scatterer of the same stopping power as the polythene scatterer. This contribution from the carbon content in the polythene scatterer, together with the energy band used, are recorded in the table. Since the radiator and the last crystal have a finite thickness which cannot be neglected and since the solid angle is not negligibly small, there is an uncertainty in the calculation of the effective neutron energy. An estimate of this uncertainty is included in the effective neutron energy.

§ 4. EXPERIMENTAL PROCEDURE

A total counting time of about 40 hours was required to obtain an accuracy of 10% in the deuterium minus hydrogen cross section. In order to reduce possible systematic errors due to long-term shifts in electronic equipment the experiment was divided into shorter runs of about one hour. A complete run consisted of successive measurements of the ratio of triple coincidence counts to monitor counts with each of the two attenuators in position and without an attenuator. The overall spread of the readings was no greater than expected from the total counts taken.

By inserting delay cables in the third channel of the triple coincidence counter it was found that the background of random triple coincidences was negligible.

§ 5. RESULTS

The cross sections calculated from the measured attenuations are listed in the table. The light water content in the heavy water sample was found to be negligible when calculating the deuterium minus hydrogen cross sections, but small corrections had to be applied for the copper end windows when calculating the oxygen cross section from the attenuation in light water. The values of the hydrogen cross section used in the latter calculation were obtained by interpolation from published values and are listed in the table.

The values obtained in this experiment agree with those obtained by others, at higher and lower energies.

ACKNOWLEDGMENTS

The authors wish to thank Professor The Svedberg for extending the facilities of his laboratory; Dr. H. Tyrén for active encouragement; U. Tallgren for constructing the coincidence circuit; G. Hanson for making the collimators and the sample changer; and the cyclotron crew for help and assistance.

REFERENCES

- COOK, L. J., McMILLAN, E. H., PETERSON, J. M., and SEWELL, D. C., 1949, *Phys. Rev.*, **72**, 1264.
- DEJUREN, J., 1950, *Phys. Rev.*, **80**, 27.
- DEJUREN, J., and KNABLE, M., 1950, *Phys. Rev.*, **77**, 606.
- FOX, R., LEITH, C., WOUTERS, L., and MACKENZIE, K. R., 1950, *Phys. Rev.*, **80**, 23.
- HILDEBRAND, R. H., and LEITH, C. E., 1950, *Phys. Rev.*, **80**, 842.
- NEDZEL, V. A., 1954, *Phys. Rev.*, **94**, 174.
- TAYLOR, A. E., 1953, *Phys. Rev.*, **92**, 1071.
- TAYLOR, A. E., and WOOD, E., 1953, *Phil. Mag.*, **44**, 95.

XXXIV. *Study of Charged Heavy Unstable Cosmic Ray Particles*

By P. R. BARKER, D. M. BINNIE, B. D. HYAMS and R. J. ROUT
The Physical Laboratories, The University, Manchester *

[Received December 3, 1954]

ABSTRACT

A technique for the direct counter detection of heavy unstable cosmic ray particles stopping in a cloud chamber is described. It is shown that the method is about three times more efficient than methods previously used when detecting particles with lifetimes greater than 5×10^{-9} sec. The observation of eight, well-identified, unstable particles is reported; they all have properties consistent with the K_μ -particle.

§ 1. INTRODUCTION

SINCE the initial discovery of charged heavy mesons cloud chamber observations of these particles have been obtained by photographing penetrating showers. Nuclear emulsion experiments (Fowler *et al.* 1951) indicate that about 3×10^{-3} heavy mesons stop per gram per day beneath 30 cm of lead at an altitude of 3000 m. However, multiplate cloud chambers, when selecting energetic penetrating showers in a conventional manner, identify only 0.6×10^{-6} S-particles per gram per day at this altitude (Bridge *et al.* 1953). It was therefore thought worthwhile to attempt the direct selection of charged heavy mesons. This paper describes an experiment in which a multiplate cloud chamber is triggered by a counter system which responds directly to heavy unstable charged particles. About 1.4×10^{-6} heavy mesons are identified per gram per day in this experiment.

§ 2. PRINCIPLE OF EXPERIMENT

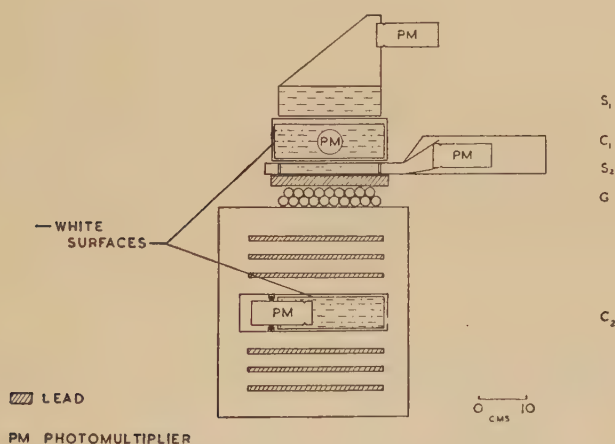
The selection system and cloud chamber are shown in fig. 1. The counter system above the cloud chamber consists of two liquid scintillation counters S_1 and S_2 , a Čerenkov counter C_1 , and a double row of Geiger counters G. There is a layer of 1.5 cm of lead between S_2 and G. The cloud chamber beneath these counters contains six lead plates and a Čerenkov counter C_2 .

The Čerenkov counters give signals only when traversed by fast particles. They are lined with diffusely reflecting surfaces, and respond to the total amount of Čerenkov light emitted without making use of its directional properties.

* Communicated by G. D. Rochester

The counter system above the chamber selects heavy particles by means of coincidences $S_1 + S_2 + G - C_1$, which will be referred to as H coincidences. This selection implies that a particle with velocity less than a critical velocity v_w and range greater than R_0 g cm⁻² (the amount of material between C_1 and G) has traversed the system. Thus the particle must have a mass greater than $M_0(v_w, R_0)$. This system of selecting heavy particles has been described previously by Duerden and Hyams (1952), who showed that $M_0 c^2 \geq 6.8 R_0$ mev when v_w is the critical velocity for water. In this experiment R_0 is chosen so that $M_0 \geq 300$ electron masses (m_e), in order to exclude light mesons (π and μ).

Fig. 1



Front view scale drawing of counter selection system, and cloud chamber.

The cloud chamber is expanded when coincidences $H + C_2$ occur within a resolving time of 5×10^{-6} sec. In general no single downward-moving particle can actuate the system, since it would have to be moving slowly at C_1 and rapidly at C_2 .

Thus the system is designed to select slow particles with mass greater than $300 m_e$ which emit fast decay or annihilation products.

The C_2 signal amplitude for $H + C_2$ coincidences is recorded on a cathode ray oscillograph to enable the velocity of heavy-particle decay products to be measured.

To detect short-lived unstable particles it is necessary to place a layer of material above the chamber. However, a slow heavy meson will not actuate the H system if accompanied by a fast particle giving an anti-coincidence signal in the C_1 counter. For this reason the lower surface of the production layer was placed 80 cm above the counter (C_1) to allow the slow heavy mesons to separate from any fast shower particles associated with their production.

In the first half of the experiment a production layer of 80 cm depth of paraffin was used. It was thought that this would give few fast shower particles accompanying the heavy mesons, and that γ -rays from any π^0 -mesons produced would give only small electron showers in the paraffin. In the latter half of the experiment a layer of 14.5 cm of lead was used instead of the paraffin, in the belief that heavy mesons may be produced mainly by π -meson nucleon interactions, in which case large nuclei should be better targets for heavy meson production than small ones. It was hoped that any electron cascades associated with the heavy meson production would be absorbed by the lead. The area of each production layer was $150 \times 150 \text{ cm}^2$.

There was no significant difference between the rates of observing unstable particles beneath lead and paraffin. Beneath paraffin the apparatus was triggered much more often by air showers and it was necessary to limit the counting rate by requiring coincidences from an additional set of Geiger counters placed above S_1 .

The time required for a particle produced in the paraffin or lead to come to rest in the cloud chamber is about 5×10^{-9} sec. Therefore the system can respond efficiently only to particles with lifetimes between 5×10^{-9} and 5×10^{-6} sec. Antiparticles, stable in flight but with very rapid annihilation, can also be detected.

§ 3. DESCRIPTION OF APPARATUS

The scintillation counter S_1 is filled with terphenyl in xylene, and S_2 with terphenyl in phenylcyclohexane. Each of these counters has an active area of about $20 \times 20 \text{ cm}^2$.

The Čerenkov counter C_1 , filled with distilled water, contains two photomultipliers to give high efficiency. It has an active area of $22 \times 22 \text{ cm}^2$ and a depth of 6.6 cm. Under normal running conditions pulses greater than about one-tenth the mean signal from relativistic particles give an anticoincidence signal.

The counter C_2 is made of $\frac{1}{8}$ inch brass and has a sealed dry compartment at one side for the base and wiring of the photomultiplier. The active area of the counter is $21 \times 27 \text{ cm}^2$ and the depth of the liquid is 6.3 cm. A 19-core cable brings out connections to each dynode of the photomultiplier and also two small tubes to maintain the dry and the liquid-filled compartments at atmospheric pressure. The dynode resistor chain is mounted externally to avoid having a source of heat in the cloud chamber. The signal from the collector electrode is brought out through a separate coaxial cable. Both cables are sealed to the counter and the cloud chamber by means of rubber O-rings. In over six months of operation no difficulties have arisen from running this counter inside the cloud chamber.

The counter C_2 is filled with a mixture of equal volumes of glycerine and water in order to lower the critical velocity and thus increase the efficiency of detecting decay particles. The critical velocity, v_g , for this mixture is 0.71 c , which is still sufficiently high so that a slow proton which

just fails to give a signal in C_1 has a very small probability of giving a signal in C_2 . Signals in C_2 greater than about one-quarter of the mean signal from fast vertical particles give coincidence pulses.

All the photomultipliers are E.M.I. type 6262 14 stage tubes.

The cloud chamber, which has a photographed region 35 cm high, 28 cm wide, and 35 cm deep, is illuminated from the rear, the expansion being obtained with two rubber membranes at the sides of the chamber.

Each of the six lead plates has a thickness of about 1 cm, with a weight of 11.0 g cm⁻². The total vertical thickness of C_2 is equivalent, with regard to ionization losses, to about 20 g cm⁻² of lead.

§ 4. OBSERVATIONS

The observations described in this paper were made at the Observatory of the Pic du Midi, at an altitude of 2850 m. The equipment was run for a period of about four and a half months during which it operated successfully for about 2000 hours.

Under 14.5 cm of lead 2520 H coincidences were registered per day. From a run of three days, photographing such events without requiring a coincident C_2 pulse, it was concluded that of these events 529 per day were due to protons stopping in the part of the chamber which was photographed.

Spurious Events

The unstable particle selection system ($H+C_2$ coincidences) registered 67 counts per day. Since the chamber recycling time was 5 minutes, 56 pictures per day were photographed. Analysis of these pictures indicated that 19 per day showed evidence of an electron cascade in the chamber. Most of these were probably events in which different particles from electron showers traversed the counters S_1 , S_2 , G. and C_2 , without passing through C_1 .

Three photographs per day showed a slow proton traversing the photocathode or first dynode of the photomultiplier in the counter C_2 . This rate exceeded the accidental rate of such events by a factor of at least 12. These events can only be attributed to pulses in the photomultiplier initiated by a charged particle causing fluorescence or direct secondary electron emission in the tube, rather than any effect due to Čerenkov radiation.

Ten pictures a day showed single particles traversing the cloud chamber, with trajectories passing through the selection system. Most of these may be attributed to fast protons which, due to statistical fluctuations in the signals, failed to be detected at C_1 but were detected at C_2 .

Twenty-one pictures a day showed no charged particles traversing the counter C_2 , in spite of the fact that its whole active area was photographed. These can be attributed to γ -rays from diffuse air showers, and the rate is consistent with this assumption.

Three pictures a day showed a particle coming to rest in the cloud chamber lead plates, with no visible charged secondary particle, and no visible charged particle traversing C_2 . This rate was eight times greater than could be accounted for by random coincidences between stopping protons and random counts (100 per sec) in the counter C_2 . Some of these events were probably due to slow protons giving rise to nuclear excitation with the detection of subsequent nuclear γ -rays by C_2 .

Unstable Particles

About 0.1 pictures a day showed particles appearing from ionization to stop in one of the lead plates and having minimum ionization tracks which begin within 1 cm of the point of stopping and enter C_2 . Plate 4 shows two such events, which will be referred to as S-events. In all, 8 well-identified S-events have been photographed. In three of these events the range of the secondary particles is more than 60 g cm^{-2} of lead. Of the 8 events 5 were observed under the paraffin production layer.

None of the secondary particles show evidence of multiplication or large angles of scattering as might be expected of electrons, although four of the eight traverse at least 1 cm of lead before leaving the chamber, and one of the others traverses C_2 . The remaining three enter C_2 with steeply inclined trajectories which go out through the sides without reappearing in the visible region.

The fact that few of these could be due to stopping light mesons is evident even without reference to the properties of the H-selection system for all the S-events had lifetimes less than $4 \times 10^{-8} \text{ sec}$ (see following paper). Since the resolving time of the counters is $5 \times 10^{-6} \text{ sec}$ the probability is 2×10^{-2} that one of these events is due to a π^- or μ^- -meson, and 1.6×10^{-7} that four of the events are due to π^- or μ^- -mesons.

Taking these observations into account we consider that it is unlikely that even one of the S-events could be attributed to a stopping π^- or μ^- -meson, and that they are all due to the stopping and decay of heavy mesons.

In none of the S-pictures do we observe any evidence for γ -rays associated with the stopping particles, either in the direction opposed to that of the charged secondary, or in any other direction.

In principle, the track length of the secondary particle through the counter C_2 , and the C_2 pulse amplitude, determine the velocity of the particle as it traverses the counter. In practice, the fluctuation of the signals makes any one velocity determination very inaccurate. However, if it is assumed that all the secondary particles are monoenergetic μ^- -mesons and allowance is made for the slowing down before reaching C_2 , the mean velocity of the eight particles may be determined. It is found to be $(0.93_{-0.03}^{+0.04})c$ which corresponds to a mean initial momentum of $(275_{-60}^{+160}) \text{ mev}/c$, the errors being calculated from the r.m.s. deviation of the mean C_2 pulse amplitude

§ 5. DISCUSSION

It is consistent with present knowledge to identify all our S-events with the K_μ -particle identified by Gregory *et al.* (1954). In no case did we bring the charged secondary particle to the end of its range, since the chamber was too small for this to be probable. Thus we may place only a lower limit on the range of the decay particles. To give a coincidence in C_2 the momentum of the decay particles, if assumed to be μ -mesons, must exceed 110 mev/c when they traverse the counter. The mean initial velocity observed for the eight particles using the C_2 pulse amplitudes corresponded to an initial momentum of (275^{+160}_{-60}) mev/c which is compatible with that of the K_μ -meson. The absence of γ -ray decay products, and the long distance of flight before decay of these heavy mesons is also consistent with the properties of the K_μ -particle.

For every S-particle photographed 1750 protons traversed the selection system and stopped in the corresponding plates of the cloud chamber. If allowance is made for the geometrical inefficiency for detecting the S-particle decay products (assumed to be μ -mesons with momentum 220 mev/c) we find a ratio of 300 protons to one S-particle stopping in the chamber.

The inefficiency of counting S-particles due to the C_1 anticoincidence may be estimated in various ways. We may compare the observed S-particle counting rate with that predicted by the emulsion data. We may also compare the observed ratio of stopping S-particles to protons with that obtained by Gregory (1954) and note that we obtain the same proton flux as Miller *et al.* (1954). From these arguments we conclude that our efficiency for S-particle detection is certainly not reduced to less than 30% due to the C_1 anticoincidence.

Stopping τ -mesons can give rise to relativistic decay particles, either through the usual $\pi-\mu-\beta$ decay, or through electron pairs from the probable alternative $\pi^0-\gamma$ decay. In the former case the detection efficiency for the electrons is not very high. In either case, positive identification from the cloud chamber pictures is difficult. Although some events compatible with τ -mesons have been observed, no satisfactory conclusions can be drawn from these.

The selection system would respond efficiently to stopping anti-protons, but although during the running time of the experiment 5×10^4 protons have traversed the counters and come to rest in the chamber, no evidence for such particles has been obtained.

ACKNOWLEDGMENTS

The authors wish to thank Professor P. M. S. Blackett and Dr. G. D. Rochester for their support and encouragement of this experiment.

They wish to express thanks to Dr. J. Rösch, Director of the Pic-du-Midi Observatory, and his staff, who have made work at the Observatory both possible and pleasurable.

They wish to thank Dr. T. Duerden for his active contribution to early stages of the work.

One of us (P. R. B.) is indebted to the United States Educational Commission in the United Kingdom for financial support.

One of us (R. J. R.) is indebted to the Department of Scientific and Industrial Research for a maintenance grant.

REFERENCES

- BRIDGE, H. S., PEYROU, C., ROSSI, B., and SAFFORD, R., 1953, *Phys. Rev.*, **90**, 921.
DUERDEN, T., and HYAMS, B. D., 1952, *Phil. Mag.*, **40**, 717.
FOWLER, P. H., MENON, M. G. K., POWELL, C. F., and ROCHAT, O., 1951, *Phil. Mag.*, **42**, 1040 (see also report on "Heavy Meson Conference" Bristol, Dec. 1951).
GREGORY, B., LAGARRIGUE, A., LEPRINCE-RINGUET, L., MULLER, F., and PEYROU, CH., 1954, *Nuovo Cimento*, **11**, 292.
GREGORY, B., 1954. We are indebted to Dr. Gregory for communicating this information to us privately.
MILLER, C. E., HENDERSON, J. E., POTTER, D. S., TODD, J., JR., SANDSTROM, W. M., GARRISON, G. R., DAVIS, W. R., and CHARBONNIER, F. M., 1954, *Phys. Rev.*, **93**, 590.

XXXV. *Measurements of the Lifetimes of Charged Heavy Unstable Particles*

By P. R. BARKER, D. M. BINNIE, B. D. HYAMS, R. J. ROUT
and J. SHEPHERD

The Physical Laboratories, The University, Manchester *

[Received December 3, 1954]

ABSTRACT

A new counter method for measuring the lifetime of unstable mesons is described. Lifetime measurements on 13 charged heavy mesons are reported. It is concluded that if there exists only one heavy meson giving fast decay products, with a lifetime greater than 5×10^{-9} sec, its lifetime is $(11.0^{+4.1}_{-2.4}) \times 10^{-9}$ sec. No evidence for any longer-lived heavy mesons has been found.

§ 1. INTRODUCTION

FOR some years it has been thought that there exists at least one type of charged heavy meson with a lifetime longer than 2×10^{-9} sec. The measurement of such a lifetime (see Rochester and Butler (1953) for a survey of early work), has eluded previous cloud chamber observations. This is because the lifetime is long compared with the time of flight across a chamber, and in a multiplate chamber, as in nuclear emulsions, practically all the particles come to rest before decay. Using the particle selection system described in the previous paper (referred to as I), a scintillation and a Čerenkov counter enable the lifetime of single heavy mesons to be measured directly. The particles are identified from cloud chamber photographs.

§ 2. METHOD OF MEASUREMENT

The counter system described in I (see fig. 1 of that paper) was used in conjunction with a cathode ray oscillograph to measure the time elapsing between a heavy meson traversing counter S_1 and a decay particle traversing counter C_2 .

The time scale is calibrated by measuring the time base velocity and the separation of pulses from fast cosmic ray particles which traverse counters S_1 , S_2 , and C_2 .

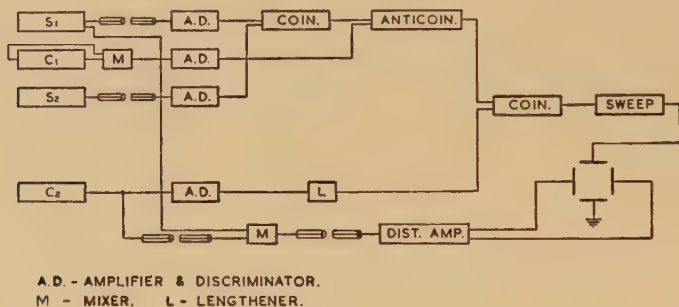
These observations, in conjunction with the cloud chamber photographs, enable one to calculate the lifetimes of the heavy mesons in their rest system. In fact the contributions to the lifetime due to times of flight were in all cases less than 5×10^{-10} sec.

* Communicated by G. D. Rochester.

§ 3. TECHNIQUES

A block diagram of the counters and fast electronic selection and timing system is shown in fig. 1. The auxiliary circuits used in conjunction with the cloud chamber to give a 5×10^{-6} sec resolving time are not shown. The amplifiers, discriminators, and coincidence circuits are all of conventional design. The $S_1 + S_2$ coincidence circuit introduces 50 μ sec of inoperative time after each coincidence so that photomultiplier after-pulses from the 10^5 fast particles traversing the system each day cannot give delayed $S_1 + S_2 + C_2$ coincidences, which would evade the C_1 anti-coincidence pulses.

Fig. 1



Block diagram of fast electronic selection system, and timing-pulse display.

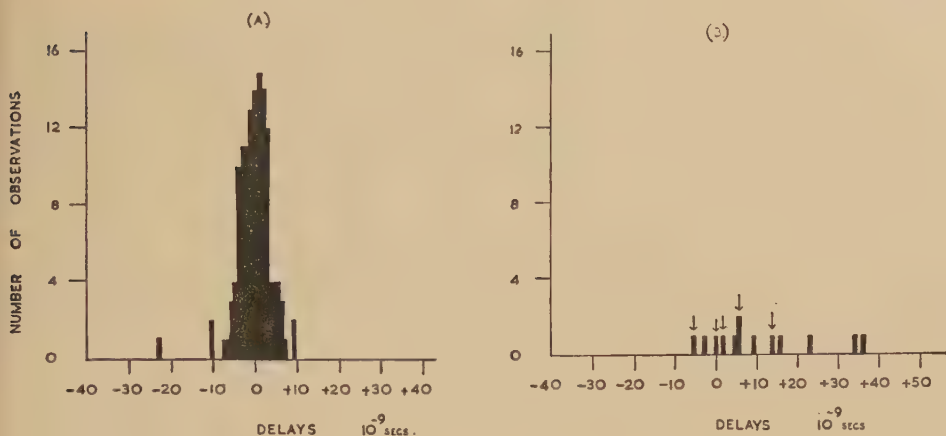
The C_2 signals are delayed by 5×10^{-8} sec with respect to the S_1 signals, and then added to them. The S_1 signal which is a step, and the C_2 signal, a pulse of opposite polarity, are amplified by the same distributed amplifier and displayed on a cathode ray oscillograph. Plate 5 shows some typical oscillograph records. The time base velocity is 5×10^7 cm sec $^{-1}$, and the distributed amplifier rise time is about 7×10^{-9} sec.

The S_1 light pulses are larger and more uniform in amplitude than those in C_2 . Displaying the S_1 signal as a step ensures that S_1 photomultiplier after-pulses are not added to the C_2 signal and do not introduce timing errors. A correlation between the timing calibration and the C_2 pulse amplitude was observed, and all timing measurements were corrected for this effect.

A photograph of the oscillograph is taken for every coincidence $S_1 + S_2 - C_1 + C_2$. If a cloud chamber picture is taken at the same time, the signals from C_1 are temporarily stopped and one oscillograph calibration picture is taken at the next $S_1 + S_2 + C_2$ coincidence. Since most of the $S_1 + S_2 + C_2$ coincidences are due to single fast mesons, these oscillograph pictures are used to determine the mean pulse separation for fast particles and to give an estimate of the error in this measurement. The time distribution of a set of 126 $S_1 + S_2 + C_2$ coincidences is shown in fig. 2 (a). The r.m.s. deviation of a single timing observation in such a

set is about 3×10^{-9} sec. Unexplained instrumental changes over a period of hours sometimes increased the error on a single time determination to as much as 4×10^{-9} sec.

Fig. 2



- (a) Distribution of delays from 126 calibration signals from fast mesons.
 (b) Distribution of delays from 13 heavy mesons. The 5 events not unambiguously identified are marked with arrows.

The observed lifetime t_s of an S-particle in its rest frame is given precisely by

$$t_s = t_d - t_c + \left\{ \int \frac{dx_1}{\gamma_1 v_1} - \int \frac{dx_1}{v_1} - \int \frac{dx_2}{v_2} + \frac{L}{c} \right\}$$

where t_d , t_c , are the separation between the S_1 and C_2 pulses for the S-particles and calibration particles respectively; x_1 , v_1 , γ_1 , are the position, velocity, and time dilation factor, for the heavy meson; x_2 , v_2 the position and velocity of the decay particle; L , c , are the mean track length and velocity for calibration particles. In fact the terms in the brackets contribute in no case more than 0.5×10^{-9} sec to the interval t_s , which is much less than the standard deviation on a single timing measurement.

Figure 2(b) shows the distribution in lifetimes of the 8 S-particles described in paper I. If we assume that all these particles are of the same nature, we find for the reciprocal of the mean lifetime, and its standard deviation $1/\tau = (0.063 \pm 0.022) \times 10^9 \text{ sec}^{-1}$, giving $\tau = (15.8 \pm 8.7) \times 10^{-9} \text{ sec}$. The timing inaccuracy contributes little to the error, which is mainly due to the small number of events observed.

There are also five events in which for various reasons the identification as an S-particle is not unambiguous. We estimate, however, that not more than one of these is due to any other type of event. The delays associated with these five events are shown in fig. 2(b). We attribute the small mean delay of these five observations to a statistical fluctuation.

Thus we consider that the lifetime of $(11.0^{+4.1}_{-2.4}) \times 10^{-9}$ sec obtained by combining these five with the eight events previously referred to gives the best estimate of the lifetime.

§ 4. DISCUSSION

Because this experiment demands a long distance of flight for unstable particles, it has a strong bias against detecting particles with lifetimes less than 5×10^{-9} sec. A small contamination of short-lived particles in the sample could not be detected by timing measurements, due to poor statistics, and probably would not be identified from the cloud chamber pictures.

The lifetime deduced is consistent with the order of magnitude estimates obtained by other cloud chamber workers. The result is not inconsistent with the conclusion of Keuffel and Mezzetti (1954) that the lifetime they measure precisely (8.7×10^{-9} sec) is that of the K_{μ} -particle.

A notable observation of the experiment is that no timing observation on an S-event has yielded a lifetime longer than 40×10^{-9} sec. This implies that if there are heavy unstable particles with mean lifetimes in the range 10^{-7} to 10^{-6} sec they are not very numerous, since decaying particles with lifetimes in this range would be observed efficiently.

ACKNOWLEDGMENTS

The authors wish to thank Professor P. M. S. Blackett and Dr. G. D. Rochester for their support and encouragement of this experiment. They wish to thank Dr. J. Rösch for his hospitality at the Pic-du-Midi Observatory.

One of us (P. R. B.) is indebted to the United States Educational Commission in the United Kingdom for financial support.

Two of us (R. J. R. and J. S.) are indebted to the Department of Scientific and Industrial Research for maintenance grants during the course of this work.

REFERENCES

- MEZZETTI, L., and KEUFFEL, J. W., 1954, *Phys. Rev.*, **95**, 858.
ROCHESTER, G. D., and BUTLER, C. C., 1953, *Reports on Progress in Physics* (London: Physical Society), p. 364.

XXXVI. *Second-Order Radiative Corrections to the Magnetic Moment of a Bound Electron*

By E. H. LIEB

Mathematical Physics Department, The University, Birmingham*

[Received December 1, 1954]

ABSTRACT

Radiative corrections to the magnetic moment of an outer electron in alkali and hydrogenic atoms due to the atomic electrostatic field have been calculated to second order. The correction is found to be

$$\frac{\Delta\mu}{\mu} = \frac{26}{15\pi} \alpha \frac{\langle V \rangle}{mc^2}$$

where $\langle V \rangle$ is the expectation value of the electron's potential energy. For hydrogen this is $\Delta\mu/\mu = 2.2 \times 10^{-7} \simeq -(2/\pi)\alpha^3$ and will be of importance in the evaluation of future experiments of improved accuracy. For the alkalis, however, the effect is too small to account for the observed Z -dependence of the magnetic moment.

§ 1. INTRODUCTION

ONE of the most fruitful methods for checking quantum electrodynamics against experiment has been the measurement of the magnetic moment of the electron. The recent experimental achievements (Koenig, Prodell and Kusch 1952, Beringer and Heald 1954) in demonstrating the fourth order correction to the magnetic moment of a free electron as calculated by Karplus and Kroll (1950) appear to confirm, in one respect at least, the verity of quantum electrodynamics. However, experiments (Franken and Koenig† 1952) on the magnetic moments of the alkalis reveal a discrepancy between the moment of a free electron and the corrected apparent moment of a bound electron. Although estimates of the effects of interconfigurational mixing (Phillips 1952) have suggested a possible source for the discrepancy, the uncertain nature of the results made it seem worthwhile to calculate the radiative corrections to the electron moment due to the atomic electric field. Such a calculation resembles closely that done by Kroll and Pollock (1952) on the effect of the Coulomb field of a hydrogen like atom on the splitting of hyperfine levels.

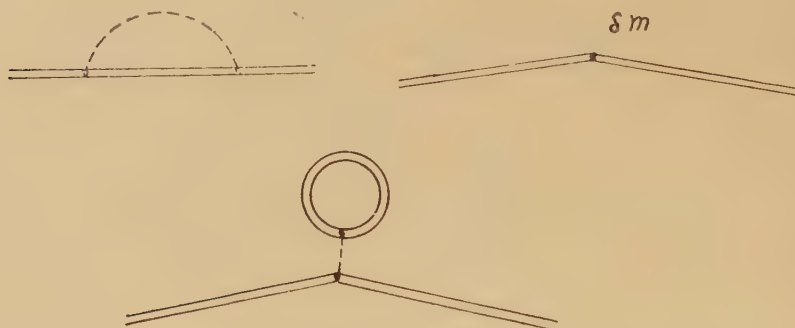
* Communicated by Professor R. E. Peierls.

† See reference for a summary of experimental results to date and for a discussion of corrections to the measurement of moments in alkalis.

Since the problems of radiative corrections to the magnetic moment and to hyperfine splitting differ only in the form of the external potential, the method employed by Kroll and Pollock (1952) in arranging their calculation may be copied here. The notation of Kroll and Pollock will be retained and the reader is referred to that paper for details.

§ 2. THE RADIATIVE CORRECTION

In terms of Feynman diagrams, the radiative corrections to be calculated are as in the figure.



Feynman diagrams for the second order radiative corrections to a bound electron. Double lines represent bound states.

The external potential to be considered is

$$A_{\mu}^e(\mathbf{r}) = iV(|\mathbf{r}|)\delta_{\mu 4} - Hy\delta_{\mu 1} \quad . \quad . \quad . \quad (1)^*$$

where $V(|\mathbf{r}|)$ is the average isotropic electrostatic potential of the alkali atom excluding the outer electron, and $-Hy\delta_{\mu 1}$ is the non-symmetric form of the vector potential of a uniform magnetic field, H , in the z -direction. Thus, taking the Fourier transform

$$\frac{e}{\hbar c} A_{\mu}^e(\mathbf{q}) = iV(|\mathbf{q}|)\delta_{\mu 4} - \frac{ie}{\hbar c} H\delta(q_x)\delta'(q_y)\delta(q_z)\delta_{\mu 1} \quad . \quad . \quad . \quad (2)^{\dagger}$$

where $\delta(x)$ is the ordinary Dirac δ -function and $\delta'(x)$ is its derivative, i.e. $\int \delta'(x)f(x)dx = -(df/dx)_0$.

The simplest integral, and one which will illustrate the main points in the evaluation of all other integrals, is the first one considered by Kroll

* Boldface type will denote 3-dimensional vectors while ordinary type will denote four vectors. $p^2 = p_1^2 + p_2^2 + p_3^2 + p_4^2$.

† $V(|\mathbf{q}|)$ is the Fourier transform of $V(|\mathbf{r}|)$. It is trivially true that a function which depends only on $|\mathbf{r}|$ has a Fourier transform depending only on $|\mathbf{q}|$.

and Pollock (cf. Kroll and Pollock, p. 882). It arises from the polarization energy

$$\Delta E'_p = 2\hbar c \alpha (2\pi)^2 \int \bar{\phi}(\mathbf{p}_2) G(\mathbf{p}_1, \mathbf{p}_2) \phi(\mathbf{p}_1) d\mathbf{p}_1 d\mathbf{p}_2 \quad (3)$$

where

$$G(\mathbf{p}_1, \mathbf{p}_2) = \left(\frac{ie}{\hbar c}\right)^2 \int_0^1 dv \, 2v^2 (1 - \frac{1}{3}v^2) \int d\mathbf{q} \times \frac{\gamma \cdot A^e(\mathbf{p}_2 - \mathbf{p}_1 - \mathbf{q}) [i\gamma \cdot (\mathbf{p}_1 + \mathbf{q}) - \kappa] \gamma \cdot A^e(\mathbf{q})}{4\kappa^2 + q^2(1 - v^2)} \quad (4)$$

Now, by observing that $\phi(\mathbf{p})$ is large only for small values of $|\mathbf{p}|$, Kroll and Pollock argue that a sufficiently accurate answer will be obtained merely by evaluating $G(0,0)$ instead of the full $G(\mathbf{p}_1, \mathbf{p}_2)$. However, it is easy to see that for the case considered here $G(0,0) = \infty$ because one of the A^e in the integrand must be a δ -function while the other must be $1/q^2$. Thus we must calculate $G(\mathbf{p}_1, \mathbf{p}_2)$ near the origin. Nevertheless we can replace p in the bracketed expression by $\bar{p} = (0, 0, 0, i\kappa)$, in which case $G(\mathbf{p}_1, \mathbf{p}_2)$ becomes a function of only $\mathbf{p}_2 - \mathbf{p}_1$. Using the notation $\mathbf{p}_2 - \mathbf{p}_1 = \mathbf{p}$; $\mathbf{p} - \mathbf{q} = \mathbf{D}$ we obtain

$$G(\mathbf{p}) = \left(\frac{ie}{\hbar c}\right)^2 \int_0^1 dv \, 2v^2 (1 - \frac{1}{3}v^2) \int d\mathbf{q} \frac{\gamma \cdot A(\mathbf{D}) [i\boldsymbol{\gamma} \cdot \mathbf{q} - \kappa(1 + \gamma_4)] \gamma \cdot A(\mathbf{q})}{4\kappa^2 + q^2(1 - v^2)} \quad (5)$$

Considering only terms linear in H , we have

$$i\gamma \cdot A(\mathbf{D}) \boldsymbol{\gamma} \cdot \mathbf{q} \gamma \cdot A(\mathbf{q}) = i\gamma_4 \{ A_4(\mathbf{D}) [\mathbf{q} \cdot A(\mathbf{q}) + i\boldsymbol{\sigma} \cdot \mathbf{q} \times \mathbf{A}(\mathbf{q})] + A_4(\mathbf{q}) [\mathbf{q} \cdot \mathbf{A}(\mathbf{D}) - i\boldsymbol{\sigma} \cdot \mathbf{q} \times \mathbf{A}(\mathbf{D})] \} \quad (6)$$

Neglecting for the moment the term in $\gamma \cdot A(\mathbf{D})(1 + \gamma_4)\gamma \cdot A(\mathbf{q})$ and letting $\mathcal{D}(\mathbf{q}) = \delta(q_x)\delta'(q_y)\delta(q_z)$ we obtain

$$G(\mathbf{p}) = \left(\frac{ie}{\hbar c}\right)^2 \gamma_4 H \int_0^1 dv \, 2v^3 (1 - \frac{1}{3}v^2) \int d\mathbf{q} \times \left\{ \frac{V(|\mathbf{p} - \mathbf{q}|) [iq_x \mathcal{D}(\mathbf{q}) - \boldsymbol{\sigma} \cdot (0, q_z \mathcal{D}(\mathbf{q})), -q_y \mathcal{D}(\mathbf{q})]}{4\kappa^2 + q^2(1 - v^2)} + \frac{V(|\mathbf{q}|) [iq_x \mathcal{D}(\mathbf{D}) + \boldsymbol{\sigma} \cdot (0, q_z \mathcal{D}(\mathbf{D})), -q_y \mathcal{D}(\mathbf{D})]}{4\kappa^2 + q^2(1 - v^2)} \right\} \quad (7)$$

Observing that the choice of H in the z -direction was arbitrary, we get

$$G(\mathbf{p}) = -\frac{2}{15} \left(\frac{ie}{\hbar c}\right)^2 \gamma_4 \boldsymbol{\sigma} \cdot \mathbf{H} V(|\mathbf{p}|) \frac{1}{\kappa^2} \left\{ 1 + \text{terms in } \frac{p_y^2}{p^2}, \frac{p_y p_z}{p^2}, \frac{p_y}{\kappa} \right\} \quad (8)$$

to lowest order in $\kappa^2 \mathbf{p}^2$. The succeeding integrals, all of which are similar to this one, will also contain terms in p_y^2 and $p_y p_z$. It is clear that these terms must cancel because they single out directions in the x - y plane whereas we know the physical problem to be isotropic in the x - y plane. Similarly, it will be seen that the term in $\gamma \cdot A(\mathbf{D})(1 + \gamma_4)\gamma \cdot A(\mathbf{q})$ will give rise only to terms proportional to p_y/κ and hence they too must vanish. Of course the terms in question involve γ -matrices and hence factors in \hat{p}_x , but no combination of them can give isotropic terms.

Thus, if μ is the electron moment, we have

$$\left(\frac{\Delta\mu}{\mu}\right)_{p'} = -\frac{\partial \Delta E_{p'}}{\partial H} \Big/ \frac{e\hbar}{2mc} \sigma = -\frac{4}{15\pi} \alpha \langle V \rangle \quad . \quad . \quad . \quad (9)$$

where $\langle V \rangle$ is the expectation value of the potential energy of the electron. This result follows at once from the observation that if $V(\mathbf{p})$ is the Fourier transform of $V(\mathbf{r})$ then

$$\int \bar{\phi}(\mathbf{p}_2) e V(\mathbf{p}_2 - \mathbf{p}_1) \phi(\mathbf{p}_1) d\mathbf{p}_1 d\mathbf{p}_2 = (1/2\pi)^3 \langle V \rangle. \quad (10)$$

Similar results hold for the rest of the integrals, the remainder of the calculation being briefly outlined in the appendix. In all cases one gets $G(\mathbf{p}) \sim V(\mathbf{p})$ which according to (10) implies $\Delta\mu \sim \langle V \rangle$.

§ 3. RESULTS AND DISCUSSION

Thus, to second order the radiative correction to the magnetic moment of a valence electron in an alkali atom is*

$$\frac{\Delta\mu}{\mu} = \frac{26}{15\pi} \alpha \frac{\langle V \rangle}{mc^2} \quad . \quad . \quad . \quad . \quad . \quad (11)$$

For hydrogen this becomes

$$\left(\frac{\Delta\mu}{\mu}\right)_H = -\frac{26}{15\pi} \alpha^3 = -2.2 \times 10^{-7} \quad (\text{for hydrogen}), \quad . \quad . \quad (12)$$

As regards the alkalis, a sufficiently accurate answer is obtained by using the approximate formula of Lamb (1941), $\langle V \rangle = W_0 - 3W$ where W is the ionization potential and W_0 is the ionization potential of a hydrogen atom in the corresponding n -state. It is then found that

$$\frac{\Delta\mu}{\mu} \simeq \frac{1}{2} \left(\frac{\Delta\mu}{\mu}\right)_H \quad (\text{all alkalis}). \quad . \quad . \quad . \quad . \quad . \quad (13)$$

This result is too small to account for the observed dependence upon atomic number of the electron moment in alkalis. Moreover, it would be rather difficult to observe in alkalis because the corrections due to relativistic effects, inter-configurational mixing and internal diamagnetism, all of which are much larger, and which must themselves account for the discrepancy, cannot be conveniently estimated with sufficient accuracy.

The situation is completely different for hydrogen where the aforementioned corrections either vanish or are known with great accuracy. Nevertheless there is still an effect which has not yet been calculated, namely the sixth order correction to the moment of a free electron—an extremely lengthy calculation. However, it is not unlikely that its magnitude is less than the effect calculated here, and consequently a crude estimate, if such could be found, would enable the bound state correction to be observed experimentally.

To measure the electron moment two facts are needed, namely the ratio of the proton moment to the bound electron moment, and the ratio of the proton moment to the Bohr magneton. The first is almost known

* cf. the Appendix to this paper.

to sufficient accuracy (Beringer and Heald 1954), an improvement of four times in accuracy being sufficient. The second (Gardner 1951) however requires an improvement of 10^2 .

It is probable that the next few years will see a decided improvement in the experimental data, in which case the effect discussed here will have to be included in a discussion of the results.

ACKNOWLEDGEMENTS

The author wishes to acknowledge his indebtedness to Dr. S. F. Edwards for his patience as a teacher, to Dr. G. E. Brown for suggesting the problem, and to Professor R. E. Peierls for his encouragement and stimulation. He would also like to acknowledge a grant from the National Science Foundation, U.S.A.

APPENDIX

Remainder of the Calculation

The next term to be considered is eqn. (43) of Kroll and Pollock. Although for hyperfine splitting this contribution to the fluctuation energy vanishes, it is not so here. The procedure is the same as for the polarization energy

$$\left. \begin{aligned} \Delta E_F^{(1)} &= -6\pi^2 \hbar c \alpha \int \bar{\phi}(\mathbf{p}_2) G_F^{(1)}(\mathbf{p}_1, \mathbf{p}_2) \phi(\mathbf{p}_1) d\mathbf{p}_1 d\mathbf{p}_2, \\ G_F^{(1)}(\mathbf{p}_1, \mathbf{p}_2) &\simeq G_F^{(1)}(\mathbf{p}) \\ &= \left(\frac{ie}{\hbar c}\right)^2 \int_0^1 dv \int d\mathbf{q} \gamma \cdot A(\mathbf{D}) \frac{2vi \boldsymbol{\gamma} \cdot \mathbf{q} + \kappa(1-2v-2v\gamma_4)}{\kappa^2 - q^2 v^2} \gamma \cdot A(\mathbf{q}). \end{aligned} \right\} \quad (\text{A.1})$$

Therefore, discarding non-isotropic terms and considering only the lowest order in p^2 ,

$$\left(\frac{\Delta\mu}{\mu}\right)_{F^{(1)}} = \frac{3}{\pi} \alpha \frac{\langle V \rangle}{mc^2}. \quad \dots \dots \dots (\text{A.2})$$

We come now to the first term of eqn. (36)

$$\left. \begin{aligned} \Delta E_F^{(1)} &= 2\pi^2 \hbar c \alpha \int \bar{\phi}(\mathbf{p}_2) G_F^{(2)}(\mathbf{p}_1, \mathbf{p}_2) \phi(\mathbf{p}_1) d\mathbf{p}_1 d\mathbf{p}_2, \\ G_F^{(2)}(\mathbf{p}_1, \mathbf{p}_2) &= \left(\frac{ie}{\hbar c}\right)^2 A_\mu^e(\mathbf{p}_2 - \mathbf{p}_1) K_\mu(p_2, p_1), \end{aligned} \right\} \quad \dots \dots (\text{A.3})$$

where $K_\mu(p_2, p_1)$ is displayed in eqn. (33). The second term in $K_\mu(p_2, p_1)$ may be split into two parts as done by Kroll and Pollock. The first part gives the anomalous moment of Schwinger while the second may be shown to vanish. The other terms in $K_\mu(p_2, p_1)$ may be expanded using eqn. (23) and after some manipulation one can show that

$$\left(\frac{\Delta\mu}{\mu}\right)_{F^{(2)}} = -\frac{\alpha}{\pi} \frac{\langle V \rangle}{mc^2}. \quad \dots \dots \dots (\text{A.4})$$

It should be pointed out that in obtaining this result a term involving $(A_\mu^e)^3$ was dropped. This is certainly justified because the momentum is small compared to the rest mass.

We now come to the second order parts, L_D and Q . The justification in Kroll and Pollock for using only the first approximation for S_F^e involves the nature of the magnetic potential. Such an argument fails in the case of a δ -function, but we can ignore higher order terms in S_F^e on the grounds that terms in $(A_\mu^e)^3$ make only small contributions. It can then be shown that L_D vanishes because of the symmetry properties of the integrand.

Finally we must evaluate Q .

$$\left. \begin{aligned} Q &= 2i\hbar c \alpha \int \bar{\phi}(\mathbf{p}_2) G_Q(\mathbf{p}) \phi(\mathbf{p}_1) d\mathbf{p}_1 d\mathbf{p}_2, \\ G_Q(\mathbf{p}) &= \left(\frac{ie}{\hbar c}\right)^2 \int \frac{d^4 k}{k^2} \mathcal{A}_\mu'(\mathbf{D}, \bar{p}, k) \frac{i\gamma \cdot (\bar{p} + q - k) - \kappa}{k^2 - 2(p+q) \cdot k + q^2} \mathcal{A}_\mu(\mathbf{q}, \bar{p}, k) d\mathbf{q} \\ &= \left(\frac{ie}{\hbar c}\right)^2 \langle \text{I} + \text{II} + \text{III} \rangle, \end{aligned} \right\} \quad (\text{A.5})$$

where I, II, III are the integrals indicated on p. 886 of Kroll and Pollock with $A^e(-\mathbf{q})$ replaced by $A^e(\mathbf{D})$. As it turns out, there is no need for an infra-red cut-off in these integrals because they converge independently. After a considerable amount of manipulation, one can show that

$$\langle \text{I} + \text{II} + \text{III} \rangle = 8V(|\mathbf{p}|)\sigma \cdot H \int d_4 k \frac{k_1^2 + k_4^2}{k^2(k^2 + 2i\kappa k_4)^3} = 0.$$

Thus $Q=0$ and on adding up all the terms we arrive at the final answer

$$\frac{\Delta\mu}{\mu} = \frac{26}{15\pi} \alpha \frac{\langle V \rangle}{me^2}.$$

REFERENCES

- BERINGER, R., and HEALD, M. A., 1954, *Phys. Rev.*, **95**, 1494.
 FRANKEN, P., and KOENIG, S. H., 1952, *Phys. Rev.*, **88**, 199.
 GARDNER, J. H., 1951, *Phys. Rev.*, **83**, 996.
 KARPLUS, R., and KROLL, N., 1950, *Phys. Rev.*, **77**, 536.
 KOENIG, S. H., PRODELL, A. G., and KUSCH, P., 1952, *Phys. Rev.*, **88**, 191.
 KROLL, N., and POLLOCK, F., 1952, *Phys. Rev.*, **86**, 876.
 LAMB, W. E., Jr., 1941, *Phys. Rev.*, **60**, 817.
 PHILLIPS, M., 1952, *Phys. Rev.*, **88**, 202.

XXXVII. *An Exact Solution of the Spherical Blast Wave Problem*

By J. LOCKWOOD TAYLOR

Norges Tekniske Høgskole, Trondheim, Norway*

[Revised MS. received September 7, 1954]

VARIOUS authors have investigated the problem of an explosion wave in air, assumed to start at a point, during the stage when the spherical shock wave is still strong, and some numerical results and at least one approximate analytical solution are known, but the present is, so far as is known, the first exact mathematical solution to be published. It is obtained by straightforward deduction from the known general equations of motion.

The equations of motion can be written

$$\frac{1}{x^2} \frac{\partial(\rho u x^2)}{\partial x} + \frac{\partial \rho}{\partial t} = 0, \quad (1)$$

$$\rho \left(u \frac{\partial u}{\partial x} + \frac{\partial u}{\partial t} \right) + \frac{\partial p}{\partial x} = 0, \quad (2)$$

$$\frac{1}{p} \left(\frac{\partial p}{\partial t} + u \frac{\partial p}{\partial x} \right) = \frac{\gamma}{\rho} \left(\frac{\partial \rho}{\partial t} + u \frac{\partial \rho}{\partial x} \right), \quad (3)$$

expressing respectively (1) continuity of flow, (2) radial force=rate of change of momentum, (3) adiabatic pressure-density relation for a particle. By combining these three equations, or otherwise, we get the known energy relation

$$\frac{\partial E}{\partial t} + \frac{1}{x^2} \frac{\partial}{\partial x} (x^2 u I) = 0. \quad (4)$$

The solution we are concerned with is of the form

$$\rho = f_1(x/t^{2/5}), \quad (5)$$

$$u = t^{-3/5} f_2(x/t^{2/5}), \quad (6)$$

$$p = t^{-6/5} f_3(x/t^{2/5}), \quad (7)$$

with $R = kt^{2/5}$ defining the shock radius at time t .

Thus the shock velocity $U = \frac{dR}{dt} = \frac{2}{5} kt^{-3/5}$.

It can be seen that (5), (6) and (7) make both the kinetic energy

$$4\pi \int_0^R \frac{1}{2} \rho u^2 x^2 dx$$

and the internal or intrinsic energy

$$\frac{4\pi}{\gamma-1} \int_0^R p x^2 dx$$

within the sphere constant at all times, also satisfying the shock† conditions

$$\rho_s = \text{constant}, \quad p_s \propto u_s^2.$$

* Communicated by the Author.

† See Appendix.

The specified dependence on t makes the problem in effect one of a single independent variable (x). Thus

$$\frac{\partial \rho}{\partial t} = -\frac{2}{5} \frac{x}{t} \frac{\partial \rho}{\partial x} = -\frac{x}{R} U \frac{\partial \rho}{\partial x},$$

$$\frac{\partial p}{\partial t} = -\frac{2}{5} \frac{x}{t} \frac{\partial p}{\partial x} - \frac{6}{5} \frac{p}{t} = -\frac{x}{R} U \frac{\partial p}{\partial x} - 3 \frac{U}{R} p.$$

Equation (4) together with the relation

$$\frac{\partial E}{\partial t} + \frac{6}{5} \frac{E}{t} + \frac{2}{5} \frac{x}{t} \frac{\partial E}{\partial x} = 0 \quad \dots \quad (8)$$

immediately following from the form $E = t^{-6/5} f(x, t^{2/5})$, gives

$$x^2 u I = \frac{2}{5} x^3 E / t \quad \dots \quad (9)$$

or

$$\frac{u}{U} = \frac{x}{R} \frac{E}{I} \quad \dots \quad (10)$$

which we rewrite as

$$u' = x' \left\{ \frac{\frac{1}{2} u^2 + \frac{p}{(\gamma-1)\rho}}{\frac{1}{2} u^2 + \frac{\gamma p}{(\gamma-1)\rho}} \right\} \quad \dots \quad (11)$$

Solving,

$$\frac{p}{\rho} = \frac{\gamma-1}{2} u^2 \frac{x'-u'}{\gamma u' - x'} = C_1 u'^2 \frac{(x'-u')}{\gamma u' - x'} \quad \dots \quad (12)$$

Combining (1) and (3) we get

$$\frac{1}{p} \frac{\partial p}{\partial x} - \frac{\gamma-1}{\rho} \frac{\partial \rho}{\partial x} = -\frac{1}{u p} \frac{\partial p}{\partial t} + \frac{\gamma-1}{u \rho} \frac{\partial \rho}{\partial t} - \frac{1}{u} \frac{\partial u}{\partial x} - \frac{2}{x} \quad \dots \quad (13)$$

On substituting for $\partial p / \partial t$ and $\partial \rho / \partial t$ and dropping the partial differentiation notation

$$\left(\frac{x}{R} - \frac{u}{U} \right) \left(\frac{1}{p} \frac{dp}{dx} - \frac{\gamma-1}{\rho} \frac{d\rho}{dx} \right) = -\frac{3}{R} + \frac{1}{U} \frac{du}{dx} + \frac{2}{x} \frac{u}{U} \quad \dots \quad (14)$$

or

$$\frac{1}{p} \frac{dp}{dx} - \frac{\gamma-1}{\rho} \frac{d\rho}{dx} = -\frac{2}{x} - \left[\frac{\frac{1}{R} - \frac{1}{U} \frac{du}{dx}}{x/R - u/U} \right] \quad \dots \quad (15)$$

Integration gives

$$\frac{p}{\rho^{\gamma-1}} = C_2 (x' - u')^{-1} x'^{-2} \quad \dots \quad (16)$$

By alternately eliminating p , ρ from (12) and (16) we get

$$p = C_3 [x u (x - u)]^{-2/(2-\gamma)} (\gamma u - x)^{1/(2-\gamma)} \quad \dots \quad (17)$$

$$p = C_4 x^{-2/(2-\gamma)} u^{2(1-\gamma)/(2-\gamma)} (x - u)^{-\gamma/(2-\gamma)} (\gamma u - x)^{(\gamma-1)/(2-\gamma)} \quad \dots \quad (18)$$

where x , u are now conveniently written for x' , u' (equivalent to taking, for the present $U=1$, $R=1$ which does not involve any loss of generality).

Differentiating $\log \rho$ from (17) with respect to x and equating to

$$\frac{1}{\rho} \frac{d\rho}{dx} = \frac{1}{(x-u)} \left(\frac{du}{dx} + \frac{2u}{x} \right) \quad . \quad . \quad . \quad . \quad . \quad (19)$$

as can be deduced from the equation of continuity (1), gives a differential equation for u in terms of x which need not be written out, but whose solution is

$$2 \log u = a \log x + b \log \left(x - \frac{3\gamma-1}{5} u \right) + h \log (\gamma u - x) + \log C \quad (20)$$

where

$$\begin{aligned} a &= \frac{-10(\gamma-1)}{(3\gamma-1)}, \\ b &= (-13\gamma^2 + 7\gamma - 12)/(3\gamma-1)(2\gamma+1), \\ h &= 5 \left(\frac{\gamma-1}{2\gamma+1} \right). \end{aligned}$$

The result (20) together with (17) and (18) express u , p , ρ in terms of x and therefore give the required solution. The constants C , C_3 , C_4 are to be found by substituting the known values of the variables at the shock (x or $x'=1$, u or $u'=2/(\gamma+1)$).

The exact solution as described allows for instance the accurate calculation of the value p/p_s at the centre of the sphere, otherwise difficult to obtain precisely. The calculated value is 0.303 for $\gamma=5/3$ and 0.365 for $\gamma=1.4$, as compared with Kynch's value of 0.31 for $\gamma=5/3$ and Sir Geoffrey Taylor's of 0.374 for $\gamma=1.4$.

Symbols

x =distance from centre of sphere.

ρ =air density.

u =air velocity (radially outwards).

p =air pressure.

t =time from explosion.

γ =ratio of specific heats.

R =shock radius= $kt^{2/5}$.

Suffix s denotes shock. Suffix 0 denotes free-air.

E/ρ =total energy of air per unit mass = $\left\{ \frac{1}{2} u^2 + \frac{p}{(\gamma-1)\rho} \right\}$.

I/ρ =total heat of air per unit mass = $\left\{ \frac{1}{2} u^2 + \frac{\gamma p}{(\gamma-1)\rho} \right\}$.

U =shock velocity = $\frac{2}{5} kt^{-3/5} = \frac{2}{5} \frac{R}{t}$.

$x'=x/R$, $u'=u/U$.

M =Mach No. = U/c_0 , $c_0 = \sqrt{\frac{\gamma p_0}{\rho_0}}$ = free-air velocity of sound.

$C, C_1, C_2, C_3, C_4, k, a, b, h$, constants.

The values of C_1, C_2, C_3, C_4 , got by substituting for the known pressure density and velocity at the shock are :

$$C_1 = \frac{\gamma-1}{2} U^2,$$

$$C_2 = 2\rho_0^{2-\gamma} \{(\gamma-1)/(\gamma+1)^{\gamma+1}\} U^2,$$

$$C_3 = 2^{2/2-\gamma} \rho_0 (\gamma+1)^{-(\gamma+1)/(2-\gamma)} (\gamma-1)^{(\gamma-1)/(2-\gamma)},$$

$$C_4 = 2^{\gamma/2-\gamma} \rho_0 (\gamma+1)^{-(\gamma+1)/(2-\gamma)} (\gamma-1)^{1/(2-\gamma)} U^2.$$

APPENDIX

Conditions at Shock

When the shock is sufficiently strong, the usual shock equations give :

$$M_s = \sqrt{\frac{\gamma-1}{2\gamma}} = (U-u_s)/c_s, \quad c_s = \sqrt{\gamma p_s/\rho_s},$$

$$\rho_s = \rho_0 \left(\frac{\gamma+1}{\gamma-1} \right),$$

$$u_s = U - \left(\frac{\gamma-1}{\gamma+1} \right) U = \frac{2}{\gamma+1} U,$$

$$p_s = \frac{2\gamma}{\gamma+1} p_0 M^2 = \frac{2}{\gamma+1} \rho_0 U^2.$$

Numerical Values for $\gamma=1.4$

x/R	0	0.6	0.8	0.9	0.95	1.0
u/U	0	0.429	0.584	0.685	0.7513	0.8333
p/p_s	0.365	0.366	0.4035	0.510	0.651	1.0
ρ/ρ_s	0	0.00675	0.0654	0.2056	0.4106	1.0

REFERENCES

- KYNCH, G. J., 1953, *Modern Developments in Fluid Dynamics*, Vol. I (Oxford : Clarendon Press).
 TAYLOR, Sir G., 1950, *Proc. Roy. Soc. A*, **201**, 159.

XXXVIII. *The Measurement of Photoneutron Yields with a Sodium Iodide Crystal*

By K. G. McNEILL

Department of Natural Philosophy, The University, Glasgow †

[Received December 8, 1954]

ABSTRACT

It is shown that a NaI (Tl) crystal will act as a detector of photoneutrons by virtue of the production of radioactive ^{128}I within the crystal. This detecting technique has been applied to the comparison of the photoneutron yields obtained from copper, cadmium, mercury and lead when these elements are irradiated with a bremsstrahlung x-ray beam of maximum energy of 22 mev. The yields from these four elements are found to be in the ratios Cu : Cd : Hg : Pb as 1 : 4.1 : 9.5 : 8.4.

§ 1. INTRODUCTION

THE importance of photodisintegration has given rise to the development of many different techniques for investigating this process. When the source of x-rays is a pulsed machine such as a beta- or synchro-tron, the instantaneous high intensity of the x-ray flux militates against the immediate detection of the product particles. As a result, most of the work in this field has been done using techniques in which the measurements are taken after the end of the beam pulse. An example of such a technique is that based on the production of radioactive isotopes (Johns, Katz, Douglas and Haslam 1950). A more recent method (Halpern, Nathans and Mann 1952) uses the fact that thermal neutrons have on the average a free life of a few milliseconds before capture by nuclei, and that therefore the photoneutrons, after slowing down in some moderator, may be detected by conventional methods at a time much later than the end of the x-ray pulse.

In a previous note (Reid and McNeill 1953) it was observed that a background activity was induced in a NaI (Tl) crystal which was being used to detect x-rays associated with the $^{208}\text{Pb}(\gamma n)^{207*}\text{Pb}$ reaction. A study of this activity has now shown that it is caused by the interaction of fast photoneutrons with the iodine of the crystal. This interaction produces ^{128}I , which decays by β emission with a half-life of 25 minutes. As this activity is actually produced within the crystal, the detection efficiency for the resulting β -rays is nearly 100%, and the NaI crystal may therefore be used as a reasonably efficient fast neutron detector.

† Communicated by the Author.

The present paper describes some measurements of relative cross sections for the (γn) process in different elements, using this fast neutron detection technique. In principle this technique resembles those previously quoted in that the measurements are of the integrated effects of the beam pulse and are carried out well after the end of the beam pulse. However, as the NaI crystal is activated by fast neutrons, the photoneutrons do not need to be thermalized prior to detection.

§ 2. PRELIMINARY EXPERIMENTS

During the initial experiments, different targets were bombarded by a bremsstrahlung x-ray beam of maximum energy 22 mev. A 1.0 inch cube NaI crystal, mounted on an EMI 5311 photomultiplier, was placed under the targets, but outside of the collimated beam. The radioactivity produced in a standard copper foil was in all cases used as a beam intensity monitor. With all the targets used, a radioactivity was induced in the NaI crystal, and the half-life of this activity was found to be independent of the target material. The average of all results gave the half-life as 25.4 ± 0.2 minutes. Moreover, it was found that for a given target the strength of the induced activity was proportional to the x-ray beam intensity. These facts show that the activity is due to ^{128}I produced by the reaction $^{127}\text{I} (n\gamma) ^{128}\text{I}$, and, therefore, that the intensity of the activity may be used as a measure of the neutron flux through the crystal.

A considerable activity was induced in the NaI crystal when there was no target in the beam. This was considered to be due to photoneutrons produced at the internal target and do-nut walls of the synchrotron, and at the walls of the beam room. To reduce this beam background the detecting system was screened by placing it within a large cubical paraffin box. The box had an external dimension of 78 cm, and had inside it a chamber lined with cadmium and iron. Inside this cavity were placed the various targets and the crystal, photomultiplier, and head amplifier. The centre of the detection cavity was 122 cm from the target of the synchrotron. Slots were cut in the box so that the x-ray beam could pass through it.

This screening arrangement was used in all the work subsequently described.

§ 3. ENERGY OF THE PHOTONEUTRONS

Some knowledge of the energy of the neutrons reacting with the iodine nuclei is essential for the comparison of neutron yields from different targets. As the $(n\gamma)$ cross section in iodine has been measured and found to be markedly dependent on neutron energy, the absolute determination of this cross section in a particular experiment would enable the energy of the incident neutrons to be found. Photoneutrons are known to be emitted with a whole spectrum of energies, and therefore in the case of photoemission the experimental determination of the $(n\gamma)$ cross section will lead to a mean cross section defined by $\int N_{\epsilon} \sigma_{\epsilon} d\epsilon / \int N_{\epsilon} d\epsilon$, where N_{ϵ} are the numbers of,

and σ_ϵ the $(n\gamma)$ cross sections for, neutrons of energy ϵ , the integral being taken over all available neutron energies. To this mean cross section will correspond a mean interaction neutron energy.

To determine this cross section it is necessary to bombard the NaI crystal with a known flux of neutrons. As the 22 mev Cu (γn) yield is well established (Byerley and Stephens 1951), this known flux was produced by irradiating with the x-ray beam a copper target placed at a known distance above the crystal. The absolute strength of the beam was measured with a Victoreen meter, and the copper monitor activity normally used for measuring the beam intensity was calibrated in terms of this Victoreen meter (Wright 1954).

In a typical experiment, after 15 minutes irradiation of the copper target, the beam was switched off and the decay of the induced activity followed for 30 minutes, readings being taken every 5 minutes. The rate of decay at switch-off was determined using the measured half-life of ^{128}I , and thus the rate of production of ^{128}I found. The average of many runs was taken, and allowance was made for the fact that with only 15 minutes irradiation the iodine activity would not be saturated. A fuller discussion of the experimental technique is given in §4. From the rate of production of ^{128}I , the known flux of neutrons, and the knowledge of the number of iodine nuclei present in the NaI crystal, the cross section of the ^{127}I $(n\gamma)$ ^{128}I reaction was calculated.

This cross section was found to be $1.6 \pm 0.5 \times 10^{-25} \text{ cm}^2$, corresponding to a mean interaction energy of $0.9^{+0.6}_{-0.3} \text{ mev}$ (*The Science and Engineering of Nuclear Power*, Vol. I, 1947).

Byerley and Stephens (1951) measured the energy distribution of Cu (γn) neutrons, and from their results an average neutron energy of 2.0 mev is indicated. The mean interaction energy will be less than this, as the low energy neutrons will give a disproportionately large yield. An estimate has been made of the mean interaction energy using Byerley and Stephens' results and the known ^{127}I $(n\gamma)$ cross sections, and this gives that the mean interaction energy equals 1.2 mev, in reasonable agreement with the experimental result quoted above.

The fact that resonance neutrons, with their much higher cross section, play no part in the interaction was checked by surrounding the NaI crystal with a layer of iodine during the course of an irradiation, and removing this layer before counting of the induced activity was commenced. The iodine layer was sufficiently thick to absorb 80% of any 40 ev resonance neutrons, and at least 16% of any neutrons below this resonance energy. To within the experimental error of 5%, this iodine layer had no effect, indicating that in fact only fast neutrons were effective in the interaction with the iodine of the crystal.

These facts show that the neutrons reacting in the crystal are coming straight from the target, and have not been thermalized in the paraffin screening prior to capture. Apparently the neutrons have an opportunity of interaction when first they pass through the crystal, but if once they

enter the paraffin, they will be slowed down there and the cadmium sheet will prevent them re-entering the detection chamber.

§ 4. COMPARISON OF PHOTONEUTRON YIELDS

As the neutrons interacting with the iodine of the crystal have come directly from the target without losing energy by collision, the distribution of energies of the photoneutrons for a given maximum x-ray energy will depend only on the shape of the (γn) cross section curve of the target material. If the shapes of this curve for different materials are the same, it is possible to say that the ratio of the induced iodine activity for two materials is equal to the ratio of their (γn) yields, for although the ^{127}I $(n\gamma)$ cross section varies with neutron energy, the relative proportions of neutrons in each energy range will be the same for both materials. Yield curves have been found for many nuclides, and the great majority of these show the same 'giant resonance' shape. In particular Cu and Pb have similar characteristics (Montalbetti, Katz and Goldemberg 1953), and it is reasonable to assume that the other two elements investigated, cadmium and mercury, have the same general characteristics, especially as the multi-isotopic characters of these two elements will smooth out any peculiarity which might be present in any one nuclide.

It is therefore possible to find the ratios of the 22 mev (γn) yields by comparing the iodine activity induced when different targets are irradiated. Experiments were performed to compare the yields of the four elements quoted. In all cases thick targets were required to give adequate yields, the thicknesses being chosen so that equal beam absorption occurred in all targets.

Normally the crystal was left a sufficiently long time between runs so that it was quite inactive before the next run was started. If this was not possible, allowance was made for the residual activity. As in all cases background had to be taken into account, the normal procedure was to subtract 'cosmic' background, then normalize to a standard beam strength using the copper monitor activity, and then to subtract the normalized 'no-target' background. The result was taken as the normalized yield due to the target.

The 'no-target' background was in all cases an appreciable fraction of the total yields. In the case of the copper target, for instance, the 'no-target' yield was almost a third of the total yield obtained with the copper target in position. Higher yields were obtained from the other targets, however, and therefore the 'no-target' yield was relatively less important. The causes of the 'no-target' yield were probably the stray neutrons which can enter the detection chamber via the beam channels, and the (γn) reactions that may take place in the detection chamber screening itself.

The comparative yields obtained from the four target materials are shown in the table in two ways: in column 2 is given the normalized yield from each target, and in column 3 the 22 mev yields per mole are given relative to the yield from copper. The statistical errors are indicated

after each result. For comparison, it may be noted that the 'no-target' yield was 143 counts in the first 30 minutes after switch-off per 1000 Cu monitor counts. This background has, of course, been subtracted from the total 'with-target' yields before inclusion in the table.

Target element	Counts in 30 minutes per 1000 monitor counts	22 mev yield/mol/r relative to copper	Yield/mol/r $\times 10^{-6}$
Cu	288 ± 15	1.0	3.2
Cd	647 ± 28	4.1 ± 0.3	13
Hg	661 ± 26	9.5 ± 0.9	30
Pb	470 ± 17	8.4 ± 0.5	27

§ 5. DISCUSSION

The photoneutron yields of lead and copper have been measured by Montalbetti, Katz and Goldemberg (1953). From their graphs the 22 mev yields of these two elements are seen to be in the ratio of 9 : 1, a figure which is in satisfactory agreement with the present result of 8.4 : 1. In the cases of cadmium and mercury, direct comparison with previous work is not possible as no data on these elements is available.

Photoneutron yields at 22 mev are known for many elements of widely differing atomic mass (Nathans and Halpern 1954, Montalbetti, Katz and Goldemberg 1953), and using these results a graph can be drawn of yield against atomic mass. It is found that a smooth curve may be drawn through the experimental points, and the results of the present investigation may therefore be checked by plotting them on this same graph. Before this is done a photoneutron yield must be assumed for one of the four elements studied, since the present experiment gives only relative yields. The present results for Pb have a smaller statistical error than do those for Cu, the other element for which independent figures are available, and therefore Pb has been taken as the standard. The value of 27×10^6 neutrons/mol/r, taken from the graphs of Montalbetti, Katz and Goldemberg (1953), has been accepted, and using this figure the yields of the other elements were calculated. These values are given in column 4 of the table. When these yields are plotted on a Yield-Atomic Mass graph, as suggested above, it is in fact found that they fit very satisfactorily with the results of other authors.

ACKNOWLEDGMENTS

I should like to thank Professor P. I. Dee, F.R.S., Mr. J. M. Reid and Mr. I. F. Wright for many valuable discussions. I am also indebted to Mr. J. M. Reid for help in the preliminary stages of the experiments.

REFERENCES

- BYERLEY, P. R., and STEPHENS, W. E., 1951, *Phys. Rev.*, **83**, 54.
HALPERN, J., NATHANS, R., and MANN, A. K., 1952, *Phys. Rev.*, **88**, 679.
JOHNS, H. E., KATZ, L., DOUGLAS, R. A., and HASLAM, R. N. H., 1950, *Phys. Rev.*, **80**, 1062.
MONTALBETTI, R., KATZ, L., and GOLDEMBERG, J., 1953, *Phys. Rev.*, **91**, 659.
NATHANS, R., and HALPERN, J., 1954, *Phys. Rev.*, **93**, 437.
REID, J. M., and MCNEILL, K. G., 1953, *Proc. Phys. Soc. A*, **66**, 1179.
THE SCIENCE AND ENGINEERING OF NUCLEAR POWER, 1947, Vol. I (The Addison-Wesley Press Inc.).
WRIGHT, I. F., 1954, private communication.

XXXIX. *Self-Excited Oscillations in an Open Circular Water Tank*

By A. M. BINNIE
Trinity College, Cambridge*

[Received September 3, 1954]

ABSTRACT

When a vertical or inclined nozzle is fixed in an open tank with its outlet flush with the surrounding water, the jet from the nozzle is irregularly disturbed by waves due to the fall of the jet. Small-scale experiments in a circular basin showed that, if the nozzle were properly sited and trained, and supplied at the correct pressure, the water in the basin could be thrown into one of its natural states of stationary oscillation. The jet then pulsated in an almost steady manner that was much more interesting to contemplate than an irregular or monotonously uniform jet. A simple, approximate theory is put forward to explain the maintenance of the self-excited oscillations in the basin.

§ 1. INTRODUCTION

BINNIE AND HOOKINGS (1948) showed that, when water is supplied tangentially to a circular tank and allowed to escape in a whirlpool at the centre of the bottom, the flat free surface in the tank is sometimes disturbed by oscillations. These form a system of waves that travels unchanged round the centre, and they appear to be due to resonance between the natural periods of the water in the tank and of disturbances in the whirlpool. But the nature of the instability of a whirlpool under gravity is obscure, and the arrangement cannot be used to excite a predetermined natural period of the tank. The present paper describes another way of producing self-excited oscillations in a tank. Experiments were carried out at the Engineering Laboratory, Cambridge, with a small nozzle fixed with its outlet level with the surrounding water. It was found that, if the trajectory of the jet were properly arranged, the fall of the jet influenced the submergence of the nozzle in such a way that many of the natural stationary periods of the tank could be excited.

The kinds of free oscillation that are possible in a circular basin must first be examined, and an account of the most important is given in § 2. It seems unlikely that the action of the rising jet on the wave over the nozzle outlet can have any exciting effect. For the relative velocity of the jet and the wave is greater as the crest of the wave subsides than as it rises; hence, if the nozzle is not submerged for the whole of every cycle, the average force on the wave over a cycle opposes the motion.

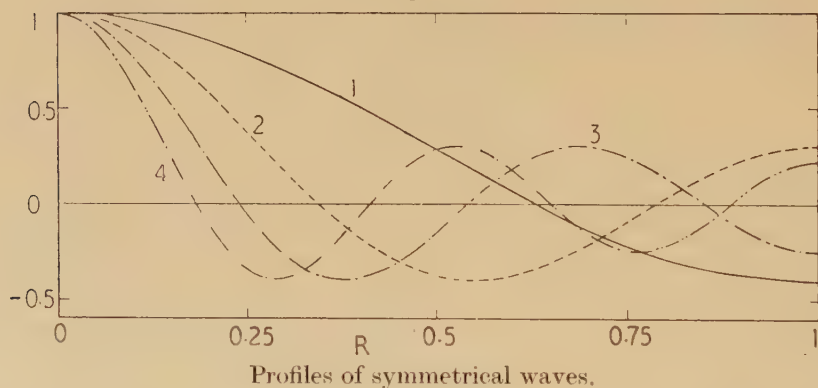
* Communicated by the Author.

An explanation of the oscillations will be sought by investigating the trajectory of the jets, and a simple theory is developed in § 3. The experiments are described in § 4, and when they are analysed, the maintenance of the waves can be accounted for. Presumably they were set going by some chance combination of the random disturbances which were always seen to occur. The work has an application to the design of pulsating fountains, and it was in fact suggested by an examination of the fountain of this type that may be seen at Villeneuve, Switzerland.

§ 2. THE THEORY OF FREE STATIONARY OSCILLATIONS IN A CIRCULAR BASIN

For a circular basin having uniform depth and vertical walls the complete theory of small oscillations was worked out by Rayleigh (1876), a summary of whose analysis was given by Lamb (1932). For motion possessing circular symmetry the waves have annular crests and hollows, and the shapes of the first four modes are displayed in fig. 1, which is

Fig. 1



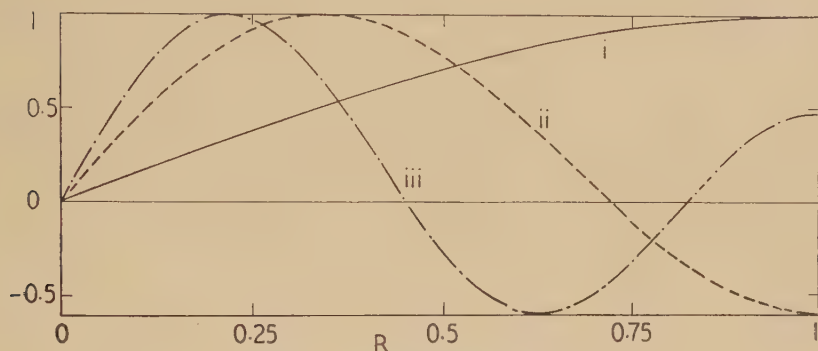
drawn to an arbitrary vertical scale on a base of $R=r/a$, where r is the radius at any point and a is the radius of the basin. The radius and depth of the experimental tank were 18 and 9 in., and for these values the upper part of table 1 shows the periods τ of the waves of fig. 1.

Table 1. Periods of Symmetrical Oscillations and of Asymmetrical Oscillations with one Diametral Node. $g=32.2 \text{ ft./sec}^2$

Symmetrical mode	1	2	3	4
τ sec	0.708	0.513	0.425	0.372
Asymmetrical mode	i	ii	iii	
τ sec	1.173	0.590	0.464	

Experiments were carried out not only on symmetrical oscillations but also on the species for which there are one diametral node and 0, 1, 2, . . . circular nodes. Cross sections of the first three waves, taken through the centre at right angles to the diametral node, are given in fig. 2 and the periods in the lower part of table 1. Only in the fundamental mode (i) was the period appreciably influenced by the depth. In this mode the water sways from side to side in a simple manner. The second mode (ii) is more complicated, and the contoured plan given by Lamb on the lower half of page 288 shows the important feature of a mound at $R=0.345$ accompanied by a hollow on the other side of the diametral node.

Fig. 2



Profiles of unsymmetrical waves.

No exact solution is known for a circular basin of variable depth, but by means of Rayleigh's principle an approximation may be found to the period of the slowest mode in a hemispherical basin. As an approximate type we assume that the free surface remains plane. Lamb (1932) shows that, for a liquid of density ρ , a semicircular element of radius b and thickness dx possesses kinetic energy T given by

$$T = \left(\frac{2}{\pi} - \frac{\pi}{8} \right) \rho b^4 \dot{\beta}^2 dx, \quad \dots \quad (2.1)$$

and potential energy V given by

$$V = \frac{1}{3} g \rho b^3 \beta^2 dx, \quad \dots \quad (2.2)$$

when the plane surface is inclined at an angle β to the horizontal. We will employ these expressions in the manner indicated in fig. 3 which shows a plan of a hemisphere of radius a . It follows from (2.1) that the kinetic energy of the hemispherical mass of liquid is

$$2 \left(\frac{2}{\pi} - \frac{\pi}{8} \right) \rho a^5 \dot{\beta}^2 \int_0^{\pi/2} \cos^5 \delta \, d\delta = 0.2602 \rho a^5 \dot{\beta}^2, \quad \dots \quad (2.3)$$

and from (2.2) that the potential energy is

$$\frac{2}{3} g \rho a^4 \beta^2 \int_0^{\pi/2} \cos^4 \delta \, d\delta = 0.3827 g \rho a^4 \beta^2. \quad \dots \quad (2.4)$$

We assume that $\beta \propto \cos \sigma t'$, and the method yields

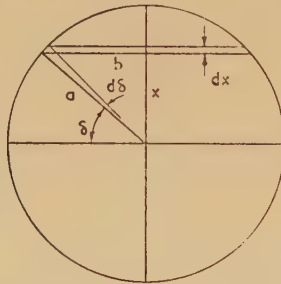
$$\sigma^2 = \frac{0.3827}{0.2602} \frac{g}{a}, \quad (2.5)$$

hence the period τ is given by

$$\tau = \frac{2\pi}{\sigma} = 5.115 \left(\frac{a}{g} \right)^{1/2} (2.6)$$

It is known that this estimate is slightly too small. To check (2.6) a hemisphere of radius about $5\frac{5}{8}$ in. was placed on a table and filled with water almost to the brim. When the table was momentarily shaken, it was found that the mode of oscillation contemplated could in fact occur and that its period was 0.60 sec. The value calculated from (2.6) is 0.62 sec, showing reasonable agreement with the experiment.

Fig. 3



Plan of hemispherical basin.

For a circular basin of radius and depth both equal to a , the gravest period is $\tau = 4.738(a/g)^{1/2}$, which is smaller than (2.6) because the kinetic energy is less for a given displacement, while the potential energy is the same. But the effect of rounding off the sharp corner in the circular basin is not large. Many fountain basins have a cross section of shallow elliptical form, intermediate between rectangular and hemispherical. An approximation to the gravest period can be made by means of Rayleigh's theory (1876) with the depth taken to be the maximum depth. This estimate will be somewhat too small because the kinetic energy is greater than when the depth is uniform.

§ 3. THE THEORY OF THE TRAJECTORY OF THE
PARTIALLY OBSTRUCTED JET

In order to discover how the impact of the falling jet stimulates the oscillations we must know when and where a jet from a submerged nozzle will impinge. We consider a nozzle delivering, when unsubmerged, a jet of velocity V_1 at an angle α to the horizontal and fixed with its outlet exactly at the mean level in the basin. Time t' will be measured from the instant when submergence of the nozzle by the rise of the

neighbouring surface has just begun. Submergence lasts until $t' = \tau/2$, and it will be assumed that the minimum jet velocity, denoted by V_2 , occurs at $t' = \tau/4$. Nothing seems to be known about the velocity and diameter of the jet cast into the air from a submerged nozzle, even when the surrounding water is quiescent. Here we will suppose that refraction is negligible and that the jet velocity v varies in the sinusoidal manner

$$v = V_1 \left\{ 1 - \left(1 - \frac{V_2}{V_1} \right) \sin 2\pi \frac{t'}{\tau} \right\} \quad (3.1)$$

At $t' = 0$ the surrounding surface is moving with its maximum velocity, and (3.1) is arranged to give the greatest rate of reduction at that instant. We will now follow the trajectory of a particle leaving the nozzle at time t' on the supposition that its path through the surrounding water is negligibly short compared with its path through the air. Air resistance and interference in the air between different parts of the jet being ignored, the required relations are obtainable by very elementary methods. If the maximum and minimum heights attained are denoted by H_1 and H_2 and the maximum and minimum ranges by \mathcal{R}_1 and \mathcal{R}_2 ,

$$H_1 = \frac{(V_1 \sin \alpha)^2}{2g}, \quad (3.2)$$

$$\mathcal{R}_1 = \frac{V_1^2}{g} \sin 2\alpha; \quad (3.3)$$

and the ratio V_2/V_1 can be found from either

$$\frac{V_2}{V_1} = \left(\frac{H_2}{H_1} \right)^{1/2}, \quad (3.4)$$

or

$$\frac{V_2}{V_1} = \left(\frac{\mathcal{R}_2}{\mathcal{R}_1} \right)^{1/2}. \quad (3.5)$$

Corresponding to a jet velocity v , the range is

$$\mathcal{R}' = \frac{v^2}{g} \sin 2\alpha, \quad (3.6)$$

and the time of flight is

$$2 \frac{v}{g} \sin \alpha. \quad (3.7)$$

We now introduce dimensionless quantities by writing

$$\mathcal{R} = \frac{\mathcal{R}'}{\mathcal{R}_1} \quad \text{and} \quad t = \frac{t'}{\tau}. \quad (3.8)$$

Then from (3.1), (3.3) and (3.6) the non-dimensional range is

$$\mathcal{R} = \left\{ 1 - \left(1 - \frac{V_2}{V_1} \right) \sin 2\pi t \right\}^2; \quad (3.9)$$

and with the origin of time mentioned above, the non-dimensional time of striking the surface is found from (3.2) and (3.7) to be

$$t_s = t + \frac{2}{\tau} \left(\frac{2H_1}{g} \right)^{1/2} \left\{ 1 - \left(1 - \frac{V_2}{V_1} \right) \sin 2\pi t \right\}, \quad (3.10)$$

the factor of the term in twisted brackets being the non-dimensional time of flight of the unobstructed jet. The eqns. (3.9) and (3.10) hold good for $0 < t < \tau/2$, and for the remainder of the period we have merely to take V_2/V_1 as unity. When H_1 , τ and V_2/V_1 are known, the procedure is to insert in (3.9) and (3.10) a series of equidistant values of t , and the results, when plotted together, show the nature of the fall of the jet over a complete period. For a vertical jet we put $\sin \alpha = 1$ and omit all mention of \mathcal{R} .

Occasionally it was noticed that the jet was unobstructed for appreciably less than half a period. To meet these conditions we will suppose that submergence lasts for $3\tau/4$, beginning at $t' = -\tau/8$ and ending at $t' = 5\tau/8$. Again we assume a sinusoidal variation in velocity, so that (3.1) is replaced by

$$v = V_1 \left\{ 1 - \left(1 - \frac{V_2}{V_1} \right) \sin \frac{4\pi}{3} \left(\frac{t'}{\tau} + \frac{1}{8} \right) \right\}. \quad (3.11)$$

Equations (3.2)–(3.8) are still applicable, and (3.9) and (3.10) become

$$\mathcal{R} = \left\{ 1 - \left(1 - \frac{V_2}{V_1} \right) \sin \frac{4\pi}{3} \left(t + \frac{1}{8} \right) \right\}^2, \quad (3.12)$$

and
$$t_s = t + \frac{2}{\tau} \left(\frac{2H_1}{g} \right)^{1/2} \left\{ 1 - \left(1 - \frac{V_2}{V_1} \right) \sin \frac{4\pi}{3} \left(t + \frac{1}{8} \right) \right\}. \quad (3.13)$$

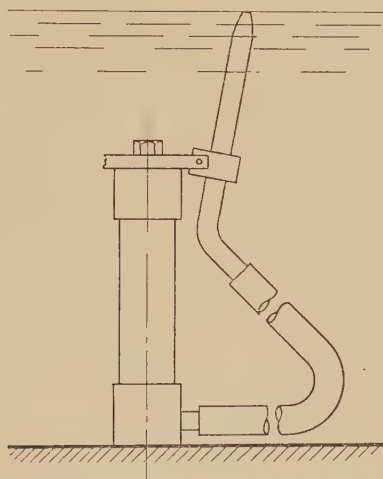
§ 4. DESCRIPTION OF THE EXPERIMENTS AND COMPARISON WITH THEORY

A symmetrical arrangement of three jets, one of which is shown in fig. 4, was fitted at the centre of a circular tank of diameter 36 in. and depth 9 in. The nozzles were made of glass tubing drawn out to about 0.15 in. diameter. It was soon discovered that a single nozzle was sufficient to excite oscillations. Thereafter, usually only one was used, but the others served as gauges indicating whether the oscillation was symmetrical or not. For operation in other positions in the tank, the nozzle was mounted on a clamp and stand. The water escaped from the tank near the periphery through a vertical pipe which terminated in a small circular weir on a screw thread: thus by rotation of the weir the water level could be finely adjusted.

In experiments with an inclined jet the usual method was to set the nozzle just clear of the surrounding surface. After the maximum height H_1 of the trajectory had been measured, the water level was raised by means of the weir until disturbance of the jet began: at intervals of some minutes the level was raised further in small steps, ample time being allowed for pulsations to make themselves apparent. If steady oscillations set in, they were timed by watching the nozzle, observing the top of the trajectory, or listening to the rhythmic 'flop' that often occurred, due to the simultaneous impact of a large part of the jet. The surface in the tank was violently disturbed by the falling jet, which threw up random waves of small length, and it was impossible to discern

any regular oscillation at the periphery, still less the position of nodes. The general commotion made the action of the submerged nozzle irregular and the accurate observation of H_2 and \mathcal{R}_2 a matter of extreme difficulty when the trajectory was long. No attempt was made to determine the wave amplitude, which was probably of the order of $\frac{1}{4}$ in. near the nozzle. When once the correct setting of H_1 and of the circular weir had been discovered, the pulsations set in quickly after the apparatus had been started from rest, the maximum time required being not more than a couple of minutes. On no occasion were the oscillations stimulated artificially.

Fig. 4



Elevation of nozzle and support.

In the vertical tests, the nozzle was set slightly out of the plumb in order to reduce interference between different parts of the jet. Nevertheless, the water that rose to the minimum height was often struck there and dispersed by the free jet following up behind. It proved possible to excite symmetrical and asymmetrical oscillations with both inclined and vertical jets, and the experimental results can be conveniently divided into the four groups shown in tables 2 and 3. In all the tests there was no ambiguity about the mode, for the observed periods were close to one of the theoretical values set out in table 1.

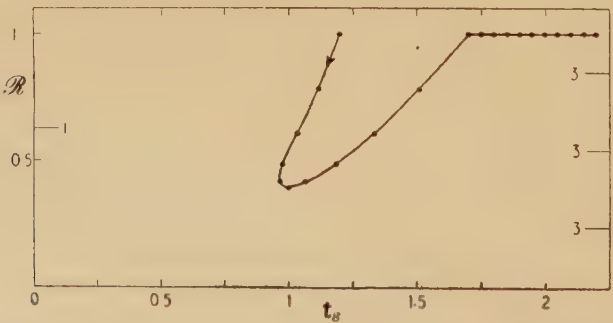
In the first group—oscillations with circular symmetry excited by an inclined jet—the nozzle was held nearly at the centre and arranged to strike (when unobstructed) close to the periphery. In the slowest mode (1), the nozzle was seen to be submerged for about half the period and so (3.9) and (3.10) apply. They have been used with the results in table 2 to produce fig. 5, in which \mathcal{R} is plotted upwards on a base of t_s . The diagram begins at $t=0$, $t_s=1.2$, $\mathcal{R}=1$, and continues in the direction of the arrow. For $0 \leq t \leq 1$, the points on the curve were

calculated at intervals of t equal to $1/20$; and since the time intervals are the same, approximately equal volumes of water impinged between each pair of adjacent points. Figure 1 indicates that the waves at the centre and at the periphery were in anti-phase, and the node is marked on the left-hand vertical axis in fig. 5. It was noticed that a concentrated fall of low-velocity water took place at the minimum radius, preceded by a quick fall from the periphery inwards ; the subsequent fall outwards

Table 2. Experiments with Symmetrical Modes

Mode	τ sec	H_1 in.	H_2 in.	R_2 in.	$\frac{V_2}{V_1}$	$\frac{2}{\tau} \left(\frac{2H_1}{g} \right)^{1/2}$
Inclined jet						
1	0.714	35	—	7	0.62	1.20
2	0.520	8	—	8	0.67	0.79
3	0.432	13	—	8	0.67	1.21
4	0.380	17	—	9	0.71	1.57
Vertical jet						
1	0.709	61	24	—	0.63	1.59
2	0.508	33	13	—	0.63	1.63
3	0.432	22	9	—	0.64	1.57
4	0.380	17	7	—	0.64	1.57

Fig. 5



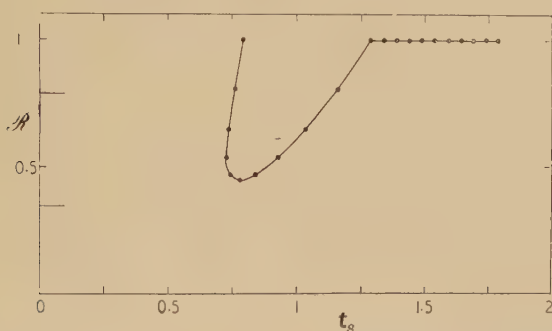
Fall of jet from inclined nozzle at centre ; circular symmetry, one node and three nodes.

along the radius seemed very light. The diagram explains the first and third of these observations but not the second : the trend of the initial part of the curve, instead of being to the left, should have been slightly to the right. Thus the cut-off of the jet by the rising wave was not as sharp as postulated in the theory. The minimum radius was rather variable, but whatever the exact timing of the above events may have been, they occurred across the node not far from $t_g=1$ when the surface

was flat, hence their effect on the oscillation could not have been large. The main stimulus seems to have come from the unobstructed jet which struck in the interval $1.7 < t_s < 2.2$. At $t_s = 1.75$ the wave at the periphery was at a crest, hence a powerful force was exerted on the descending wave. Points in fig. 5, for which t_s differs by unity, are simultaneous, therefore the low-velocity concentration struck while the high-velocity fall was in progress, and it is not surprising that a 'flop' was heard.

The second mode (2) was remarkably regular and easy to obtain. Conditions were now different because the waves at the centre and at the periphery were in phase. The corresponding $\mathcal{H} - t_s$ curve is given in fig. 6 with the nodes marked on the left. The obstructed jet was seen

Fig. 6



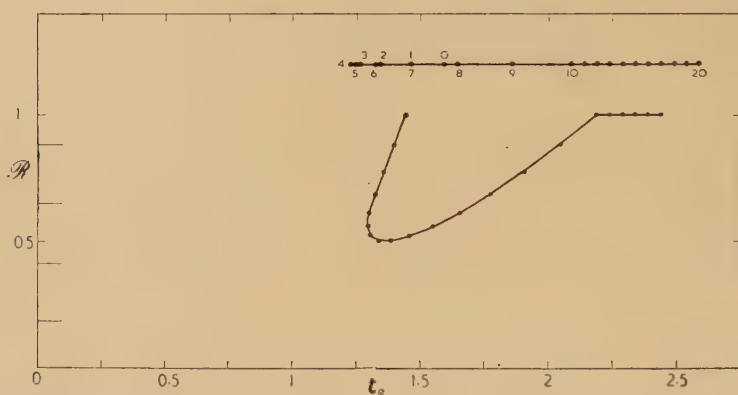
Fall of jet from inclined nozzle at centre ; circular symmetry, two nodes.

to fall in much the same manner as before, and now the initial part of the curve is nearly vertical, in better agreement with observation. At $t_s = 0.75$ the region between the two nodes was at its maximum elevation and the motion was assisted by the concentrated fall of water in that area at that instant. At $t_s = 1.25$ the wave at that periphery was at a crest, and again the unobstructed jet fell on a subsiding wave. It should be added that with the nozzle fixed near the periphery and trained on the centre a short attempt to produce the gravest mode failed when the jet was arranged in accordance with the first line of table 2. Instead, the second mode appeared at $H_1 = 36$ in., $\mathcal{H}_2 = 9$ in., to which the corresponding time of flight is 1.63. Thus the unobstructed jet was in the air for almost an additional period compared with the value in table 2. This experience of searching for one mode and finding another was not uncommon.

The third mode (3) is seen from the final column of table 2 to be dynamically identical with the first, and fig. 5, to which the positions of the nodes have been added on the right, will serve to explain the action. The fourth mode (4) was difficult to obtain, the setting of the two controls being delicate. In this test only, the nozzle was clearly submerged for more than half the period, and the curve in fig. 7 has been drawn with

the aid of (3.12) and (3.13). At $t_s=1.25$ the region between the two middle nodes was at its maximum elevation, thus the motion was assisted by the concentrated low-velocity fall. At the periphery the wave crest occurred at $t_s=2.25$, and again the unobstructed jet was helpful. It was not found possible to animate this mode with a jet travelling in the air for only about half a period.

Fig. 7



Fall of jet from inclined nozzle at centre: circular symmetry, four nodes. Above: fall of jet from vertical nozzle at centre.

The corresponding experiments with an almost vertical jet placed at the centre are summarized in the lower part of table 2: dynamically they are all the same as the fourth mode above, which also was principally excited by impact at a point in phase with the wave at the nozzle. For the slowest mode (1), one jet was used, but for the three higher modes the feebler jets were often momentarily upset by interference, and the usual timing over 50 cycles was difficult. Therefore, for these three experiments only, three jets were employed to facilitate timing. The $R-t_s$ curve now degenerates into the straight line with the numbered points plotted at the top of fig. 7. The wave at the centre was at a crest at $t_s=1.25$, and the concentrated low-velocity fall occurred also at that instant. The unobstructed jet fell on both sides of the next crest at $t_s=2.25$. We recognize that water falling on a rising wave that has passed its mean position does not entirely oppose the motion; although the impulsive pressure is in the contrary direction, yet weight added to an elevation promotes the oscillation. Thus assistance was provided by the unobstructed jet. Experiments with an almost vertical jet placed close to the periphery were not pursued, because interference caused much water to be thrown out of the tank.

The experimental results with the asymmetrical modes are set out in table 3. The test with the slowest mode (i) was spectacular, and the summit of the trajectory varied gracefully between heights about 102

and 52 in. Since the jet was nearly vertical, there was much interference : but when the water from the submerged nozzle avoided collision, it fell close to the centre of the basin and had no influence on the oscillation. The second mode (ii) was produced in four ways with the nozzle placed in the mound position. The first three were with the nozzle trained on an antiphase point, and they are dynamically identical with the first and third entries in table 2, which also were carried out with impingement on an antiphase point. Now the modes and the fall of the obstructed jet were widely different in these five experiments, thus it appears that the main stimulus to the oscillations came from the properly timed impact of the unobstructed jet, the feebler obstructed jet having an effect only of minor importance. The fourth and the last lines in table 3 refer to experiments with impact on a point in phase, and the times of flight differed by half a period from the first three tests. The fifth test was with anti-phase conditions, the time of flight being a whole period greater than before.

Table 3. Experiments with Asymmetrical Modes

Mode	τ sec	H_1 in.	\mathcal{R}_1 in.	\mathcal{R}_2 in.	$\frac{V_2}{V_1}$	$\frac{2}{\tau} \left(\frac{2H_1}{g} \right)^{1/2}$	Nozzle at	Trained on
Inclined jet i 1.200		102	36	18	0.71	1.22	periphery	other end of same diameter
ii 0.600		$24\frac{1}{2}$	12	6	0.71	1.19	mound	hollow
ii 0.595		25	12	5	0.65	1.21	mound	nearer end of same diameter
ii 0.597		8	24	8	0.58	0.68	mound	further end of same diameter
iii 0.469		52	24	7	0.54	2.22	mound	further end of same diameter
Vertical jet ii 0.600		52	$H_2=21$		0.64	1.74	mound	—

When a pulsating jet is required in a fountain basin, the following procedure should be adopted. First, the mode and the method of obtaining it must be decided, and then an estimate of the period is made, as explained in §2. The unobstructed jet is set at the value of H_1 calculated from the dimensionless time of flight given in table 2 or 3, and the basin level is slowly raised until pulsations set in.

REFERENCES

- BINNIE, A. M., and HOOKINGS, G. A., 1948, *Proc. Roy. Soc. A*, **194**, 398.
 LAMB, Sir H., 1932, *Hydrodynamics*, pp. 440, 444 (Cambridge Univ. Press).
 RAYLEIGH, Lord, 1876, *Phil. Mag.* (5), **1**, 257, Papers 1, 251.

XL. *A New Vacuum Calorimeter for Low Temperatures*

By K. G. RAMANATHAN and T. M. SRINIVASAN
National Physical Laboratory of India, New Delhi*

[Received November 17, 1954]

§ 1. INTRODUCTION

A CRYOSTAT with a hermetically sealed vacuum calorimeter has recently been developed in this laboratory for investigating the specific heats of solids at low temperatures. In this apparatus the use of an exchange gas and the operation of high vacuum equipment necessary with calorimeters of conventional design are avoided by the introduction of a mechanical arrangement which can make or break a thermal contact of the specimen with the bath as necessary.† With slight modifications in technique the cryostat, which is now being used for measurements in the liquid helium range, could also be used for calorimetry up to 50°K . Its performance has been tested by some preliminary measurements on the specific heat of tin in the range $1.5\text{--}4.2^{\circ}\text{K}$.

§ 2. DESCRIPTION OF APPARATUS

Figure 1 shows the contact making mechanism and the calorimeter chamber C. Inside C the specimen S_1 is suspended by fine eureka wires of negligible heat conductance from the metal disc D_1 maintained at the helium bath temperature by the copper wire heat-leak L. It can be moved up and down without breaking the vacuum by means of the assembly at the top consisting of the metal bellows B, the spring S_2 , and the nut N. The disc D_1 shields the specimen from any possible heating effects due to radiation or 'hot molecules' of gas from the top of the cryostat. The disc D_2 which is also maintained at liquid helium temperature, presses against the specimen when it is in the lowest position to give the thermal contact with the bath.

The temperature of the specimen is measured with the carbon resistance thermometer T_1 (a $\frac{1}{2}$ watt resistor of 12 ohm room temperature resistance, manufactured by Allen Bradley). This is cemented inside a hole drilled in the specimen. Its resistance temperature curve is determined by measurements with the specimen in contact with the calorimeter bottom, the bath temperature being found from the helium vapour pressure

* Communicated by D. Shoenberg.

† While this work was in progress, we heard from Dr. D. Shoenberg, that a calorimeter based on the same principle had been developed at the Clarendon Laboratory, Oxford (Webb, F. J., *Thesis*, Oxford 1953). After submitting for publication we also heard of the work of Westrum, *et al.* (1953, *J. Chem. Phys.*, 21, 419), in which a mechanical contact is used for cooling specimens in a different type of calorimeter.

tables published by Van Dijk and Shoenberg (1949). It exhibits a variation from 120 to 1300 ohms in the range 4.2–1.5°K. The resistance measuring bridge could detect changes equivalent to temperature changes of 10^{-4} °K at 4°K with a measuring current of 10 microamps. This sensitivity increases at lower temperatures and is about seven times higher at 1.5°K.

The electrical leads to the thermometer and heating coil H, which are in thermal contact with the bath inside the metal capillary T_2 , are sealed

Fig. 1

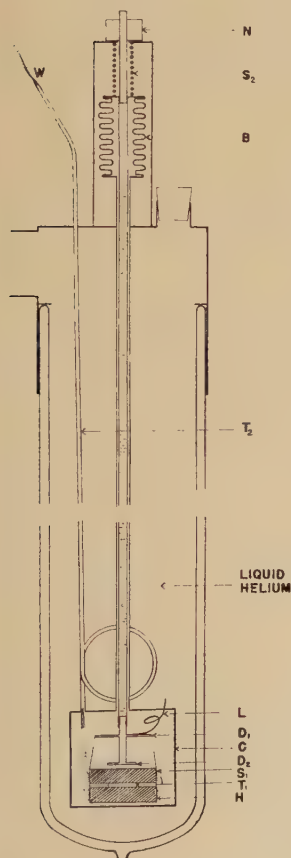
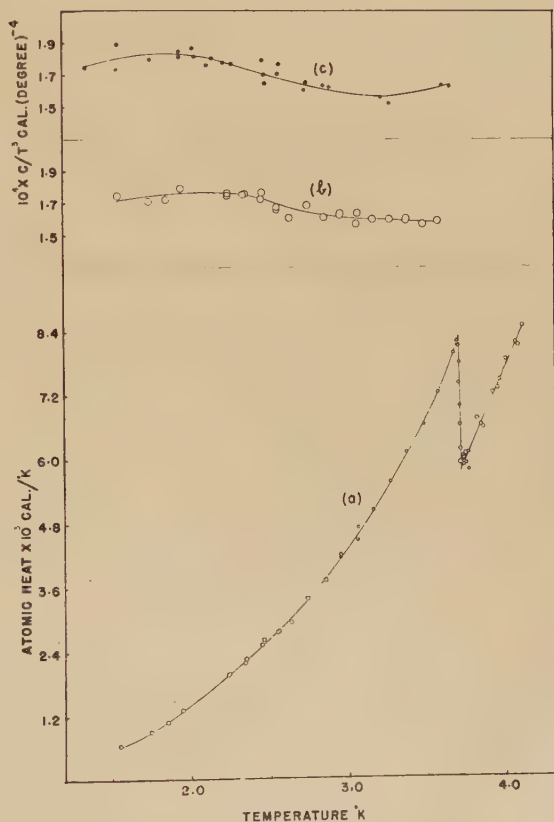


Fig. 2



off with wax at W; in an earlier design the leads were brought out through glass-metal seals in the calorimeter, but these often gave rise to leaks and were abandoned. At all other joints the vacuum system is sealed hermetically by soldering. On filling the cryostat with liquid helium the air inside the calorimeter is frozen out and a vacuum better than any obtainable with diffusion pumps is produced. The specimen is kept raised during this process to prevent it being frozen to the calorimeter bottom by frozen air. Later it is cooled to the bath temperature by making contact with the bottom of the calorimeter.

The specific heats at various temperatures are measured by isolating the specimen from the bath, passing a known electrical power for a definite time through the heating coil and measuring the rise in temperature ΔT . In these measurements the specimen is always kept within 0.04°K of the bath temperature so that the heat lost during the measuring interval along the leads and suspension wires is negligible (less than 0.25% of the total heat). When this temperature difference is much larger a correction has to be applied for this loss.

The quantity of heat dissipated in the specimen is calculated from the known resistance of the coil, the heating time and the current. The change ΔT in temperature, which is usually of the order of 0.02°K , could be measured to 1% accuracy. The accuracy of determination of specific heats is estimated to be better than 3% down to 1.5°K .

§ 3. RESULTS

Figure 2 (a) is a plot of the variation of the specific heat of tin in the liquid helium range. It is seen that the scatter of points in the curve is less than 3% except near the superconducting transition point where very small intervals (0.003°K) of temperature had to be used. The magnitude of the jump in the atomic heat at the superconducting transition point 3.71°K , is $0.0025 \text{ cal}/^\circ\text{K}$. This agrees well with the value $0.0026 \text{ cal}/^\circ\text{K}$ calculated from Rutgers's formula using the known value of dH_c/dT at the transition point (H_c is the critical magnetic field). Figure 2 (b) shows the variation of C/T^3 with T observed by us. The results obtained by Keesom and Van Laer (1938) are also reproduced in fig. 2 (c) for comparison. It can be seen that the two curves are similar in character, and there is good agreement between the absolute magnitudes of C/T^3 . These results show that the new calorimeter compares well in performance with those of more conventional design.

ACKNOWLEDGMENTS

We wish to thank Sir K. S. Krishnan, F.R.S., Director, National Physical Laboratory of India and Dr. D. Shoenberg, F.R.S., Royal Society Mond Laboratory, Cambridge, for their kind interest in this work. We are also obliged to Dr. J. K. Hulm, Institute for the study of Metals, Chicago, for supplying us with the carbon thermometer.

REFERENCES

- KEESOM, W. H., and VAN LAER, P. H., 1938, *Physica*, **5**, 193.
VAN DIJK, H., and SHOENBERG, D., 1949, *Nature, Lond.*, **164**, 151.

XLII. The Emission of Alpha Particles from Argon under Bombardment with Neutrons

By E. H. BELLAMY and F. C. FLACK*
Department of Natural Philosophy, Glasgow†

[Received November 30, 1954]

ABSTRACT

Groups of particles have been observed from the bombardment of argon with neutrons using a high pressure gridded ionization chamber. The chief reaction is $^{40}\text{Ar}(n, \alpha)^{37}\text{S}$ with a measured Q -value of -2.5 ± 0.1 mev, and transitions were observed to excited levels in ^{37}S at 1.3 ± 0.05 , 2.2 ± 0.1 , and 2.7 ± 0.1 mev. The cross section for the ground state transition is approximately 30 μ barns.

§ 1. EXPERIMENTAL

A GRIDDED ionization chamber with a counting volume of 1.5 litres containing argon at a pressure of 30 atmospheres was bombarded with neutrons from the $^3\text{H}(d, n)^4\text{He}$ reaction. The resultant pulses after amplification were analysed on an 80 channel kicksorter (Hutchinson and Scarrott 1951). The result of such an experiment carried out at 90° to the 250 kev deuteron beam is shown in the figure. In addition to well defined peaks (A and B), evidence exists of other peaks as indicated by the arrows.

Owing to slight alterations in overall gain and kicksorter bias, from day to day, which altered the position of the peaks by about 2%, the data from experiments which were made at intervals of several days cannot be immediately added on one graph, but particle groups corresponding to positions C and D shown in the figure are present in each of several pulse distributions. The presence of a group at position E is also strongly indicated, although the data are not conclusive.

The higher energy end of the distribution can be compounded from peaks of full width at half-maximum of 6% at energies of 11.6, 10.3, 9.4, 8.9 and 8.1 mev with relative intensities of 1.0, 1.45, 2.2, 1.5 and 1.0 respectively, together with a steeply rising lower energy component which has zero intensity at 9.4 mev, but an intensity at 8.1 mev which is more than twice that of the peak at this position.

Polonium α -particles from a weak source were used to calibrate the energy scale and provide the resolution expected for a running time of several hours. The resolution obtained with a strong source when

* Communicated by Professor P. I. Dee.

† Now at University College of the South West, Exeter.

amplifier and kicksorter drifts were negligible was 3%. An experiment with neutrons having a mean energy of 14.8 mev gave the same Q values for the peaks A and B, but owing to the much larger spread in neutron energy (± 0.3 mev), the resolution was much poorer than in the figure, and the peaks C and D were not resolved.

The neutron spectrum was examined by observing the recoil protons in a plastic phosphor. There was a small contamination of 2.5 mev neutrons from the $d(d, n)t$ reaction.



§ 2. INTERPRETATION OF RESULTS

There can be little doubt that peak A corresponds to the reaction $^{40}\text{A}(n, \alpha)^{37}\text{S}$ in which the sulphur nucleus is left in the ground state. The reactions (n, α) and (n, p) in ^{36}A (0.33% abundant) are expected to produce peaks at $E=16.1$ and 14.2 mev, of which there is little evidence. ^{38}A is present only to 0.07% and corresponding peaks are expected at 13.9 mev for the α -reaction which does not appear, and at 10 mev where it would be hard to detect. (n, d) reactions would give peaks at 7.9 and 8.1 mev respectively for these two nuclei, but owing to the low abundances, excessive cross sections would be required for these reactions to give a detectable contribution to the peaks found.

This leaves, then, only reactions in ^{40}A to account for the remaining peaks. The Q values for the reactions $^{36}\text{A}(\text{n}, \text{p})^{36}\text{Cl}$ and $^{38}\text{A}(\text{n}, \text{p})^{38}\text{Cl}$ would indicate that the Q value for the reaction $^{40}\text{A}(\text{n}, \text{p})^{40}\text{Cl}$ is certainly less than -4 mev and is likely to be about -8 mev, so that all the assignments can be made to the reaction $^{40}\text{A}(\text{n}, \alpha)^{37}\text{Cl}$. The resulting Q -values and excited levels in ^{37}Cl are shown in the table. The cross section for the ground state transition was calculated from the integrated deuteron current incident on the target and is unlikely to be correct to better than 50%.

Peak	Intensity	E peak (mev)	Q (mev)	Levels in ^{37}Cl (mev)
A	1.0	11.6	-2.5 ± 0.1	ground state
B	1.45	10.3	-3.8	1.3 ± 0.05
C	2.2	9.4	-4.7	2.2 ± 0.1
D	1.15	8.9	-5.2	2.7 ± 0.1
(E)	1	8.1	-6.0	3.5 ± 0.2

The energy limits for charged particles from the (n, d) and (n, pn) reactions in ^{40}A are marked in the figure. The Q -value for the $^{40}\text{A}(\gamma, \text{p})^{39}\text{Cl}$ reaction as determined by Wilkinson and Carver (1951) has been used to determine these limits. The steps in the curve may be associated with these reactions.

The Q -value for the ground state reaction together with the mass-spectrometer determinations of the ^{40}A and ^{37}Cl masses can be used to compute the end-point energy of the β -ray (10%) to the ground state of ^{37}Cl from the 5 min ^{37}S decay. A value of 4.9 ± 0.2 mev is obtained which is not in strong disagreement with the value of 4.3 ± 0.3 mev obtained by an Aluminium absorption determination (Bleuler and Zunti 1946). This Q -value also confirms the assignment (Endt and Kluyver 1954) of the α -particles observed by Graves and Coon (1946) with 2.5 mev neutrons to the $^{36}\text{A}(\text{n}, \alpha)^{33}\text{S}$ reaction.

REFERENCES

- BLEULER, E., and ZUNTI, W., 1946, *Hel. Phys. Acta*, **19**, 133.
 ENDT, P. M., and KLUYVER, J. C., 1954, *Rev. Mod. Phys.*, **26**, 95.
 GRAVES, E. R., and COON, J. H., 1946, *Phys. Rev.*, **70**, 101 (A).
 HUTCHINSON, G. W., and SCARROTT, G. G., 1951, *Phil. Mag.*, **42**, 792.
 WILKINSON, D. H., and CARVER, J. H., 1951, *Phys. Rev.*, **83**, 466 (L).

XLII. *Spallation of Elements in the Mass Range 51-75*

By S. G. RUDSTAM

The Gustaf Werner Institute for Nuclear Chemistry, University
of Uppsala, Uppsala, Sweden*

[Received November 17, 1954]

SUMMARY

Empirical formulae for the yields of the products obtained in spallation reactions with high energy particles are constructed. These formulae reproduce most of the experimentally determined cross sections within a factor of 2, and they simplify the comparison between different spallation investigations.

§ 1. INTRODUCTION

THE spallation of medium weight elements has been fairly well studied. The mass region best investigated is probably 51-75. In this region the following spallation studies are found in the literature: vanadium, manganese, and cobalt + 187 mev protons (Rudstam 1953), iron + 340 mev protons (Rudstam, Stevenson, and Folger 1952), cobalt + 240 mev protons (Wagner and Wiig 1952), cobalt + 370 mev protons (Belmont and Miller 1954), copper + 60 mev protons (Carleson 1954), copper + 190 mev deuterons, 340 mev protons and 380 mev alpha particles (Batzel, Miller, and Seaborg 1951, Miller, Thompson and Cunningham 1948), copper + 400 mev neutrons (Marquez 1952), copper + 2.2 bev protons (Friedlander, Miller, Wolfgang, Hudis, and Baker 1954), zinc + 340 mev protons (Worthington 1952), and arsenic + 190 mev deuterons (Hopkins and Cunningham 1948). It is seen that the conditions of the investigations differ widely. It is of great interest to compare these different groups of spallation reactions,† but this is not easily done if the spallation yields are given merely as a set of tabulated cross sections.

However, for vanadium bombarded with 187 mev protons, the cross sections can be expressed by a formula of the following type (Rudstam 1953):

$$\sigma(A_i, Z_i) = \exp [P \cdot A_i - Q - R(Z_i - S \cdot A_i)^2], \quad . . . \quad (1)$$

where $\sigma(A_i, Z_i)$ is the formation cross section of the nuclide with the mass number A_i and the atomic number Z_i , and P , Q , R , and S are constants.

If the spallation groups mentioned before could be characterized by an equation of this type, this would greatly facilitate the comparison between them. The purpose of the present study was to investigate the application

* Communicated by Professor The Svedberg, F.R.S.

† By a group of spallation reactions, or a spallation group, is meant all the spallation reactions associated with the bombardment of a given element (X) with particles of a given kind (a) and energy (E). Notation: $G(X; a; E)$.

of the formula (1) to the spallation of elements in the mass range 51-75 and then to use the results for a comparison between these spallation groups.

§ 2. DETERMINATION OF THE CROSS SECTION FORMULA

The cross section formula (1) for a group of spallation reactions can be determined from the measured cross sections in the following way. The formula is written :

$$\log_e \sigma(A_i, Z_i) = P \cdot A_i - Q - R(Z_i - S \cdot A_i)^2. \quad . \quad . \quad (2)$$

An arbitrary value is chosen for the parameter S , and the method of least squares is then used to determine the best values of the parameters P , Q , and R from the known data of $\log_e \sigma(A_i, Z_i)$, A_i , and $(Z_i - S \cdot A_i)^2$. The root-mean-square error ϵ of the logarithm of the cross sections is calculated, and different values of S are tried until the minimum of ϵ is found. The corresponding values of P , Q , R , and S give the best formula of the type (1) for the cross sections, and the value of ϵ_{\min} shows how successful the formula is, because the average ratio between experimental and calculated cross sections is given by the factor $e^{\pm \epsilon}$.

The experimental cross sections used for the determination of the cross section formulae should be the independent cross sections for primary formed spallation products. However, the independent cross section of a nucleus is generally much lower than the independent cross section of its daughter nucleus for the actual spallation reactions. For this reason the measured cross sections can be regarded as independent.

Since the cross section formula cannot be expected to hold over all mass numbers, the mass region used in the calculations was arbitrarily limited to between 30 and 2 mass numbers below the lowest mass number of the target isotopes.

§ 3. RESULTS OF THE CALCULATIONS

The parameters P , Q , R , and S , and the factor e^ϵ are tabulated in table I for twelve different groups of spallation reactions.

The cross section formula fits remarkably well as is seen from the values of e^ϵ . In most cases this factor is less than 2, which means that the cross section formula reproduces the experimental cross sections within a factor of 2 on the average. This is satisfactory since the cross sections often vary by a factor of 10^3 or more, and moreover the experimental cross sections may sometimes be inaccurate to a factor of 2. Thus one may conclude that the cross section formula (1) is a good approximation to the cross section distribution for spallation of elements in the actual mass region. For a given spallation group, the cross section distribution can then be roughly characterized as follows :

(1) The yields* of the spallation products vary regularly with their atomic number and mass number. This is indicated by the mere possibility of expressing all the cross sections by a simple formula.

* The yields are proportional to the cross sections.

(2) The yield-mass curve, that is the total isobaric yield $\sigma(A)$ versus the mass number, increases exponentially with the mass number. This is seen by the following argument.

$$\sigma(A) = \sum_Z \sigma(A, Z) = \exp [P \cdot A - Q] \sum_Z \exp [-R(Z - S \cdot A)^2] \\ \sim \exp [P \cdot A - Q] \int_{Z_1}^{Z_2} \exp [-R(Z - S \cdot A)^2] dZ.$$

The limits of integration, Z_1 and Z_2 , are the smallest and the largest obtainable value of Z . If R is not too small this integral will not differ much from the integral with the limits $-\infty$ and $+\infty$. One then obtains

$$\sigma(A) \sim \exp [P \cdot A - Q] \int_{-\infty}^{\infty} \exp [-R(Z - S \cdot A)^2] dZ \\ = (\pi/R)^{1/2} \cdot \exp [P \cdot A - Q]. \quad (3)$$

Table 1

Spallation group	P	Q	R	S	e^E
G(V ; p ; 187 mev)	0.377 ± 0.014	11.93 ± 0.52	1.80 ± 0.11	0.466	1.46
G(Mn ; p ; 187 mev)	0.297 ± 0.018	12.55 ± 0.67	1.38 ± 0.08	0.471	1.25
G(Cu ; d ; 190 mev)	0.311 ± 0.026	18.55 ± 1.25	1.10 ± 0.25	0.465	2.09
G(As ; d ; 190 mev)	0.348 ± 0.054	24.86 ± 3.40	0.68 ± 0.17	0.463	3.13
G(Fe ; p ; 340 mev)	0.253 ± 0.018	9.98 ± 0.77	1.37 ± 0.11	0.472	1.59
G(Co ; p ; 370 mev)	0.232 ± 0.024	8.96 ± 1.03	1.28 ± 0.17	0.468	2.06
G(Zn ; p ; 340 mev)	0.239 ± 0.022	10.41 ± 1.07	1.45 ± 0.15	0.469	1.97
G(Cu ; p ; 340 mev)	0.256 ± 0.016	14.44 ± 0.82	1.41 ± 0.13	0.468	1.81
G(Cu ; p ; 60 mev)	0.956 ± 0.119	57.84 ± 6.80	1.41 ± 0.21	0.472	1.94
G(Cu ; p ; 2200 mev)	0.072 ± 0.015	1.36 ± 0.71	1.22 ± 0.13	0.466	1.87
G(Cu ; n ; 400 mev)	0.350 ± 0.067	17.11 ± 3.70	1.21 ± 0.37	0.466	2.62
G(Cu ; α ; 380 mev)	0.236 ± 0.036	15.04 ± 1.88	0.81 ± 0.32	0.468	1.81

The parameter P is thus a measure of the steepness of this exponential increase in the yield-mass curve.

(3) The charge distribution curve, that is, the independent yield versus the atomic number for isobars, is a gaussian function of the atomic number with a precision index ($=R^{1/2}$) which is independent of the mass number. In this connection it is of interest to note that the assumption of a charge distribution curve independent of mass number is consistent with evidence from the study of yields of fragments in the fission of uranium with thermal neutrons (Pappas 1953).

(4) The most probable primary charge, that is, the 'atomic number', generally non-integral, giving maximum yield in the charge distribution curve, is a linear function of the mass number, passing through the origin and having a slope equal to S in a Z versus A plot.

It may be remarked that the constant Q merely fixes the scale of the cross sections and is of minor interest here, since the measured cross sections are only relative in most cases.

The measured and calculated cross sections for the spallation groups discussed in this paper can be compared in the tables 2-13.

Table 2. $G(V; p; 187 \text{ mev})$. Cross Sections in millibarn. Experimental data: Rudstam (1953)

Nuclide	σ measured	σ calculated	Nuclide	σ measured	σ calculated
^{24}Na	0.030	0.020	^{45}Ca	3.6	4.7
^{27}Mg	0.028	0.032	^{47}Ca	0.11	0.08
^{31}Si	0.18	0.16	^{43}Sc	4.0	2.5
^{32}P	0.34	0.27	^{44}Sc	17	12
^{33}P	0.32	0.34	^{46}Sc	20	25
^{35}S	0.61	0.74	^{47}Sc	10	12
^{34}Cl	0.031	0.056	^{48}Sc	4.8	2.4
^{38}Cl	0.74	0.97	^{45}Ti	6.1	3.8
^{39}Cl	0.30	0.29	^{47}V	5.7	5.6
^{42}K	3.9	5.1	^{48}V	28	35
^{43}K	2.5	1.8	^{48}Cr	0.23	0.59

Table 3. $G(\text{Mn}; p; 187 \text{ mev})$. Relative Cross Sections. Experimental data: Rudstam (1953)

Nuclide	σ measured	σ calculated	Nuclide	σ measured	σ calculated
^{31}Si	0.027	0.022	^{45}Ca	0.25	0.31
^{32}P	0.034	0.047	^{47}Ca	0.007	0.007
^{42}K	0.39	0.40	^{45}Ti	1.00	0.94
^{43}K	0.21	0.14	^{49}Cr	2.2	2.3

Table 4. $G(\text{Cu}; d; 190 \text{ mev})$. Relative Cross Sections. Experimental data : Batzel, Miller and Seaborg (1951)

Nuclide	σ measured	σ calculated	Nuclide	σ measured	σ calculated
^{32}P	0.0005	0.00018	^{56}Mn	0.10	0.096
^{38}Cl	0.00032	0.00072	^{52}Fe	0.003	0.0024
^{39}Cl	0.00007	0.00039	^{53}Fe	0.047	0.022
^{45}Ti	0.002	0.0029	^{59}Fe	0.045	0.083
^{48}V	0.035	0.016	^{55}Co	0.022	0.025
^{49}Cr	0.01	0.0071	^{61}Co	0.094	0.192
^{51}Cr	0.03	0.061	^{57}Ni	0.054	0.037
^{51}Mn	0.029	0.011	^{60}Cu	0.20	0.30
^{52}Mn	0.087	0.043	^{61}Cu	1.00	0.98

Table 5. $G(\text{As}; d; 190 \text{ mev})$. Relative Cross Sections. Experimental data : Hopkins and Cunningham (1948)

Nuclide	σ measured	σ calculated	Nuclide	σ measured	σ calculated
^{52}Mn	0.0002	0.00065	^{61}Cu	0.1	0.018
^{56}Mn	0.002	0.0025	^{64}Cu	0.1	0.057
^{59}Fe	0.005	0.0040	^{67}Cu	0.02	0.013
^{55}Co	0.003	0.0007	^{69}Zn	0.12	0.032
^{61}Co	0.003	0.0093	^{66}Ga	0.1	0.13
^{57}Ni	0.0002	0.0011	^{68}Ga	0.2	0.26
^{65}Ni	0.001	0.0054	^{71}As	0.3	0.85
^{66}Ni	0.002	0.0018	^{72}As	1.00	1.1
^{60}Cu	0.06	0.0068			

Table 6. $G(\text{Fe}; p; 340 \text{ mev})$. Cross Sections in millibarn. Experimental data : Rudstam, Stevenson, and Folger (1952)

Nuclide	σ measured	σ calculated	Nuclide	σ measured	σ calculated
^{31}Si	0.12	0.07	^{47}Sc	0.84	0.98
^{32}P	0.044	0.15	^{48}Sc	0.45	0.20
^{35}S	0.23	0.23	^{45}Ti	3.7	1.9
^{34}Cl	0.11	0.07	^{47}V	2.4	2.7
^{38}Cl	0.17	0.21	^{48}V	10.3	7.4
^{39}Cl	0.045	0.059	^{48}Cr	0.80	0.73
^{42}K	0.7	0.75	^{49}Cr	4.8	4.0
^{43}K	0.4	0.25	^{51}Mn	4.0	5.7
^{45}Ca	0.56	0.50	^{52}Mn	13	18
^{47}Ca	0.007	0.010	^{52}Fe	0.68	1.32
^{46}Sc	3.2	2.4			

Table 7. G(Co; p; 370 mev). Cross Sections in millibarn. Experimental data: Belmont and Miller (1954)

Nuclide	σ measured	σ calculated	Nuclide	σ measured	σ calculated
³² P	0.30	0.21	⁴⁹ V	31.1	11
³³ P	0.03	0.20	⁴⁹ Cr	4.1	2.5
³⁹ Cl	0.50	0.14	⁵¹ Cr	27.5	16
³⁸ K	0.31	0.13	⁵¹ Mn	4.1	3.2
⁴² K	0.85	1.22	⁵² Mn	19.7	12
⁴³ K	0.50	0.52	⁵⁴ Mn	25.4	31
⁴⁵ Ca	0.66	1.00	⁵⁶ Mn	3.8	8.3
⁴⁷ Ca	0.06	0.04	⁵² Fe	0.28	0.61
⁴⁶ Sc	2.2	3.7	⁵³ Fe	1.7	4.3
⁴⁵ Ti	3.5	1.4	⁵⁵ Fe	37.0	39
⁴⁷ V	2.1	1.9	⁵⁵ Co	5.2	5.6
⁴⁸ V	10.6	5.8	⁵⁶ Co	15.2	24

Table 8. G(Zn; p; 340 mev). Cross Sections in millibarn. Experimental data: Worthington (1952)

Nuclide	σ measured	σ calculated	Nuclide	σ measured	σ calculated
³² P	0.02	0.063	⁵¹ Mn	2	1.1
³⁵ S	0.06	0.101	⁵² Mn	10	4.4
⁴² K	0.24	0.34	⁵⁶ Mn	1.9	1.9
⁴³ K	0.19	0.12	⁵² Fe	0.22	0.17
⁴⁵ Ca	0.22	0.24	⁵⁹ Fe	0.67	0.61
⁴⁷ Ca	0.0055	0.0054	⁵⁵ Co	1.5	1.9
⁴⁵ Ti	0.93	0.34	⁵⁶ Co	1.8	8.9
⁴⁷ V	0.8	0.60	⁵⁸ Co	46	30
⁴⁸ V	4.8	2.0	⁵⁶ Ni	0.090	0.25
⁴⁸ Cr	0.20	0.12	⁵⁷ Ni	1.7	2.4
⁴⁹ Cr	2.0	0.8	⁶¹ Cu	33	52

Table 9. G(Cu; p; 340 mev). Relative Cross Sections. Experimental data: Batzel, Miller, and Seaborg (1951)

Nuclide	σ measured	σ calculated	Nuclide	σ measured	σ calculated
³² P	0.0053	0.0019	⁵² Mn	0.31	0.17
³⁴ Cl	0.0003	0.0006	⁵⁴ Mn	0.53	0.48
³⁸ Cl	0.0025	0.0038	⁵⁶ Mn	0.11	0.12
³⁹ Cl	0.0004	0.0013	⁵² Fe	0.008	0.0065
⁴⁵ Ca	0.007	0.011	⁵³ Fe	0.073	0.056
⁴⁷ Ca	0.0004	0.00033	⁵⁵ Fe	0.49	0.63
⁴⁶ Sc	0.075	0.047	⁵⁹ Fe	0.034	0.050
⁴⁷ Sc	0.033	0.023	⁵⁵ Co	0.10	0.074
⁴⁵ Ti	0.044	0.015	⁵⁶ Co	0.15	0.37
⁴⁸ V	0.032	0.078	⁵⁸ Co	2.5	1.5
⁴⁹ Cr	0.041	0.030	⁶¹ Co	0.21	0.11
⁵¹ Cr	0.31	0.25	⁵⁷ Ni	0.079	0.098
⁵¹ Mn	0.071	0.041	⁶¹ Cu	1.00	2.4

Table 10. $G(\text{Cu}; p; 60 \text{ mev})$. Relative Cross Sections. Experimental data : Carleson (1954)

Nuclide	σ measured	σ calculated	Nuclide	σ measured	σ calculated
^{54}Mn	0.0012	0.0014	^{58}Co	0.25	0.07
^{56}Mn	0.00091	0.00075	^{61}Co	0.013	0.018
^{59}Fe	0.0018	0.0019	^{57}Ni	0.014	0.006
^{56}Co	0.0022	0.0086	^{60}Cu	0.32	0.33
^{57}Co	0.031	0.031	^{61}Cu	1.00	1.51

Table 11. $G(\text{Cu}; p; 2200 \text{ mev})$. Cross Sections in millibarn. Experimental data : Friedlander *et al.* (1954)

Nuclide	σ measured	σ calculated	Nuclide	σ measured	σ calculated
^{32}P	6.4	2.5	^{48}Cr	0.5	0.3
^{33}P	0.9	2.3	^{49}Cr	2.2	1.7
^{35}S	0.95	2.8	^{51}Cr	19	9.5
^{34}Cl	0.89	0.58	^{51}Mn	1.4	1.6
^{38}Cl	0.67	2.2	^{52}Mn	7.0	5.2
^{39}Cl	0.40	0.79	^{54}Mn	12	12
^{42}K	3.7	3.5	^{56}Mn	2.3	3.3
^{43}K	1.3	1.5	^{52}Fe	0.19	0.24
^{45}Ca	1.1	2.1	^{53}Fe	1.3	1.5
^{47}Ca	0.10	0.09	^{55}Fe	12	11
^{46}Sc	6.5	5.6	^{59}Fe	0.6	1.2
^{47}Sc	3.5	2.8	^{55}Co	1.5	1.4
^{48}Sc	2.4	0.8	^{61}Co	3.6	1.7
^{45}Ti	2.5	1.8	^{57}Ni	0.6	1.2
^{47}V	2.7	1.7	^{60}Cu	1.8	5.2
^{48}V	9.6	5.0	^{61}Cu	6.5	14
^{49}V	27	8.5			

Table 12. $G(\text{Cu}; n; 400 \text{ mev})$. Cross Sections in millibarn. Experimental data : Marquez (1952)

Nuclide	σ measured	σ calculated	Nuclide	σ measured	σ calculated
^{45}Ti	0.0078	0.071	^{59}Fe	2.44	2.3
^{49}Cr	0.35	0.20	^{55}Co	0.415	0.87
^{51}Mn	0.76	0.39	^{58}Co	62	24
^{52}Mn	4.68	1.5	^{61}Co	3.78	5.8
^{56}Mn	2.81	2.8	^{57}Ni	0.54	1.4
^{52}Fe	0.134	0.067	^{61}Cu	15.4	47
^{53}Fe	1.24	0.54			

Table 13. G(Cu; α ; 380 mev). Relative Cross Sections. Experimental data: Batzel, Miller, and Seaborg (1951)

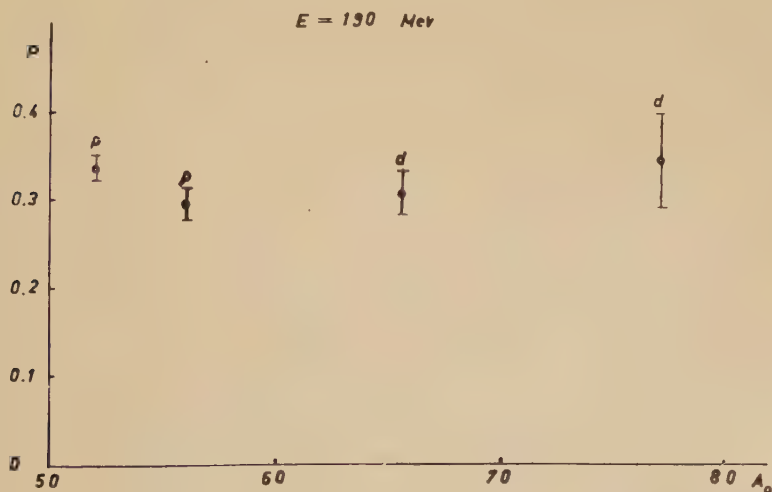
Nuclide	σ measured	σ calculated	Nuclide	σ measured	σ calculated
^{38}Cl	0.0022	0.0014	^{56}Mn	0.05	0.050
^{49}Cr	0.006	0.012	^{59}Fe	0.034	0.040
^{51}Cr	0.016	0.049	^{57}Ni	0.066	0.049
^{51}Mn	0.025	0.018	^{60}Cu	0.12	0.21
^{52}Mn	0.08	0.044	^{61}Cu	1.00	0.44

§ 4. COMPARISON BETWEEN SPALLATION GROUPS

The cross section distributions of different spallation groups can now be compared by studying the dependence of the parameters P , R , and S on the composition of the target and on the kind and energy of the bombarding particles. It must be remarked in advance, however, that it is not possible to obtain more than general trends from the available data.

The figs. 1-8 indicate how the parameters of the cross section equation vary with the energy of the bombarding particles and with the mass number A_0 or the atomic number Z_0 . A_0 is defined as the mass number of the nucleus formed by adding the bombarding particle to the target

Fig. 1



nucleus, in other words the 'compound' nucleus. Z_0 is the corresponding atomic number. A_0 , defined in this way, applies only to monoisotopic targets. For other target elements an average of A_0 has to be used. The kind of bombarding particle is denoted by the letters p, d, n, or α appearing above the corresponding point in the figures.

The dependence of the parameter P on A_0 can be studied in figs. 1 and 2 for the energies 190 mev (fig. 1) and 340-400 mev (fig. 2). It is

seen from the figures that P is almost independent of A_0 in the mass region investigated. It should also be noted that P does not depend on the kind of bombarding particle, with the possible exception of neutrons. Figure 3 shows P as a function of the energy. The parameter P decreases with increasing energy. This is to be expected. The steepness of the yield-mass curve should decrease with increasing energy of the bombarding particles.

Fig. 2

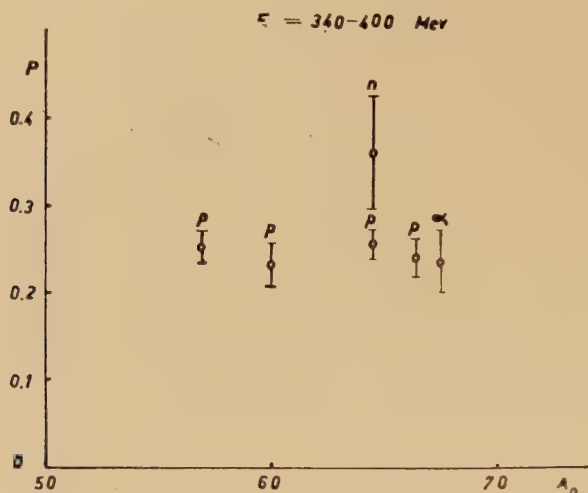
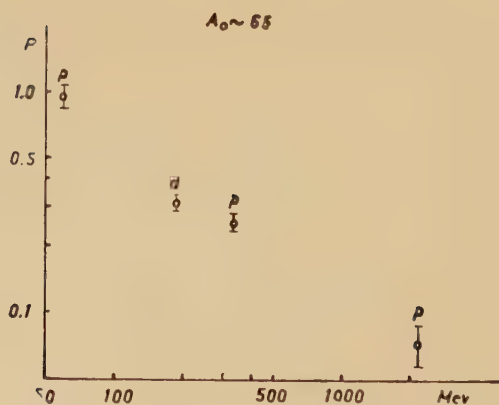


Fig. 3



The parameter R is plotted against A_0 for proton bombardments in fig. 4* and for bombardments with other projectiles in fig. 5. The energies of the bombardments (in mev) are denoted in the figures.

Figure 4 shows that R is quite insensitive to variation of A_0 and of the energy. Thus the charge distribution curve has almost the same width

* Three points at $A_0=64.5$ (spallation of copper) have been spread out in the figure.

in the spallation of copper with 60 mev and with 2200 mev protons. One might expect R to depend on the isotopic composition of the target, but this does not appear from the figure.

Figure 5 indicates that the parameter R is somewhat smaller for deuteron and alpha particle bombardments than for proton bombardment.

Fig. 4

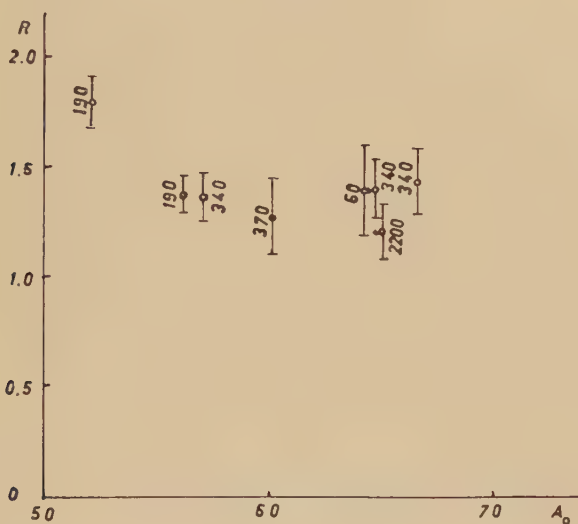
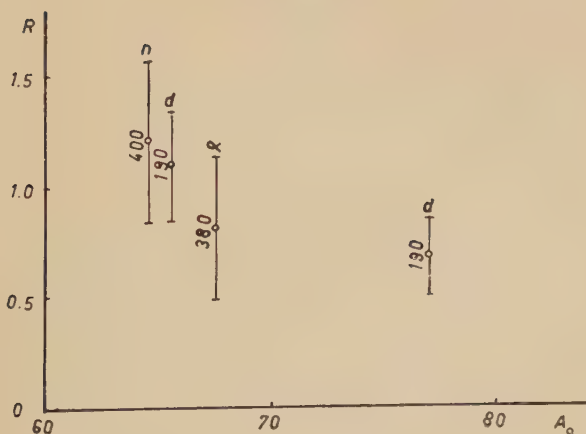


Fig. 5



It is not very profitable to compare the values of the parameter S for different spallation groups. Instead, one may study the behaviour of the factor $U = S - (Z_0/A_0)$, which is a measure of the preference for neutron emission. This factor will be zero if the most probable ratio between emitted protons and neutrons (where both free and bound

nucleons are considered) is the same as the ratio between protons and neutrons in the compound nucleus. If U is positive, neutron emission is more probable than proton emission. The factor U is plotted versus Z_0 for 190 mev in fig. 6 and for 340–400 mev in fig. 7 and versus the energy of the bombarding particles for $Z_0=30$ in fig. 8.

Fig. 6

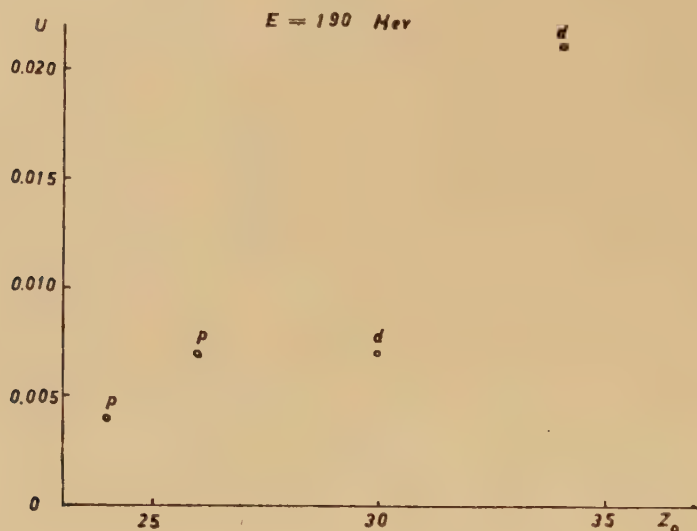


Fig. 7

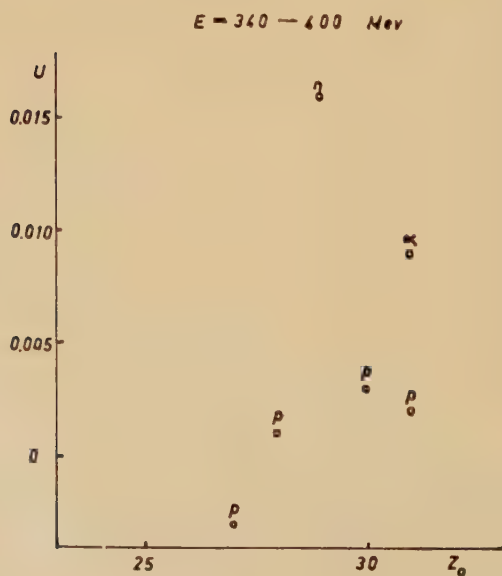
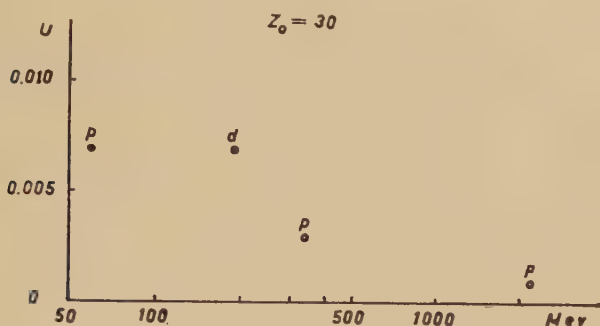


Figure 6 indicates an increase of U with increasing Z_0 . This increase is to be expected since the potential barrier for charged particles rises with increasing Z_0 .

Figure 8 shows that U decreases with increasing energy. This trend is not surprising. The potential barrier, which favours the emission of neutrons, is relatively more important when the energy of the bombarding particles is low.

Fig. 8



By integrating the cross section equation it is possible to estimate the total cross section, $\sigma(A_1; A_2)$, for formation of products with mass numbers between A_1 and A_2 . Thus one obtains :

$$\begin{aligned} \sigma(A_1; A_2) &\sim \int_{A_1}^{A_2} dA \int_{-\infty}^{\infty} \exp [PA - Q - R(Z - S \cdot A)^2] dZ \\ &= \frac{e^{-Q} \cdot \pi^{1/2}}{P \cdot R^{1/2}} [\exp (PA_2) - \exp (PA_1)]. \quad . \quad . \quad (4) \end{aligned}$$

§ 5. USE OF THE CROSS SECTION FORMULA

It is of practical interest to be able to estimate cross sections of spallation products as a function of the mass number (and the atomic number) of the target and of the kind and energy of the bombarding particles. A systematic study of spallation reactions, preferably with monoisotopic targets, and determination of cross section distributions might make such an estimation possible since the parameters of the cross section formula (1) could then be evaluated as functions of the variables mentioned above.

ACKNOWLEDGMENTS

The author wishes to express his thanks to Professor T. Svedberg for his stimulating interest in this work and to Drs. A. C. Pappas, D. Rosen and W. J. Swiatecki for helpful discussions.

REFERENCES

- BATZEL, R. E., MILLER, D. R., and SEABORG, G. T., 1951, *Phys. Rev.*, **84**, 671.
BELMONT, E., and MILLER, J. M., 1954, *Phys. Rev.*, **95**, 1554.
CARLSON, G., 1954, to be published.
FRIEDLANDER, G., MILLER, J. M., WOLFGANG, R., HUDIS, J., and BAKER, E., 1954, *Phys. Rev.*, **94**, 727.
HOPKINS, H. H., and CUNNINGHAM, B. B., 1948, *Phys. Rev.*, **73**, 1406.
MARQUEZ, L., 1952, *Phys. Rev.*, **88**, 225.
MILLER, D. R., THOMPSON, R. C., and CUNNINGHAM, B. B., 1948, *Phys. Rev.*, **74**, 347.
PAPPAS, A. C., 1953, *Technical Report* LNS-63, MIT, 7.
RUDSTAM, S. G., 1953, *Phil. Mag.*, **44**, 1131.
RUDSTAM, G., STEVENSON, P. C., and FOLGER, R. L., 1952, *Phys. Rev.*, **87**, 358.
WAGNER, G., and WIG, E. O., 1952, *J. Amer. Chem. Soc.*, **74**, 1101.
WORTHINGTON, W. J., 1952, *UCRL-1627*.

XLIII. CORRESPONDENCE

Radioactive ^{69}As and ^{70}As

By F. D. S. BUTEMENT and E. G. PROUT
Atomic Energy Research Establishment, Harwell

[Received January 13, 1955]

THE lightest radioarsenic isotope previously known is ^{70}As . This letter describes a new neutron deficient isotope ^{69}As .

Samples of 20 mg of 'Specpure' germanium dioxide were irradiated with protons at a series of energies from 8–60 mev. Radioarsenic was then isolated by dissolving the germanium dioxide in 3 ml. of 27N hydrofluoric acid, adding 5 ml. of 6N ammonium hydroxide and precipitating the arsenic as sulphide by passing in hydrogen sulphide. After a second precipitation with inactive germanium hold-back carrier, the arsenious sulphide was isolated for counting.

At proton energies of 8–20 mev the radioarsenic showed half-lives of 52 minutes (^{70}As), 26 hours (^{72}As and ^{76}As) and 17.6 days (^{74}As). Between 20 and 35 mev a new 15 minute activity appeared in appreciable yield (^{69}As), due to a (p, 2n) reaction on ^{70}Ge . Between 40 and 60 mev the initial half-life was ~ 10 minutes, suggesting the formation of a mixture of ^{69}As with a shorter lived activity, of half-life ~ 7 minutes, possibly ^{68}As produced by a (p, 3n) reaction on ^{70}Ge .

The mass assignment of the 15 minute activity to ^{69}As was made by milking off and identifying the radioactive germanium daughter. Radioarsenic isolated from germanium dioxide irradiated with 30 mev protons was prepared as a solution in hydrochloric acid containing inactive germanium carrier, and the germanium was then quantitatively isolated by distillation for two minutes in a current of chlorine. Successive separations of germanium were carried out at regular time intervals, fresh germanium carrier being added on each occasion. Germanium sulphide sources for counting were prepared from each distillate. All the germanium sources showed a half-life of 40 hours, due to ^{69}Ge , and the yields for successive separations decreased at a rate indicating a 15 minute half-life for the parent, ^{69}As .

The ^{69}As emitted positrons, the maximum energy of which, as determined by absorption in aluminium, was 2.9 mev. The absorption curve did not show any evidence of lower energy components. The gamma radiation was examined with a NaI(Tl) scintillation spectrometer and a single channel pulse analyser. In order to avoid the interference caused by the backscatter peak of the annihilation radiation, the source was mounted on a very thin aluminium foil in a magnetic field sufficient

to prevent any positrons from reaching the scintillator crystal. A single gamma-ray with an energy of 0.23 Mev was found. In both the positron and gamma-ray energy determinations corrections were made for the effects of the longer lived activities. The gamma-ray spectrum of 52 minute ^{70}As was also examined and gamma-rays of energies 1.06, 1.74 and 2.04 Mev were found in agreement with the results of Aten and Verkerk (1952). Additional gamma-rays of energies 0.18 and 1.36 Mev were also found.

REFERENCE

ATEN, A. H. W., and VERKERK, B., 1952, *Physica*, **18**, 974.

The Elastic Scattering of Protons by Helium 3

By D. R. SWEETMAN

Department of Physics, The University of Birmingham*

[Received January 29, 1955]

THE angular distribution for the elastic scattering of protons by helium 3 is of interest for comparison with the theoretical results given by Swan (1953).

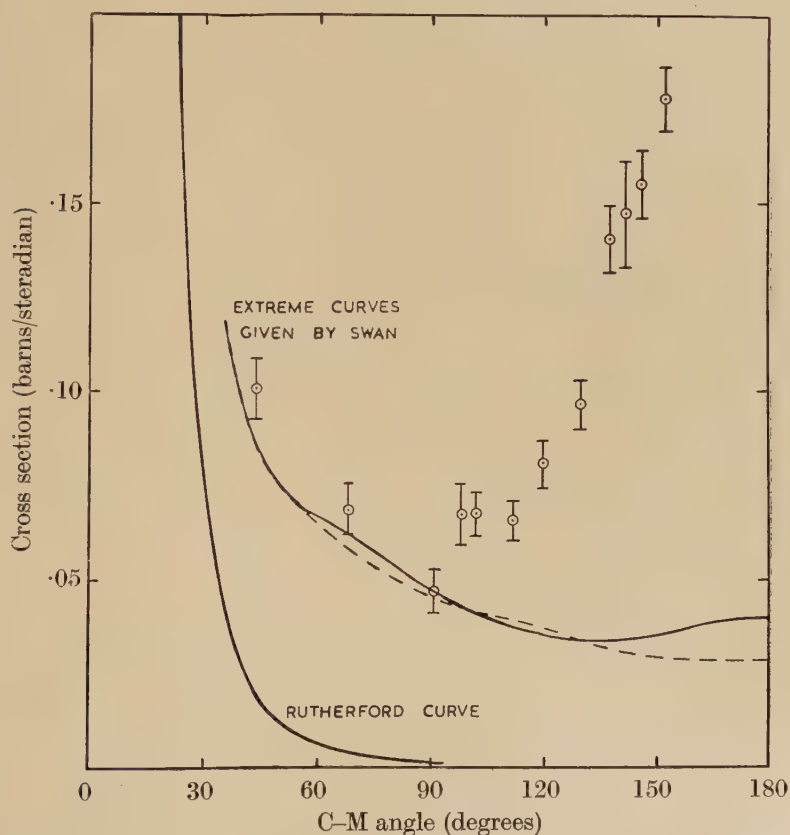
By operation of the Birmingham 60 in. cyclotron at $\frac{3}{4}$ the magnetic field used for $^2\text{D}+$ acceleration and using helium 2% enriched in ^3He fed into the ion source, an internal beam of ^3He ions suitable for transmutation experiments has been obtained (Fremlin 1952). Unfortunately, the unsuitable shimming at the low magnetic field results in the loss of most of the particles before they reach the extraction radius. Thus the present external ^3He beam is too small for scattering purposes and an attempt has therefore been made to use the internal ^3He beam with a specially designed scattering chamber.

As space was very restricted a nuclear plate was used as a detector, the method being similar to that used by Chadwick, May, Pickavance and Powell (1944) except that solid targets were used. The scatterer was mounted at 45° to the incident beam which was defined by a stop system; the natural collimation of the beam was found to be sufficient. The beam was received in a Faraday cup which was connected to a condenser, the voltage across which was measured with a Farmer electrometer voltmeter. Scattered particles entered the nuclear plate at a glancing angle of between 5 and 10 degrees. As the position of the beam hitting the scatterer was known accurately, relative cross sections could be determined with an accuracy essentially limited by the number of tracks that were measured in the plate. The beam was located and the cyclotron adjusted to resonance using a sensitive current meter connected to a mechanically operated shutter which was raised for the exposures.

* Communicated by J. H. Fremlin.

Trouble was experienced at first due to fogging of the plates by intense x-rays emitted by the dee feelers and dee edges. It was found, however, that thick layers of copper on the top and bottom of the chamber and a lead cap on the end facing the dee feelers were sufficient to reduce the fog background to negligible proportions.

Since it was difficult to determine absolute cross sections directly (due to the large vertical spread of the beam at the scatterer position) cross sections were normalized using a plate exposed to particles elastically scattered from gold, the cross sections for which were calculated from the Rutherford relationship.



Angular distribution for $p\text{-}^3\text{He}$ elastic scattering. C-M energy 3.72 mev.

The apparatus has been used to scatter 14.9 mev ^3He ions from protons (C-M energy=3.72 mev) the latter being conveniently obtainable in the form of polythene foil. A proton group of distinct range was obtained at all angles to the incident beam up to 70° when the range of the scattered protons became so small that some were lost in the scatterer. In order to establish the nature of the background to be subtracted from the proton group a second plate was exposed using a carbon scatterer.

The resulting angular distribution when converted to the C-M system for the scattering of protons by ^3He is shown in the figure. The probable errors shown have been calculated on a purely statistical basis from the number of tracks measured at each angle. The method of normalization employed limits the absolute accuracy of the cross sections to about 10%.

A preliminary result has been obtained for the higher C-M energy of 6.45 mev when the minimum appears to have moved to about 104° C-M angle.

The angular distribution given agrees with the general trend of the experimental results at lower energies given by Famularo, Brown, Holmgren and Stratton (1953) which also show a pronounced minimum near 90° and a steep rise towards 180° .

The distribution shown is not in agreement with the theoretical curves given by Swan (1953) who predicts no pronounced rise towards 180° for this energy. However, he suggests* that the agreement may be considerably improved by not using approximate Gaussian ground-state wave functions.

REFERENCES

- CHADWICK, J., MAY, A. N., PICKAVANCE, T. G., and POWELL, C. F., 1944, *Proc. Roy. Soc. A*, **183**, 1.
FAMULARO, K. F., BROWN, R. J. S., HOLMGREN, H. D., and STRATTON, T. F., 1953, *Bull. Amer. Phys. Soc.*, Vol. **28**, No. 6, 24.
FREMLIN, J. H., 1952, *Proc. Phys. Soc. A*, **65**, 762.
SWAN, P., 1953, *Proc. Phys. Soc. A*, **66**, 740.

* Private communication.

XLIV. REVIEWS OF BOOKS

Optics: Lectures on Theoretical Physics, Vol. IV. By ARNOLD SOMMERFELD. Translated from the German by Otto Laporte and Peter A. Moldauer. [Pp. vii+383.] (Academic Press Inc., New York.) Price \$6.80.

THIS book forms Volume IV of the author's series with the general title *Lectures on Theoretical Physics*. It includes a thorough treatment of the theory of diffraction regarded as a boundary value problem in electro-magnetic theory, and this is the most valuable part of the book. The rationalized M.K.S. system of electrical units is used. Unfortunately, the sections on elementary diffraction theory are not so satisfactory. They are in places inaccurate and suffer from the complete omission of any vector diagrams, which are so valuable in understanding diffraction phenomena. On page 220 it is stated that the intensity due to the first Fresnel zone for a circular aperture is equal to that of the unobstructed wave (instead of *twice* that of the unobstructed wave). Figure 64 is also incorrect. On page 215 the increase in strength of radio signals at the point on the Earth antipodal to the transmitting antenna is attributed to diffraction round the spherical Earth, but in practice this is due to the trapping and focussing effect of the ionosphere.

The treatment of anomalous dispersion is good, and includes an outline of the wave-mechanical theory. Other interesting topics, not usually found in standard textbooks on optics, include a quantum treatment of Doppler effect, the theory of Cerencov radiation, and a thorough discussion of wave propagation in dispersive media. The section on white light gives only a qualitative discussion and seems inadequate.

The methods of Fourier transforms and contour integration are frequently used, but not explained, reference being made to Volume VI of the series for a treatment of these mathematical topics.

Because of the omission of most of the experimental material, the book cannot be recommended as a standard textbook for students of experimental physics, though it should be useful as a reference book. Students of theoretical physics should find it valuable and stimulating. B. H. B.

Radio-Isotope Conference 1954, Vol. I, *Medical and Physiological Applications*. Edited by J. E. JOHNSTON, R. A. FAIRES and R. J. MILLETT. [Pp. xi+418.] (Butterworths Scientific Publications.) Price 65s.

THIS volume is a report of the Second Isotope Conference held in Oxford during July, 1954, the first one having been held in July 1951. There are 46 papers under the following headings:—Therapy, Diagnosis, Animal Physiology and Pathology, Biochemistry, and Plant Nutrition and Allied Subjects. The whole Conference, of which the above proceedings report a part, consisted of 70 papers chosen from 280 offered. The editors, in choosing the papers to be read, gave preference to new ideas and to new methods and stress the importance of new results. The present volume testifies admirably to their choice.

Whereas in 1951 the emphasis was still on the measuring and assaying of radioactive isotopes, it has now definitely moved over, in both clinical work and research work, to their uses. Nevertheless, techniques of measurement are still improving and from this Conference one can see, for example, how, during the past three years, the crystal scintillation counter has replaced the Geiger counter in this field. The uses of radio-iodine, radio-cobalt, and radio-phosphorus still form a large part of the Conference but the field is obviously expanding rapidly; however, uses for such isotopes as ^{90}Y , ^{59}Fe and

^{206}Bi , which had not appeared three years ago, are also described. Tracer work in metabolic studies is, of course, rapidly expanding; biochemical compounds labelled with ^{14}C and ^3H are now common tools. This again is reflected in the number of papers in this field.

The proceedings of the Conference demonstrate, if any were needed, how radioactive isotopes have developed into being one of the established working tools for both the medical specialist and biochemist. This Conference gives an excellent view of the present situation and points the way for further advances.

The volume is well bound, clearly printed and singularly free from mistakes, though at 65s. the price seems rather high. Both the editors and publishers are to be congratulated on the short time which elapsed between the Conference and the date of publication.

C. L. S.

BOOK NOTICES

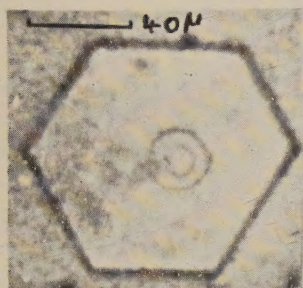
Luminescence with Particular Reference to Inorganic Phosphors. A symposium held by the Electronics Group of the Institute of Physics at the Cavendish Laboratory, Cambridge from the 7 to 10 April, 1954. *British Journal of Applied Physics*, Supplement No. 4. Price 25s.

Petrology for Students. An introduction to the study of rocks under the microscope. By ALFRED HARKER. [Pp. viii+283.] (Cambridge : University Press.) (8th edition, revised.) Price 18s.

Mathematics of Engineering Systems (Linear and Non-Linear). By DEREK F. LAWREN. [Pp. 380.] (Methuen & Co. Ltd.) Price 30s.

[The Editors do not hold themselves responsible for the views
expressed by their correspondents.]

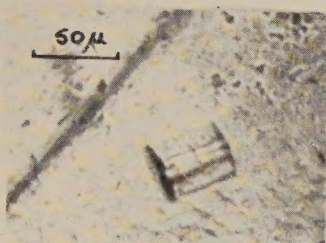
Fig. 2



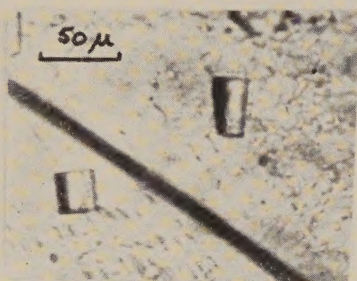
(a)



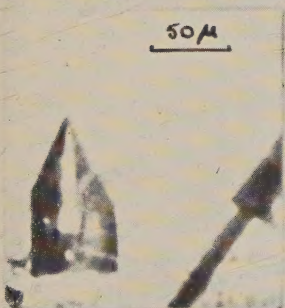
(b)



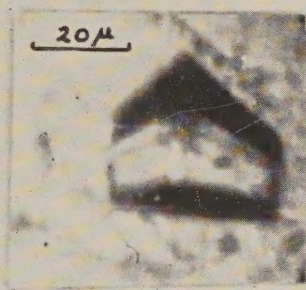
(c)



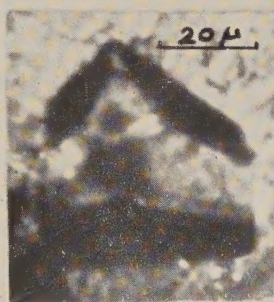
(d)



(e)

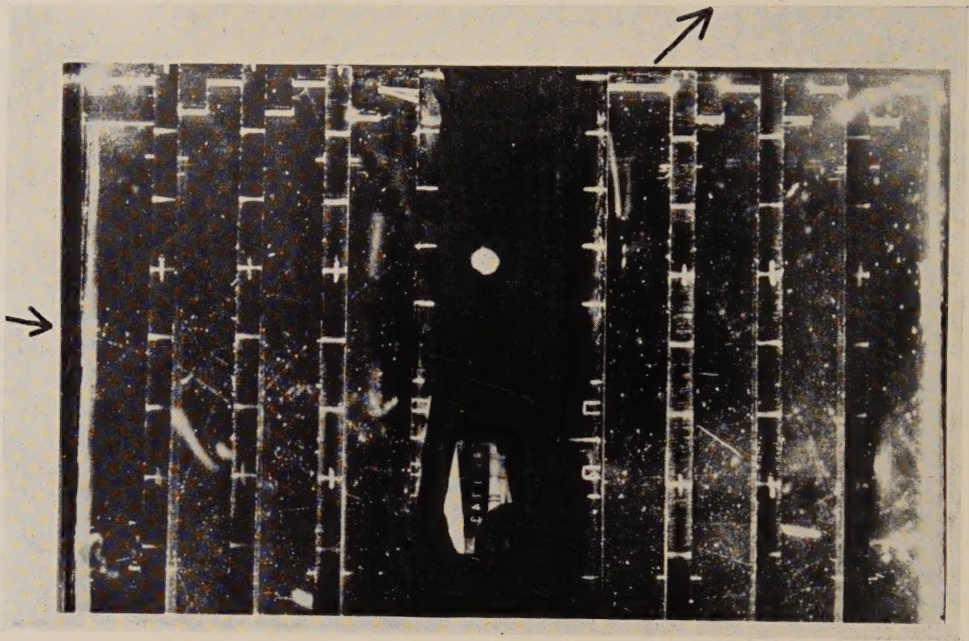


(f)



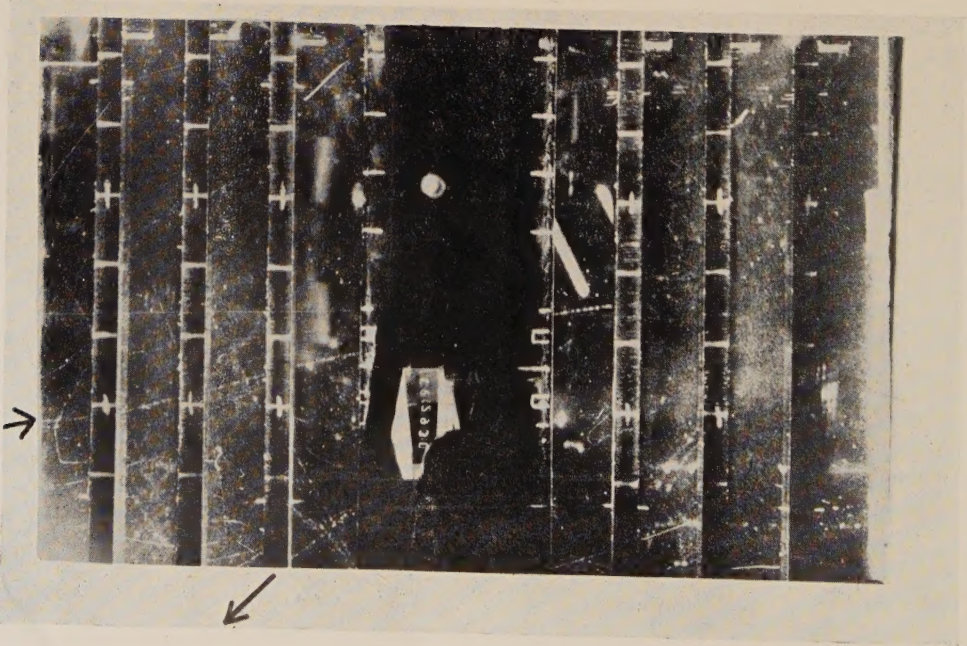
(g)

Examples of crystals grown on the metal plate. (a) Hexagonal plates (-15°C), (b) prisms (-6°C), (c) prisms (-22°C), (d) prisms (-33°C), (e), (f), (g), prisms with pyramidal faces (-22°C).



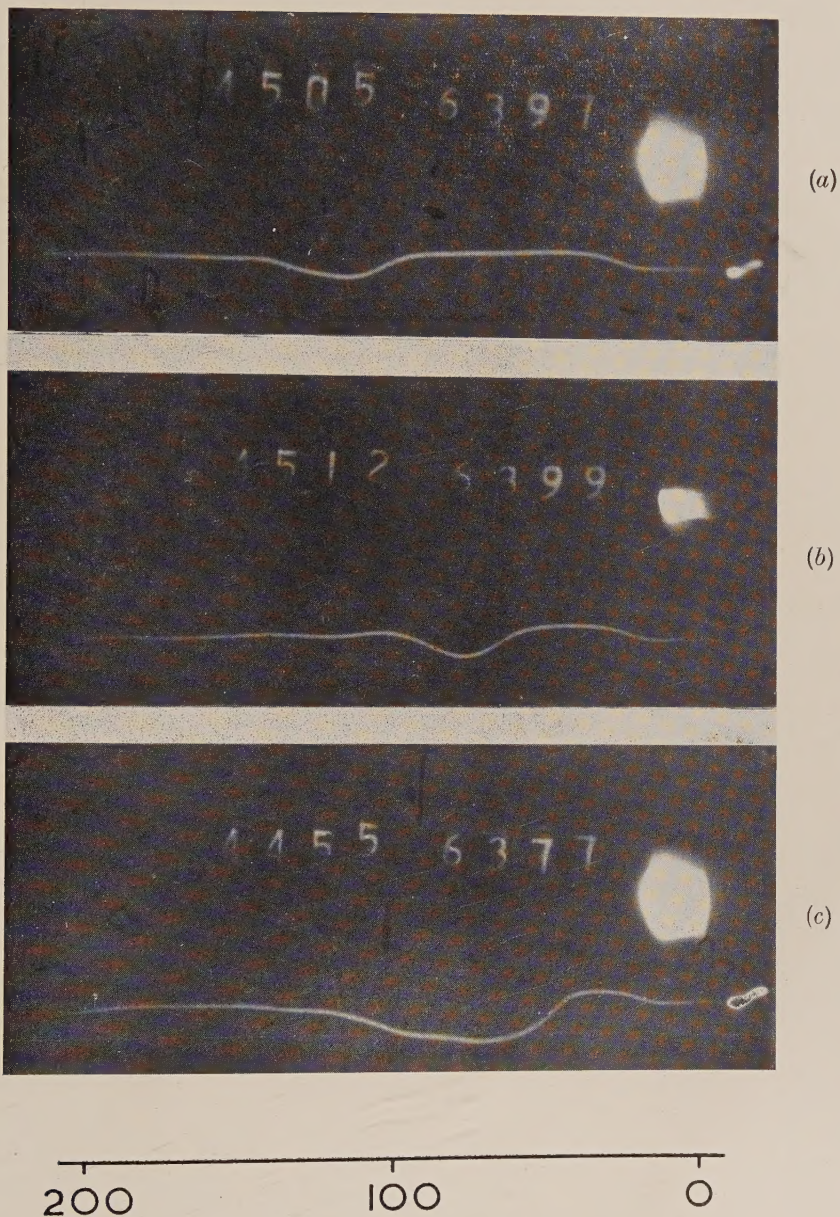
(b)

A heavy meson stops in the second plate emitting a downward-going secondary particle. The track in the third compartment dips steeply away from the camera



(a)

A heavy meson stops in the fourth lead plate of the cloud chamber and emits an upward moving decay particle. The slowly moving heavy particle gives no signal in the C_2 counter.



Oscillograph traces of S_1 and C_2 counter signals. The scale is in units of 10^{-9} sec.

(a) An S-particle, delay 36×10^{-9} sec.

(b) A fast meson, delay 1×10^{-9} sec.

(c) An electron shower of high density; many particles enter the counter C_2 .

The delay between the S_1 and C_2 signals is measured between points at which the trace is deflected through a fixed distance of about half a trace width.

